Resource Assessment and Feasibility Study for Use of Hydrokinetic Turbines in the Tailwaters of the Priest Rapids Project

Moriel A. Arango

A thesis
submitted in partial fulfillment of the
requirements for the degree of

Master of Science in Mechanical Engineering

University of Washington
2011

Program Authorized to Offer Degree:
Department of Mechanical Engineering

University of Washington
Graduate School

This is to certify that I have examined this copy of a master's thesis by

Moriel A. Arango

and have found that it is complete and satisfactory in all respects,
and that any and all revisions required by the final
examining committee have been made.

Committee Members:

_____
Philip C. Malte

_____
Alberto Aliseda

_____
Brian L. Polagye

Date: _____

In presenting this thesis in partial fulfillment of the requirements for a master's degree at the University of Washington, I agree that the Library shall make its copies freely available for inspection. I further agree that extensive copying of this thesis is allowable only for scholarly purposes, consistent with "fair use" as prescribed in the U.S. Copyright Law. Any other reproduction for any purposes or by any means shall not be allowed with my written permission.

Signature: _____

Date: _____

University of Washington

Abstract

Resource Assessment and Feasibility Study for Use of Hydrokinetic Turbines in the Tailwaters of the Priest Rapids Project

Moriel A. Arango

Chair of the Supervisory Committee:
Professor Philip C. Malte
Department of Mechanical Engineering

Grant County PUD has funded this work to study and analyze the stretch of the Columbia River downstream from the Wanapum and Priest Rapids Dams, owned and operated by the utility district, in order to assess the feasibility of introducing hydrokinetic turbines in the tailwaters of the dams for extracting kinetic power found in the flow of water. The use of this emerging technology allows for the generation of power without the need for impounding water and constitutes a way of harnessing a renewable energy source while satisfying the new requirements set forth by the state's Energy Independence Act. As an initial assessment, this study only considers pilot scale deployments consisting of one full-scale hydrokinetic turbine each.

The dams span across the Columbia River approximately 650 river kilometers inland from the Pacific Ocean, in the central part of Washington State. The two facilities are known as the Priest Rapids Project and have a combined rated capacity of 1893MW, ranking as the fifth largest conventional hydroelectric generating system on the Columbia River. The hydrokinetic resource

found downstream from each dam is assessed using: 1) operational data obtained directly from Grant County PUD, 2) results from physical and numerical modeling of the two stretches of river performed by the Iowa Institute of Hydraulic Research (IIHR) at the request of this study, and 3) discharge information found in the data bank of the Columbia River Data Access in Real Time (DART).

Four different hydrokinetic turbines that are currently available, or are scheduled to be in the near future, are studied as the viable technology to introduce in the tailrace waters. The devices cover a range of turbine designs and include a horizontal axis turbine with two blades manufactured by Tocardo International B.V., a shrouded horizontal axis turbine with seven blades and a diffuser on the downstream end being developed by Free Flow Power Corp., a vertical axis turbine with four/five blades designed by New Energy Corporation Inc., and Ocean Renewable Power Corporation's cross-flow horizontal axis turbine with four blades. Most of the devices are rated for water velocities between 3-3.5 m/s. Only the devices for which power performance curves are currently available are considered for power extraction, corresponding to those manufactured by New Energy Corporation Inc. and Tocardo International B.V.

Four sites are considered in this study as being feasible for using hydrokinetic turbines. For each dam the powerhouse vicinity is of interest since the velocity found at the outlet of the powerhouse draft tubes constitutes a loss in conventional hydroelectric systems and exploiting this kinetic energy would allow for the maximum use of the flow going through the conventional turbines. A spot located ~80m in front (i.e. downstream) of unit 6 of the Wanapum powerhouse and another located ~35m from the draft tube outlet of unit 4 of the Priest Rapids powerhouse are chosen. These locations coincide with the region where the river bed elevation found downstream of the powerhouses has increased near its maximum. A site is also identified well downstream from each facility that offers the best available combination of factors suitable for in-stream turbine siting. At approximately 1400m downstream from the left embankment of the Wanapum Dam, a region

immediately downstream from a constriction that occurs in the river is chosen because it is observed to average-out large spatial variations in the flow patterns that can occur during times of spill, be it fish passage spill or spill over the main spillway of the dam. The other downstream site is close to 550m from the Priest Rapids powerhouse, where the river reach is observed to have a region that develops high velocities that meet or exceed the rated velocities of most of the turbines being manufactured.

Vertical velocity profiles are created at the identified siting locations using the steady-state values of velocity components obtained from results of the IHR numerical simulations of the tailrace at characteristic low, median, and high total river flow rates; results available for the Wanapum tailrace correspond to total flow rates of 1.70, 3.00, and 5.79 thousand cubic meters per second (kcms) and for the Priest Rapids tailrace to total flow rates of 1.82, 3.91, and 5.72 kcms. For the vicinity of the powerhouses, an empirical profile is constructed based on simulation results pertaining to the Wanapum tailrace that depict velocity distributions similar to what has been reported in the literature for wall-bounded jets. The data from the downstream sites are fitted to a modified version of Cole's Law of the Wake, a well documented equation used for open-channel flow. Further empirical relationships are established between the various parameters necessary to construct the velocity distributions and the total river discharge.

The power density through the water column is determined from the velocity profiles and used along with probability distributions calculated for the total flow in each tailrace and the performance parameters of the turbines being considered to calculate the annual average power, energy production, and capacity factor for each hydrokinetic turbine for the sites. For the powerhouse vicinity, the total discharge is coupled with the probability distribution calculated for the draft tube outlet velocity. The placement of the hydrokinetic turbines at the sites is examined assuming both floating and bottom mounted scenarios.

At the site downstream from the Wanapum Dam, for a median river discharge, the depth averaged velocity is calculated to be 1.57m/s, with an average depth of 9.88m. The relatively slow velocity generally seen at this site, in comparison to the rated speeds for the turbines, is found to favor the low speed EnCurrent turbine produced by New Energy Corporation. A turbine rated at 25kW that is currently available and a turbine rated at 125kW that will be available soon, are considered. These models are designed to generate high torque at low speeds by increasing the rotor size while using the same size generator as the high speed models. The turbines have a generator and gear box intended to remain above the water line and can be mounted on a floating structure. For the 25kW turbine an average power of 8.0kW and an energy generation of 70MWh/y are calculated, corresponding to an annual capacity factor of 32%. An average power of 34kW and an energy production of 297MWh/y are determined considering the 125kW unit, with a slightly lower value of 27% calculated for the capacity factor. The difference between the capacity factors is attributed to the larger size of the rotor for the 125kW turbine that intercepts slower velocities deeper in the water column.

The downstream site at Priest Rapids offers the potential for placement in a region with high power density, but with relatively shallow water depth. Velocities at this site are quite high, and are found to exceed rated turbine velocities close to 50% of the time. At a median river discharge, the depth averaged velocity in the region of interest is calculated to be about 3.5m/s with an average depth of 5.4m. The Aqua T-50 turbine rated at 50kW manufactured by Tocardo International BV is found to perform best at this site. The Aqua T-50 is rated at a speed of 3.5m/s and is reported to function in flows close to 40% above the rated velocity but with a significant decrease in the efficiency of power extraction. Considering a bottom mounted deployment, the Aqua T-50 should give an annual average electric power extraction of 31.5kWa and an energy production of 276MWh/y. The capacity factor for the bottom mounted Aqua T-50 is calculated to be 63%.

The velocities calculated at the sites in the vicinity of the powerhouse favor once more the low speed turbines manufactured by New Energy Corporation. Near both powerhouses the average depth is around 9.5m and the most probable velocities range between 1.75-2.5m/s. For deployment considered in front of unit 6 of the Wanapum powerhouse, the annual capacity factor of the low speed 25kW EnCurrent turbine is calculated to be 79%, with an energy production of 172MWh/y and an annual average power of 19.6kW. Results show the 125kW device as having a capacity factor of 60%. Near unit 4 of the Priest Rapids powerhouse, the capacity factor of the low speed 25kW EnCurrent is 40% and 42.5% for the 125kW turbine. The capacity factor at Priest Rapids is lower than that at in the vicinity of the Wanapum powerhouse due to a higher probability of slower velocities and due to an inability to completely align the EnCurrent turbines with the flow due to the steepness of a positive slope found in front of the powerhouses. The other turbines show capacity factors of 20-30% at these sites, with the higher range in performance corresponding to floating deployments and the lower range to bottom mounted.

Keeping in mind the early stage of the technology and the limited experience that exists in bringing together a functioning deployment, the cost associated with setting up a pilot scale project is found to fall within a fairly broad range. Based on the limited information available from manufacturers for unit pricing and deployment estimates, the total cost for a stand-alone unit is estimated to range from $6,000 to $11,900 per rated kW installed. Operational and maintenance costs are approximated to fall within 4% of the capital investment. A detailed breakdown of the cost and the financing of a pilot scale deployment are not considered in this study.

Table of Contents

Page No.

List of Figures iii
List of Tables vi
List of Notation vii
I-Introduction 1
1.1 Research Motivation and Sponsorship: Grant County Public Utility District No.2 1
1.2 Hydropower 3
1.3 Open Channel Flow 6
1.4 River In-stream Energy Converting Technology 8
1.5 Hydrokinetic Resource Assessment Literature Review 17
1.6 IIHR 20
II-Site Identification 24
2.1 Priest Rapids Project 25
2.2 Total River Discharge 28
2.3 Downstream Sites 30
2.3.1 Wanapum Dam Tailrace 31
2.3.2 Wanapum Dam Tailrace Dynamics and Frequency 39
2.3.3 Priest Rapids Tailrace 44
2.4 Powerhouse Vicinity 50
2.5 Sediment Transport and River Bed Motion 56
III-Resource Assessment 58
3.1 Open Channel Turbulent Velocity Profiles 58
3.2 Downstream Sites 63
3.2.1 Wanapum Site 66
3.2.2 Priest Rapids Site 71
3.3 Powerhouse Vicinity 75
3.3.1 Draft Tube Flow 75
3.3.2 Draft Tube Outlet Wall Bounded Jet 82
IV-Deployment 93
4.1 Downstream Sites 97
4.1.1 Wanapum Tailrace 98
4.1.2 Priest Rapids Tailrace 99

4.2 Powerhouse Vicinity 101
V-Power Extraction and Energy Generation from a Pilot Scale Deployment 104
5.1 Deployment Assumptions Used for Calculating the Power Generation 106
5.2 Downstream Sites 107
5.3 Powerhouse Vicinity 112
VI-Cost Estimate 117
VII-Concluding Remarks and Recommendations 121
References 126
Appendix A: Probability and Relative Frequency Distributions 135
Appendix B: Distribution of the Velocity Parameters for the Downstream Sites……...144
Appendix C: Results for Additional Data Planes in the Vicinity of the Powerhouses……....155

List of Figures

Figure No. Page No.

Figure 1.1 Depictions of the rivers found in Washington State 3

Figure 1.2 Idealized performance curve for the Tocardo T50-A turbine 11

Figure 1.3 Conceptual design of the cross-flow RivGen™ Power System 12

Figure 1.4 Conceptual image of the vertical axis EnCurrent Power Generating System 13

Figure 1.5 Hydro+™ shrouded horizontal axis turbine 14

Figure 1.6 SmarTurbine™ shrouded horizontal axis turbine 15

Figure 1.7 T50-Aqua horizontal axis turbine 15

Figure 1.8 Projects in which IIHR has been involved for implementation at the Wanapum and Priest Rapids Dams 23

Figure 2.1 Location of Wanapum Dam and Priest Rapids Dam along the Columbia River 24

Figure 2.2 Daily average fluctuations of the total and powerhouse flow rates at Priest Rapids Dam 26

Figure 2.3 Aerial view of Wanapum Dam 27

Figure 2.4 Aerial view of Priest Rapids Dam 28

Figure 2.5 Annual exceedance probability of total river discharge through Wanapum Dam 29

Figure 2.6 Annual exceedance probability of total river discharge through Priest Rapids Dam 30

Figure 2.7 Wanapum Dam tailrace; total river flow rate of 1.7kcms with 0.566kcms flow through the fish bypass 32

Figure 2.8 Wanapum Dam tailrace; total discharge of 3.0kcms with all of the flow going through the powerhouse 33

Figure 2.9 Wanapum Dam tailrace; discharge of 2.1kcms going through the spillway and a total flow rate of 5.8kcms 33

Figure 2.10 Bathymetry of the Wanapum Dam tailrace 34

Figure 2.11 Data plane used to describe the downstream site in the Wanapum tailrace contoured with the streamwise velocity and tailrace bathymetry 35

Figure 2.12 Distribution of a) maximum streamwise velocity, b) specific discharge, and c) depth, across the downstream site in the Wanapum tailrace 37

Figure 2.13 Fish and regular spill at Wanapum Dam 41

Figure 2.14 Velocity vectors across the river for the three discharge simulations at the Wanapum downstream site 43

Figure 2.15 Priest Rapids Dam tailrace; contoured streamlines of the flow for a simulation of 1.82kcms being discharged through the powerhouse 45
Figure 2.16 Priest Rapids Dam tailrace; contoured streamlines for a flow of 3.91kcms going through the powerhouse 46
Figure 2.17 Priest Rapids Dam tailrace; velocity contours and streamlines for a configuration of 0.425kcms flowing through the spillway chute 22 and 4.67kcms going through the ten powerhouse units 46
Figure 2.18 Top-down view of the bathymetry data provided for the Priest Rapids tailrace 47
Figure 2.19 Streamwise velocity distribution 550m downstream from the Priest Rapids powerhouse 47
Figure 2.20 Distribution of a) maximum streamwise velocity, b) specific discharge, and c) depth across the downstream site in the Priest Rapids tailrace 49
Figure 2.21 Simulation data planes in the vicinity of the Wanapum powerhouse 51
Figure 2.22 Layout of a Kaplan turbine and draft tube in the Wanapum powerhouse 54
Figure 2.23 Relative frequency of the area averaged draft tube outlet velocity 55
Figure 2.24 Images taken from the shore of the tailraces 57
Figure 3.1 Plot of the streamwise velocity vs. the normalized depth at five different locations across the Wanapum downstream site 64
Figure 3.2 Distribution of shear velocity across the Wanapum site for a river discharge of 3.00kcms 67
Figure 3.3 Normalized depths vs. normalized velocity deficits for the three Wanapum tailrace discharge simulations 69
Figure 3.4 Typical velocity profiles for the downstream Wanapum site 70
Figure 3.5 Shear velocity distributions for the three discharges across the Priest Rapids downstream site 71
Figure 3.6 Normalized depths vs. normalized velocity deficits for the three Priest Rapids tailrace discharge simulations 73
Figure 3.7 Typical velocity profiles for the downstream Priest Rapids site 74
Figure 3.8 Original (a) and new Kaplan (b) turbine used in the Wanapum powerhouse 76
Figure 3.9 Secondary flow and Görtler vortices expected to be present in the 90° bend of the draft tube 79
Figure 3.10 Inlet conditions and draft tube outlet results for the unsteady numerical simulation performed by Paik et al. [79] 82

Figure 3.11 Data plane running perpendicular from the Wanapum powerhouse through the middle bay of unit 6 85
Figure 3.12 Large surface boils in front of the Wanapum powerhouse 86
Figure 3.13 Behavior of the normalized maximum velocity as a function of distance from the draft tube outlet 87
Figure 3.14 Typical velocity magnitude profile along the region where the bed gradient decreases in the vicinity of the Wanapum powerhouse 89
Figure 3.15 Normalized heights vs. normalized velocity magnitude along the region of bed gradient decrease in the powerhouse vicinity for the Wanapum Dam simulations 90
Figure 3.16 Representative normalized velocity vs. normalized height in the powerhouse vicinity 91
Figure 4.1 Power density contours in the Wanapum downstream site and across the whole river for the ~50% exceedance discharge 98
Figure 4.2 Power density contours across the whole river and the siting region for the Wanapum downstream site for a) the 95% exceedance discharge and b) the 5% exceedance discharge..... 99
Figure 4.3 Power density contours across the Priest Rapids downstream site and the whole river for the ~50% exceedance discharge 100
Figure 4.4 Power density contours across the river and region for siting in the Priest Rapids tailrace for a) the 95% exceedance discharge and b) the 5% exceedance discharge 101
Figure 4.5 Typical arrangement considered for bottom mounted deployments in the vicinity of the Wanapum powerhouse……..…….102
Figure 4.6 Illustration of a hydrokinetic device deployed on the free surface in the vicinity of the Priest Rapids powerhouse……...….103
Figure 5.1 Depiction of the steps taken to compute the annual average power for the downstream sites 109
Figure 5.2 Exceedance probability of the depth averaged streamwise velocity over the area of the turbines at the downstream micro-sites 112
Figure 5.3 Exceedance probability of mean draft tube outlet velocity for unit 6 and unit 4 at the Wanapum and Priest Rapids powerhouse, respectively 116

List of Tables

Table No. Page No.

Table 2.1 Averaged and Integrated Parameters for the Downstream Site at Wanapum Dam for the Three Characteristic Flows 39

Table 2.2 Averaged and Integrated Parameters for the Downstream Site at Priest Rapids Dam for the Three Characteristic Flows 49

Table 2.3 Dimensions of Draft Tubes Found at the Wanapum and Priest Rapids Powerhouses 54

Table 3.1 Median RMSD and R^2 Errors for All of the Fitted Velocity Profiles in the Wanapum Downstream Site 71

Table 3.2 Median RMSD and R^2 Errors for All of the Fitted Velocity Profiles in the Priest Rapids Downstream Site 75

Table 3.3 Parameters of the Priest Rapids Project Kaplan Turbines 78

Table 3.4 Constants for the Empirical Velocity Profile Equation Used in the Powerhouse Vicinity 92

Table 4.1 Characteristics of Floating and Bottom Mounted Structures 95

Table 4.2 Anchoring Options 96

Table 5.1 Performance Parameters of the Hydrokinetic Turbines 105

Table 5.2 Characteristics of the Hydrokinetic Turbines Used for Calculating Power Extraction . 106

Table 5.3 Empirical Correlations between Total River Discharge and Velocity Profile Parameters 108

Table 5.4 Results of Annual Average Power, Energy, and Capacity Factor at the Wanapum Site 110

Table 5.5 Results of Annual Average Power, Energy, and Capacity Factor at the Priest Rapids Site 110

Table 5.6 Empirical Relations between Free-Surface in Front of the Powerhouses and Total River Discharge 113

Table 5.7 Results of Annual Average Power, Energy, and Capacity Factor in the Wanapum Powerhouse Vicinity with the 'Best Scenario' Velocity Profile 114

Table 5.8 Results of Annual Average Power, Energy, and Capacity Factor in the Priest Rapids Powerhouse Vicinity with the 'Best Scenario' Velocity Profile 114

Table 6.1 Pricing of Available Hydrokinetic Turbines 117

List of Notations

a_c - Cross-sectional area between vertical velocity profiles (m^2)

A_c - Cross-sectional area (m^2)

δ – Height of maximum streamwise velocity, 'dip position' (m)

d_h - Hydraulic depth (m)

$\partial u/\partial z$ – Gradient of the streamwise velocity with respect to the height above the river bed (1/s)

$\partial h/\partial s$ – Change in depth with respect to the streamwise direction (m/m)

$\partial p/\partial s$ – Pressure gradient with respect to the streamwise direction (N/m^3)

D - Ratio of hydroelectric turbine runner diameter to a runner diameter of 1m

D_h - Hydraulic depth (m)

ε – Turbulent kinetic energy dissipation

E - Average electricity (MWh/y)

Fr - Froude number (non-dimensional)

g - Gravitational acceleration; taken to be equal to 9.81 m/s^2

h – Depth of water column (m)

$h_{1/2}$ – Characteristic depth used to describe wall-bounded jets (m)

H_{gross} - Net head acting on a conventional hydroelectric turbine (m)

H_n - Ratio of net head acting on a hydroelectric turbine to a net head of 1m

k – Turbulent kinetic energy production

κ - von Kármán constant; taken to be equal to 0.41

kcms - Units of discharge equal to $10^3 m^3/s$

kW - Kilowatts; units of power equal to $10^3 W$

kWa - Average kilowatts

l - Characteristic length scale (m)

λ - Tip speed ratio (non-dimensional)

μ - Dynamic viscosity (kg/(ms))

MW – Megawatts; units of power equal to $10^6 W$

η_e - Total extraction efficiency of turbine (%)

η_{gross} - Net efficiency of conventional hydroelectric turbine (%)

n_{11} - Specific speed of a conventional hydroelectric turbine (rpm)

Ω - Rotating angular velocity (rad/s)

ρ - Density; taken to be equal to $10^3 kg/m^3$ for water

p – Pressure (N/m^2)

P - Power in the flow; units of Watts (W)

P_{gen} - Electric power generated by turbines (W)

P_w - Wetted perimeter (m)

q - Specific discharge (m^2/s)

Π - Cole's wake strength parameter

Q - Discharge (m^3/s)

Q_{11} - Specific discharge of a conventional hydroelectric turbine (m^3/s)

R - Radius (m)

Re – Reynolds number (non-dimensional)

Re_τ – Friction Reynolds number

s - Streamwise direction

τ_0 - Shear force per unit area on river bed boundary (N/m^2)

T_w - Top width of a cross-section (m)

u - Instantaneous point velocity (m/s)

$\bar{u}$ - Time averaged point velocity component (m/s)

$\acute{u}$ - Fluctuating point velocity component (m/s)

u_* - Shear velocity (m/s)

U - Free surface velocity (m/s)

ν - Kinematic viscosity; taken to be equal to $1.26073*10^{-6}$ (m^2/s)

ν_t – 'Eddy' viscosity

V - Mean velocity of the flow (m/s)

V_d - Depth averaged velocity (m/s)

$\overline{V_d}$ - Average of depth averaged velocities (m/s)

z - Height above the river bed (m)

z^+ - Dimensionless height

z_o - Bed height where no-slip condition is satisfied (m)

Acknowledgments

The author would like to thank the Public Utility District No. 2 of Grant County (Grant County PUD), WA, for their pursuit and interest in renewable energy sources, which has led to the funding of this work. The continual assistance by Grant County PUD's Manager of Resource Planning, Mr. Keith Knitter, in coordinating the structure of this research and maintaining open lines of communication for accessing data was fundamental to the completion of this project and is strongly appreciated. Additional recognition goes to the Grant County PUD's Manager of Transmission Services, Mr. Rod Noteboom, the Project Manager and Hydroelectric Engineer, Mr. Dana Jeske, and the Project Engineer, Mr. Brad Strickler, for their contributions with operational and performance data of the Priest Rapids Project. The author would like to credit the participation of Iowa's Institute of Hydraulic Research (IIHR), as it was essential in performing this study. The key involvement of Dr. Larry Weber, Director of IIHR, in establishing a path of collaboration with IIHR is very much valued and a special gratitude is expressed for the Associate Research Engineer, Dr. Marcela Politano, for her significant role in sharing results of work performed at IIHR and for her patience in the collection of data specified by the authors for use in this project. An immense sense of respect and appreciation is expressed to Professor Philip C. Malte, whom shared his vision and experience in his guidance through this research project. His continual support, motivation and drive, for which the author is extremely grateful, will always be valued. Furthermore, the author would like to thank Professors Alberto Aliseda, Brian Polagye and James Riley from the Department of Mechanical Engineering at the University of Washington and other members of the Northwest National Marine Renewable Energy Center-UW for their contribution and insight into matters of fluid dynamics and hydrokinetic technology. The foundation upon which the author relied to maintain composure, concentration and determinacy, was his wife and family. An outmost feeling of joy in the completion of the work is attributed to them, as they have been significantly influential in the path taken by the author in his life.

I – Introduction

As population densities increase, the strain placed on the existing resources necessary to sustain this growth demands that national governments worldwide, as well as regional and local functionaries, support the development of new means for harnessing the wealth of different energy sources. In addition, concern over immediate and long-term environmental impacts coupled with the desire to reduce local dependency on exterior suppliers, has placed an emphasis on increasing power generation through the use of promising sustainable and renewable sources. By making use of river in-stream energy conversion (RISEC) devices that capture the kinetic energy from the flow of water, an emerging alternative is strengthened through the experienced gained.

1.1 Research Motivation and Sponsorship: Grant County Public Utility District No.2

The passage of House Bill 1010 and Initiative 937 in 2006 brought new chapters to the constitution of the state of Washington with the establishment of the Energy Independence Act. The law now requires publicly owned electric utilities providing service to more than 25,000 customers to account for 15% of their base load with energy generated through the use of eligible renewable sources by the year 2020.

Grant County Public Utility District No.2 (Grant County PUD) is the owner and operator of both the Wanapum and Priest Rapids Dams located on the Columbia River. The two hydroelectric plants are referred to as the Priest Rapids Project. The Project provides energy for the entire Grant County, with a population of approximately 85,000, as well as other regions in central Washington, the Puget Sound and Oregon. The Priest Rapids Project has a combined generating rated capacity of 1893MW, and ranks as the fifth largest hydroelectric generating system on the whole stretch of the Columbia River. As such, Grant County PUD is a significant contributor to the generating capacity of the state and must comply with the new law and its requirements outlined in the state's Energy Independence Act.

An Integrated Resource Plan (IRP) submitted in 2008 by Grant County PUD to the state Department of Commerce in compliance with the new law, lists the current additional energy resources being explored. They included the development of an in-county and Yakama biomass project (13MWa); the design of a 1.5 MWa hydrokinetic energy system within the in-county canal system; the advancement towards the full generation potential of the Wapato Irrigation Project in partnership with the Yakama Nation; and the progress in setting up a natural gas fired cogeneration plant to serve combined heat and power needs of major industrial customers.

In addition to the aforementioned energy resources, another option on the table that Grant County PUD can explore is the possibility of installing hydrokinetic turbines in the tailrace of the existing hydroelectric dams. The recent emergence of the technology in the market raises questions that must be carefully considered before incorporating such a technology into an existing energy portfolio. In an attempt to address the uncertainties associated with the implementation of RISEC turbines in the tailrace of the Wanapum and Priest Rapids Dams, Grant County PUD funded this resource assessment to determine the feasibility of implementing this technology to harness power from the tailrace waters of the Priest Rapids Project.

In accordance with Grant County PUD, the assessment is comprised of the following:

1. A review and analysis of the operational data from the dams, as provide by Grant County PUD, coupled with additional data obtained from numerical and physical models of the two dams developed by the University of Iowa's Institute of Hydraulic Research (IIHR).
2. An analysis of the potential power extraction from the two tailraces through the selection of either a generic turbine with nominal efficiencies based on turbomachinery power extraction theory or information made available from manufacturers.
3. A conceptualized deployment of a pilot scale plant.
4. An estimate of the cost of power extraction based on information available from related hydrokinetic and hydropower applications.

1.2 Hydropower

During the past seven decades the Pacific Northwest region has been a leader in conventional hydropower electric generation in the United States. For 2008 the U.S Energy Information Administration (EIA) reports that in Washington State alone, 77,637 GWhrs of electrical energy was generated through conventional hydropower; this is equivalent to 30.47% of the total net electricity generated from conventional hydropower in the United States and 1.88% of the total net electricity generated by means of all the energy sources used in the country. As observed in figure 1.1, this image generated by the Washington State Department of Ecology shows a state that is very hydrologically active.

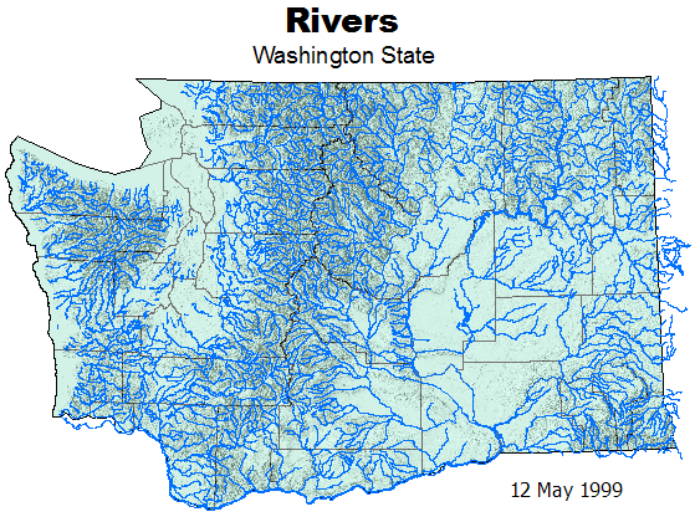

Figure1.1 Depictions of the rivers found in Washington State**.**
Image from Washington State's Dept. of Ecology [1]

Having the second largest average runoff in the United States, the Columbia River is by far the grandest of the multiple waterways found in the state. The United States Army Corps of Engineers (USACE) reports an average discharge at the mouth, where the Columbia River reaches the Pacific Ocean, of roughly 8 thousand cubic meters per second (8 kcms). The immense source of energy potential found in the course of the river as it moves through the United States is harnessed by eleven hydroelectric facilities. Five of these dams are non-federal projects owned and operated by three public utility districts and six are federal projects operated primarily by the USACE, and one owned and operated by the Bureau of Reclamation.

Based on records for 2009 released by EIA, conventional hydroelectric generation was the largest source of renewable energy in the United States, accounting for 65.5% of the electricity generated through renewable sources, and 6.9% of the country's total electricity generated, which amounted to 3,950 TWhrs. However, large hydroelectric dams have been recognized as one of the primary means by which humans have altered fluvial ecosystems [2-4]. Furthermore, an assessment of the waterpower potential released by the Electric Power Research Institute (EPRI) [5] forecasts that no additional power capacity will come through the construction of large (>30MW) conventional hydroelectric dams in the nation. Regardless, vast amounts of untapped energy may still remain in the numerous rivers across the country, and in this state, in particular.

Aside from steps that hydropower facilities can take to improve their systems as they stand today, such as adding turbines in available intake bays, and upgrading generators and turbines with larger and more efficient ones, the EPRI assessment points to additional hydro capacity that can be harvested from rivers through the development of small (<1MW) and low (between 1 and 30MW) capacity hydroelectric dams, the implementation of hydrokinetic devices in natural streams and constructed waterways, and through the extraction of energy from dams that currently exist as control stations.

There is a limited understanding of the available energy found in river flows. A report estimating the national availability of kinetic power in natural streams was published in 1986 by members of the New York University [6, 7]. In their survey an overall resource capacity of 12,500MW, or 110TWh/yr, was determined for rivers with discharges greater than 0.113kcms and velocities above1.3m/s [8]. The availability of this document is limited and is only found as a referenced source in other studies. Currently, the National Research Council is conducting an independent evaluation of a detailed resource assessment funded by the Department of Energy (DOE) in 2009, which was intended to determine and update the potential found in U.S. marine and hydrokinetic resources for the purpose of energy generation [9]. Among the hydrokinetic resources considered

were natural rivers and man-made channels. The completion of this work is expected to occur in 2012.

The principle behind the hydrokinetic power found in the flow of water is similar to that found in wind. Through conservation of energy, the power existing at a point in the cross-sectional area of a stream of water flowing at a given speed can be equally determined using equation 1.1;

$$P = \frac{1}{2}\rho A_c u^3 \qquad (1.1)$$

where P (W) is the power in the flow, ρ (kg/m^3) is the density of water, A_c(m^2) is the cross-sectional area of interest, and u(m/s) is the undisturbed instantaneous point velocity of the oncoming flow in the cross-section.

When considering the use of a device to extract the available power, the cross-sectional area of the device that intersects the flow is taken as the area of interest and the total efficiency of the device and associated power system in converting the kinetic power into electrical power has to be considered. Thus, the generated power (P_{gen}) is calculated using equation 1.2,

$$P_{gen} = \frac{1}{2}\rho A_c u^3 \eta_e \qquad (1.2)$$

where the power (P) from (1.1) is modified by η_e, the total extraction and conversion efficiency of the considered system, and A_c is the cross-sectional area of the hydrokinetic device that perpendicularly intersects the oncoming flow.

As power is proportional to the cube of the velocity, it is of particular interest to identify zones within a waterway that provide high velocities and sufficient depth to accommodate a device. The proper identification of sites will allow for the optimal functionality of devices and determine the economic viability of a project, which is dictated by the power density at a site [10]. In order to locate sites with the greatest potential, it is important to understand the complexities that characterize rivers.

1.3 Open Channel Flow

Natural streams, as opposed to man-made irrigation or water treatment channels, have carved out their own path through areas that provide the least resistance to their flow. This path can typically be associated with variations in shape, size, and river bed composition as one goes along the path of the river, or streamwise direction of the current. Additionally, there are often obstructions in a river such as islands and rock outcroppings, as well as bed surface irregularities shaped like dunes and large ripples. All of these variations have a direct effect on the resistance to the movement of the water and influence the distribution of velocities and shear stresses associated with friction across a cross-section of a river [11,12].

If the governing physical equations of conservation of mass and momentum are considered, it is understood that river flows are driven by gravity. Through dimensional analysis it has been formulated that in order for dynamic similarity between flow scenarios to exist they must share an equal Froude number. The Froude number is commonly defined as

$$Fr = V/\sqrt{gh} \tag{1.3}$$

where V(m/s) is the mean velocity of the flow, g(m/s^2) is the gravitational acceleration, and h(m) is the depth of the water column. The Fr number represents the ratio of the inertia force associated with a flow to the gravity force acting on the fluid. When calculating Fr for a non-uniform cross-sectional area of an open channel flow the depth is replaced with the hydraulic depth, d_h(m), given as

$$d_h = A_c/T_w \tag{1.4}$$

where T_w(m) is the width of cross-section at the free surface. The hydraulic depth thus represents an average depth based on the top width.

For small amplitude disturbances that occur at the water's free surface, the speed of propagation of the associated waves equals $(gh)^{1/2}$ [11]. These waves are typically characterized as shallow-

water gravity driven waves where the wavelength of the disturbance is much larger than the depth [13]. If a flow is characterized by $Fr < 1$, the flow is said to be sub-critical and these small amplitude waves will propagate in both the down and upstream direction. If $Fr > 1$, the flow is said to be super-critical and the surface disturbances will be swept in the downstream direction since the velocity of the flow is greater than the propagation speed. At the transition $Fr = 1$ and the flow is said to be critical.

For hydrokinetic turbine deployments it is best to avoid super-critical flows as these commonly undergo an abrupt change from the associated shallow depth and fast velocities to a sub-critical flow with larger depths and slower velocities. The transition occurs when the depth of a super-critical flow grows up to the critical depth, typically through the drag induced by frictional forces slowing the flow. The turbulent transition that occurs is referred to as a "hydraulic jump". These jumps are always accompanied by a significant energy loss and large counterclockwise rolling eddies that move up through the water column and appear as boils or upwellings at the free surface. By introducing a turbine into a region where super-critical flow is maintained, the associated drag that the turbine experiences and thus exerts back onto the flow could be sufficient to trigger a hydraulic jump.

The state of turbulence in the flow is dependent also on other governing parameters. The Reynolds number is the characteristic number that provides insight into the turbulent state and is defined as follows

$$Re = Vl/\nu \qquad (1.5)$$

where l(m) is a characteristic length scale, and ν(m^2/s) is the kinematic viscosity of the fluid. The Re number is representative of the influence that the viscosity of a fluid plays in determining how a flow behaves, with turbulent flows, i.e. large *Re* numbers, becoming independent of the viscosity. For open-channel flow the general rule is that a flow is fully turbulent if $Re > 2100$ [11]. The

characteristic length used to determine Re for open-channel flow is the hydraulic diameter, D_h(m), defined as

$$D_h = 4 * A_c/P_w \qquad (1.6)$$

where P_w(m) is the total wetted perimeter of the cross-sectional area. By noting that if the cross-section is of a circular shape and the whole cross-section is wetted, as in pipe flow, the hydraulic diameter would be equal to $4\pi R^2/2\pi R$, which is equal to $2R$, or the diameter.

The large cross-sectional areas and flow rates associated with rivers typically place open-channel flows in the turbulent regime as sub-critical flow. According to design, some sections of hydraulic structures, such as the spillway chutes on hydroelectric dams, experience flows that are super-critical, with induced and controlled hydraulic jumps occurring immediately downstream [11,14]. In general these areas should be avoided for hydrokinetic turbine deployment.

1.4 River In-stream Energy Converting Technology

The effort to develop devices that harness hydrokinetic energy has received government support thanks to a series of acts offering funding for research into technologies that can compete in the energy generation field. Results on the environmental criteria and efficiency of resource use are starting to become available as progress in this field continues. A comprehensive data base of current and forthcoming technologies intended for extracting energy from water can be found at the Department of Energy's Energy Efficiency and Renewable Energy Wind and Water Power Program site (http://www1.eere.energy.gov/windandhydro/hydrokinetic/). Among the various devices being considered, hydrokinetic turbines are making promising headway. Note that the term RISEC, for river in-stream energy conversion, is contained within the field of hydrokinetic turbines.

It is important to realize that hydrokinetic energy is not only found in rivers but also in currents generated during the transition of ocean tides. In recent years this technology for use in the marine

environment has received more attention. In principle, the devices intended for use in rivers are primarily going to vary in scale and will not have to address the bi-directionality found in the flow of marine currents.

As with wind turbines, two mechanisms exist to extract the hydrokinetic energy found in the flow of the water. By obstructing the path of the fluid flow, a drag force resulting from the shape of the blade can be used to generate the necessary torque for a generator. As recapitulated by Twidell and Weir [15], for an ideal drag-based wind turbine in an infinite stream of fluid, the maximum obtainable power extraction efficiency of the turbine alone is close to 20%. In comparison, by using lift forces that can be generated on the blades, the turbine power extraction efficiency can reach upwards of 40%. This is a significant improvement towards the idealized maximum extractable fraction by a single turbine of 16/24, or approximately 60%, commonly referred to as the Betz limit. Under conditions where the size of a hydrokinetic turbine is small in comparison with the cross-sectional area of interest, similar turbine extraction efficiencies can be expected. Only turbines making use of lift forces generated around blade foils to extract the power from the flow were considered in this study.

Devices are designed to have an operating range that begins once a minimum threshold, or cut-in speed, is reached. For the lift driven turbines, this cut-in speed is reached once the component of the lift force acting along the plane of rotation exceeds the component of the drag force that is acting in the opposite direction to the lift, as well as the internal friction found in a gearbox if one is used and the resistance found in permanent magnet generators, referred to as the cogging torque of the generator. Since the cut-in speed is determined by several factors addressed in the design of the generator and blade shape, it constitutes a functional and economical constraint on the machine. In the presence of speeds below this cut-in speed, the device will not generate power. Once a sufficiently fast flow is present and rotation of the blades is induced, the extracted power can be

determined through use of equation (1.2) if the relation between the energy generating efficiency and the velocity is known.

From experience gained in the wind turbine industry, it is known that the extraction efficiency of a turbine blade is dependent on the tip speed ratio of a device (λ). This ratio is defined as,

$$\lambda = \frac{R\Omega}{V} \qquad (1.7)$$

where R(m) is the radius of the turbine, Ω(rad/s) is the rotating angular velocity, and V in this case is the mean velocity of the undisturbed flow over the cross-sectional area of the device. It is important to try to maintain a constant value of λ in the operating range of a device. That is, the tip speed ratio should be maintained near the value that yields highest efficiency. From equation (1.7) it is seen that by allowing the turbine blades to spin at a variable angular velocity that proportionally changes as the oncoming velocity changes, a constant tip speed ratio can be achieved. A constant tip speed can also be maintained by allowing the blades to change the angle at which they "attack" the oncoming flow as the flow velocity changes. Having this flexibility that allows for varying the pitch of the blades can be used to adjust the forces acting on the blades and consequently the angular velocity of the blades.

The total efficiency of a device in generating power must take into consideration other factors besides the mechanical extraction capabilities. The quality of the electrical generator and the effectiveness of transporting the energy to shore and necessary voltage step-up through use of a transformer; all add to the global efficiency of energy extraction.

A device also has an upper limiting constraint. Once flow speeds reach the normal maximum speed for which a turbine system has been designed, it is said that it has reached its rated speed. Depending on the design of the system, the behavior of a turbine in flows above the rated speed will vary.

An idealized performance curve for a hydrokinetic turbine as a function of the oncoming flow speed is shown in figure1.2. This particular curve corresponds to a Tocardo T50-A turbine, where the performance points are based on field measurements taken at a commercial deployment site in Den Oever, The Netherlands [16]. The device has a cut-in speed of 0.7m/s, a rated speed of 3.5m/s, and an efficiency of approximately 40% in the region between the cut-in speed and the rated speed. The behavior at water speeds above the rated speed varies between devices and the particular turbine performance shown in figure 1.2 should not be taken to represent all of the devices. It does however show the detrimental effects on the extraction efficiency that can occur above the rated power speed.

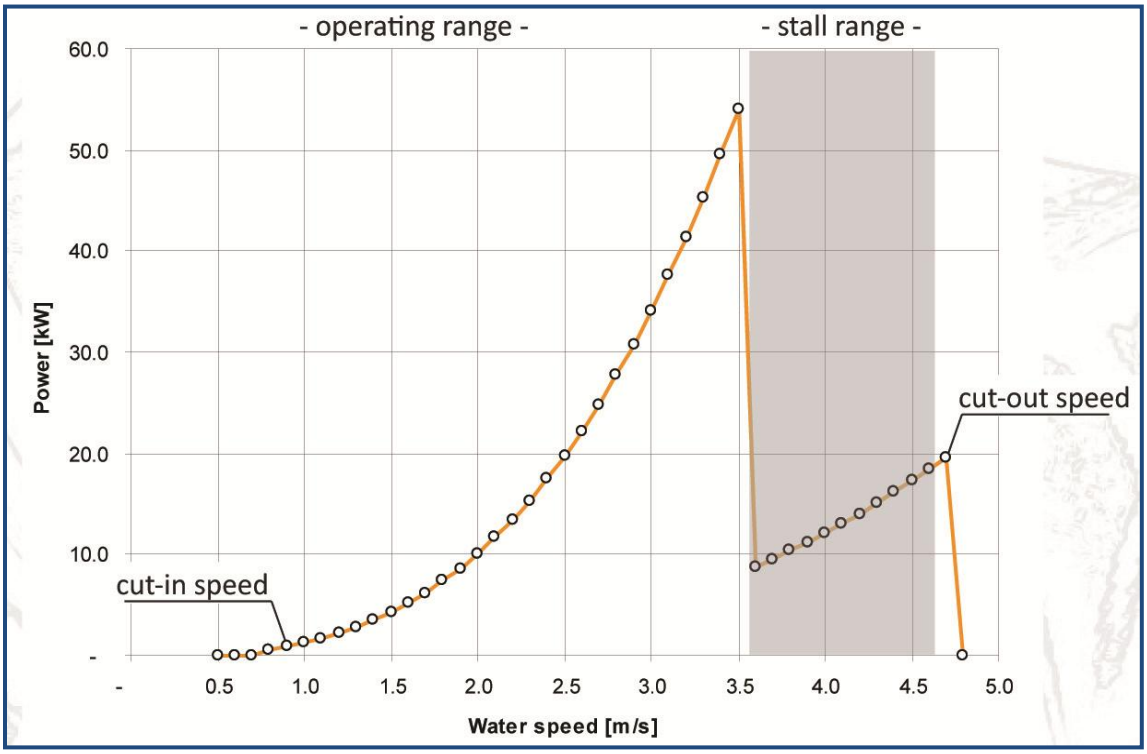

Figure1.2 Idealized performance curve for the Tocardo T50-A turbine.
Image from Tocardo International BV [17]

Presently, a handful of companies exist that either manufacture or are in stages of demonstrating devices intended specifically to work in river settings. Following is a list of the companies offering a product or claiming to have a finished product in the foreseeable future, the characteristics of their technology, and the known stage of development:

Company: Ocean Renewable Power Corporation, LLC (ORPC) [18,19]

Turbine Model: RivGen™ Power System

Type: Cross-flow horizontal axis turbine

Rated Power: 30kW (initial design)/50kW (future goal) at a flow speed of 3m/s; cut-in speed 1.5m/s

RPM: 30-60

Rotor Diameter: 1.5m

Rotor Length: ~(2x4.4)m

Number of Blades: 4 per rotor

Generator: Variable speed permanent magnet generator

Gear Box: No

Anchoring: Barge or pile mounted (Site specific)

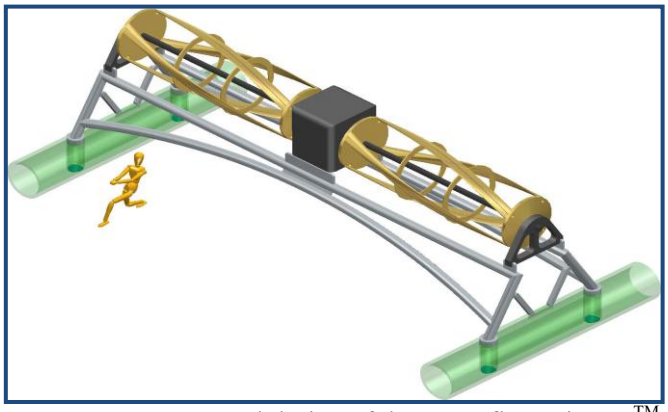

Figure 1.3 Conceptual design of the cross-flow RivGen™ Power System.
Image from ORPC, LLC [18]

Current Status: This device is not currently available. ORPC is under licensing processes for a site on the Tanana River, near the community of Nenana, Alaska, to develop and test the RivGen™ Power System. They are working under collaboration with the Alaska Hydrokinetic Energy Research Center at the University of Alaska Fairbanks. Environmental and site characterization continues to date. The foreseen installation of a turbine at this site is in June 2012. A beta-prototype of the company's TidGen™ Power System intended for shallow tidal sites has been tested off of a barge moored in Cobscook Bay, near the city of Eastport, Maine.

Company: New Energy Corporation Inc. (New Energy) [20]

Turbine Model: EnCurrent Power Generating System

Type: Vertical axis turbine

Rated Power: 5/10/25/125kW at a flow speed of 3m/s for high speed models and 2.4m/s for low speed models; cut-in speed 1.5m/s; cut-out speed 3.25m/s for high speed models and 2.6m/s for low speed models

RPM: 90/90/40(22.4) at rated current speeds for the 5/10/25kW turbines; ( ) denotes low velocity model parameters

Rotor Diameter: 1.52/1.52/3.40(4.83)/7.6(10.8) m

Rotor Height: 0.76/1.52/1.70(2.41)/3.8(5.4) m

Number of Blades: 4-5

Generator: Permanent magnet generator

Generator Output: 0-300V

Gear Box: Yes, above waterline

Anchoring: Barge mounted

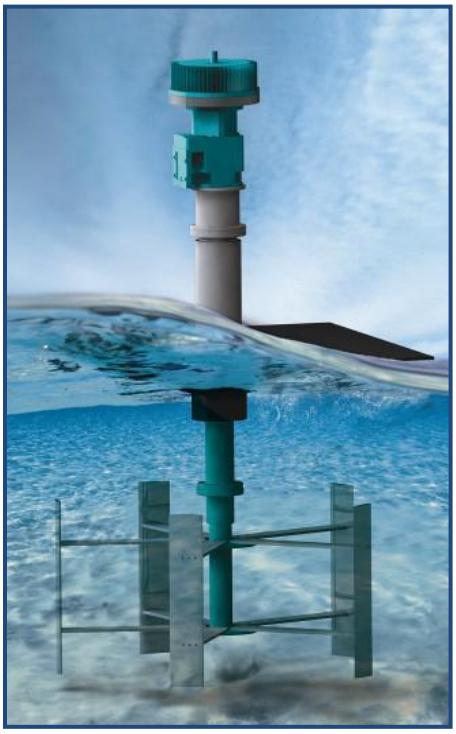

Figure 1.4 Conceptual image of the vertical axis EnCurrent Power Generating System. *Image from New Energy Corp. Inc. [20]*

Current Status: The 5/10/25kW turbines are available and include the appropriate inverters for both a grid-tie or off-grid system only. Deployments of a 5kW generating system have occurred at a site on the Yukon River, near Ruby, Alaska, and on the Winnipeg River at Pointe du Bois, Manitoba, Canada. Deployment of a 25kW generating system also took place at the same site on the Winnipeg River and a deployment is currently being monitored on the Yukon River near the town of Eagle, Alaska. Data regarding the power generating functionality of the

devices for these deployments is sparse but reports describing deployment experience and development of the device are available from the company.

Company: Hydro Green Energy LLC (Hydro Green) [21]

Turbine Model: Hydro^{+TM}, Current^{+TM}

Type: Shrouded horizontal axis turbine

Rated Power: 98kW at a flow speed of 3.5m/s; cut-in speed 1m/s

RPM: 21 at rated speed

Rotor Diameter: 3.66m

Number of Blades: 3

Generator: Unknown

Gear Box: Unknown

Anchoring: Barge mounted

Current Status: Availability of the device is unknown. One full scale unit has been deployed in the near vicinity of the powerhouse of the Lock and Dam No.2 on the Mississippi River, near the city of Hastings, Minnesota. Data regarding the power generating functionality of the device for this deployment is not available. The company appears to be reorienting the focus of their efforts to low-head conventional turbines.

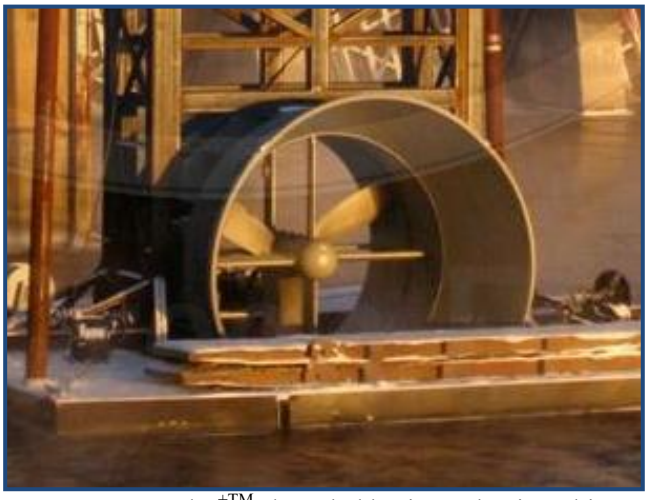

Figure 1.5 Hydro^{+TM} shrouded horizontal axis turbine. Image corresponds to the deployment in front of the Lock and Dam No.2.
Adapted image from Hydro Green Energy LLC [22]

Company: Free Flow Power Corporation (FFP) [23-25]

Turbine Model: SmarTurbine^{TM}

Type: Shrouded horizontal axis turbine

Rated Power: 40kW at a flow speed of 3m/s; cut-in speed 1m/s; cut-out speed 4m/s

RPM: 38 at 2.25m/s, less than 70 at 4m/s

Rotor Diameter: 3m

Number of Blades: 7

Generator: Variable speed permanent magnet generator

Gear Box: No

Anchoring: Barge or pile mounted (Site specific)

Current Status: This device is not currently available. A barge mounted 1.4m rotor diameter proof of concept turbine has undergone testing. A barge mounted full-scale prototype was scheduled to be commissioned by November of 2010 and deployed through June 2011 at one of the sites being licensed by FFP. Further development of an experimental deployment of four or more pilings with mock or power generating turbines is scheduled to begin in late 2011 at this same site on the Mississippi River, near Baton Rouge, Louisiana.

Figure 1.6 SmarTurbine™ shrouded horizontal axis turbine.
Image from FFP Corp. [23]

Company: Tocardo International BV (Tocardo) [17,26]

Turbine Model: Tocardo Aqua

Type: Horizontal axis turbine

Rated Power: 50/150kW at a flow speed of 3.5m/s; cut-in speed .7m/s; cut-out speed 4.8m/s

RPM: 72/60 at rated flow speeds

Rotor Diameter: 2.8/4.5 m

Figure 1.7 T50-Aqua horizontal axis turbine.
Adapted image from Tocardo International BV [27]

Number of Blades: 2

Generator: 14/22 pole, variable speed permanent magnet generator

Generator Output: 0-400V

Gear Box: No

Anchoring: A connecting flange offers the ability for a multitude of configurations including barge, pile or overhead structure mounts (site specific)

Current Status: These devices are currently available. A T50 turbine is currently operating at a demonstration site in Den Oever, The Netherlands. A T150 unit is soon expected to be operational at another site in The Netherlands.

As of now, some manufacturers have passed the stage of proving and testing their technology, with successful deployments to show. There are finer details on the performance and experience gained that are still uncertain but a particular question of concern that remains is the environmental impact that can be expected from their hydrokinetic devices. Currently there are experimental studies funded by the U.S. Department of Energy (DOE) being carried out by the Pacific Northwest National Laboratory (PNNL) [28] and EPRI [29] to try to answer this query. PNNL is working to develop an Environmental Risk Evaluation System to act as a tool for assessing the impact of an installation at a particular site and is also working on simulating the result of impact with a RISEC turbine. Flume tests on three different turbine designs are being led by EPRI intended to determine the likelihood of strike on fish by the rotor blades and the response of the fish to the presence of the device.

The devices being examined in the EPRI study are a 5kW EnCurrent turbine, a spherical turbine intended for use in water transmission pipes with 4 blades manufactured by Lucid Energy and a horizontal-axis ducted turbine. The second quarterly technical progress report from EPRI [30] released in June of 2010, reported that testing on the EnCurrent turbine had been performed. A total of 205 Atlantic salmon smolt and 300 American shad were used in the experiments. Both the

salmon smolt and the shad were tested by releasing the fish upstream from the turbine. Additional testing for the shad was performed by releasing them downstream of the turbine and allowed to swim upstream voluntarily. Out of the shad, 130 tried to swim up the flume, many on multiple occasions. Preliminary results showed no evidence of injury and no deaths were recorded. Results from fish tagging and filming of the experiment are pending.

Fish survivability testing was funded by Hydro Green for the Hydro^{+TM} deployed on the Mississippi River. Tagging and recapturing of approximately 680 fish of varying sizes was done by Normandeau Associates. Results published by Normandeau Associates [31] indicated that no injuries were present on any of the recaptured fish that could be attributed to a rotor blade strike. The report concluded on 99% fish survivability and that the hydrokinetic device presented little if any impact on fish in the area.

1.5 Hydrokinetic Resource Assessment Literature Review

With the levels of variability that can be encountered in any given reach of a river, the data needed for the development of a hydrokinetic energy generation site becomes highly site specific. To date, such assessments of hydrokinetic resources are limited, but nevertheless increasing.

In 2008, under sponsorship of the Alaska Energy Authority, EPRI [10] conducted a resource assessment to determine the feasibility of implementing RISEC devices at sites in Alaska. The areas of interest were chosen to embrace the variety of parameter combinations that could be encountered in typical locations throughout the state. Conceptualized deployments and economic models returned simple payback periods between 3-9 yrs for commercial sized plants ranging between 40 to 500kW at sites varying in terms of isolation and access to transmission lines. The cost per installed kW for the commercial plants was calculated to be between $3,071-$7,474, with annual operational and maintenance (O&M) costs at 2-7% of the capital investment. The authors

noted, however, that a high level of uncertainty masks the findings, due to a lack of finer details pertaining to the assessed resource.

The anticipated relative ease for deploying hydrokinetic projects in man-made channels, led Thielmann [32] to conduct a resource assessment of the hydropower available in trapezoidal laterals that make up part of the Columbia Basin Irrigation system. Sponsored by Grant County Public Utility District No.2 (Grant PUD), the possibility offered by exploiting three sites through the use of hydrokinetic turbines was studied and compared against the potential of using conventional low head hydropower turbines. Two sites where flow check stations are located and one site where a control station once existed were considered. The concatenation of a system that would replace the existing control stations with hydrokinetic turbines, while providing flow control through power extraction, experienced limitations due to the low flows found in the lateral channels. It was determined that further civil work would be required to bring the flow velocities to a useful level within the rated functionality of the stream. In turn, the narrowing of the channels was paralleled with diminishing energy potential that could be extracted without causing the flow to "choke," which would result in an alteration of the upstream depth and could have effects propagating into other sections of the irrigation system. The limitations posed by the small laterals and the higher cost associated with early emerging renewable energy technology made low head conventional hydro turbines a more economical alternative per kW of generated power at these sites. In general, using low head turbines offered a significant increase in the amount of power that could be harnessed, varying between 10 to 50 times that expected from hydrokinetic devices. However, to make use of the full potential, these low head projects also presented an increase in the up-front capital cost, around 10 to 30 times more than estimated for the hydrokinetic deployments. Nonetheless, the duality found in the functionality of hydrokinetic devices to provide flow control and generate power should not be dismissed. Having access to the larger canals with higher flow rates and faster velocities could prove worthwhile.

Reporting on the progress made by the Department of Engineering Sciences at Uppsala University, Sweden, in a quest to establish a testing site for hydrokinetic energy extraction, Lalander and Leijon [33] presented work associated with the development of a test turbine/generator unit and the numerical modeling of a chosen site. Results have been published on the simulation of power extraction from the flow going through the dredged Söderfors channel on the Dal River. The reach exists between a hydroelectric plant upstream and a reservoir lake for a hydropower facility downstream. Simulating 100kW power extraction from three turbines placed 400m downstream from the powerhouse and four more near the entrance to the lake, approximately 1km downstream, led to a calculated surface level increase of 0.02m upstream of the first set of turbines. The surface level fluctuations due to the stage of the lake were reported to be an order of magnitude larger, ranging between ±0.2m, thus having a more significant impact on the head available at the upstream hydroelectric plant. Complete development of this site for testing of prototypes is expected.

Toniolo et al. [34] report on their methodology to assess the power density and stability of a 1260m long reach of the Tanana River, near the community of Nenana, AK. Using field measurements and a 2-D numerical model to simulate the reach, an average power density of 4,500 W/m^2 was calculated at a total river discharge of 1.141kcms, corresponding to a flow rate characteristic of late August, when field measurements were taken. As the Tanana River is a glacier fed river, it is characterized by heavy sediment load transport. The river bed can take on a shape consisting of wave-like dunes, and the deepest section of the river, the thalweg, can be unstable and shift with changing discharge and stage. For various transects along the reach, mean velocities, specific discharge, and velocity fluctuations were calculated using data acquired with an Acoustic Doppler Current Profiler (ADCP). A region approximately 800m long was found to be stable, with the remaining stretch showing signs that the thalweg might be shifting from one river bank to the other. This work is intended to establish a baseline of the river dynamics at this particular site, from

which the effects of introducing hydrokinetic devices can more appropriately be determined and understood. The site of interest falls within the area being licensed by ORPC for deployment of their RivGen™ Power System. In collaboration with other private industry partners, ORPC and the Alaska Hydrokinetic Energy Research Center (AHERC) at the University of Alaska, Fairbanks, are working to establish the Nenana Hydrokinetic Test Center within the permitted boundaries [35].

Documentation associated with proof of concept deployments for the EnCurrent system developed by New Energy Corporation Inc. has been made available by the company [36], and updates from FFP Corporation on site assessment characteristics, analysis of the preliminary mounting structure, and other generalities related to the development of their sites and turbine can be found in Quarterly Reports submitted to the Federal Energy Regulatory Commission (FERC) [24].

1.6 IIHR

Since the 1930's, IIHR at the University of Iowa has been involved in developing physical and numerical models used to study environmental effects of hydraulic structures and water pollutants. For close to thirty years, the institute has been studying and applying its knowledge to the environment encountered by migratory fish, particularly salmon, in the annual migration up and down the Columbia and Snake Rivers. From 1983 to the present time, Grant County PUD has been working with IIHR in efforts to reduce the impact of their hydroelectric dams.

The work that has been done in regards to Wanapum and Priest Rapids Dams and includes the design and implementation of a fish bypass system and spillway deflectors for Wanapum Dam, and the undergoing study and design of a top spill configuration intended as a fish bypass mechanism for Priest Rapids Dam [37-39]. Figure 1.8 provides visualization of these projects.

As an essential tool in these studies, IIHR has developed a computational fluid dynamic model of the tailrace of these two dams, as well as various physical models. Using field measurements obtained throughout the years of involvement, both the physical and computation fluid dynamics

(CFD) models have been calibrated and proven to be useful tools in the continuing research and applications being performed at IIHR.

A margin of accuracy is considered to be inherent in modeling work. Pertaining to the two stretches of river studied in this work, a limited distribution report was made accessible by IIHR [40] relating to the construction of a 1:100 scale, undistorted, fixed bed physical model of the powerhouse, spillway and over 4kms of the tailrace of the Wanapum Dam that occurred in 1996. Additional correspondence from IIHR included a letter report containing general flow pattern information on both tailraces. This letter report contained images showing velocity vectors determined from measured and numerically predicted values, primarily concerning the Wanapum tailrace, and a series of images of numerical simulation results contoured with velocity magnitudes for the Priest Rapids tailrace [41]. Two published literature sources on numerical simulations of the Wanapum Dam tailrace were found [12,42], one performed during the same research period when the aforementioned physical model was constructed [12] and a more recent modeling performed in 2008. No further information was obtained concerning the Priest Rapids tailrace.

Using results of field and physical model measurements taken along four cross-sections downstream from the Wanapum Dam (1,219m, 1,828m, 2,865m, 3,993m) [40] during the physical model's calibration process, the relative error of the average velocity between the two is found to have a median value of 2.1%. The average velocity was calculated by the authors as the average of measurements taken at 3/10 and 7/10 depths. This error should be expected to change for the different points along the water column and serves more as a general guideline. For the same calibration process, the median relative error of the water surface profile is found to be .045% based on the available results, with accuracy in the water surface profile of ±0.03m as reported by the authors.

In the published material referencing the numerical simulation that accompanied the construction of the physical model [12], a relative error of the velocity magnitude at 6/10 depth is reported, ranging between 5-10% for most of the data when compared between the numerical and field measurements. It is unknown as to how this range applies to the simulation performed close to fifteen years later, as it is not reported. Only visual representations presented for the measured and predicted velocity vectors are available for the more current simulations [41,42]. These images containing velocity vectors generally demonstrate a good level of agreement between the numerical and field measurements but offer limited information as they only present a rough quantitative scale.

The limited information obtained on the validation of the models used by IIHR hinders the ability to account for the margin of error existing in the numerical simulation results that will propagate through to the calculations of the power expected from a pilot scale deployment. Since a more concise and detailed analysis of the algorithms and techniques implemented by IIHR in their modeling falls outside the scope of this current work, the effects of the numerical simulation error are not further considered but have to be kept in perspective. This is a matter that needs to receive more attention if more detailed studies are intended to continue since the effects of the errors will grow close to three-fold as the velocity gets cubed and could lead to significant error margins in the final electrical power generation results.

a)

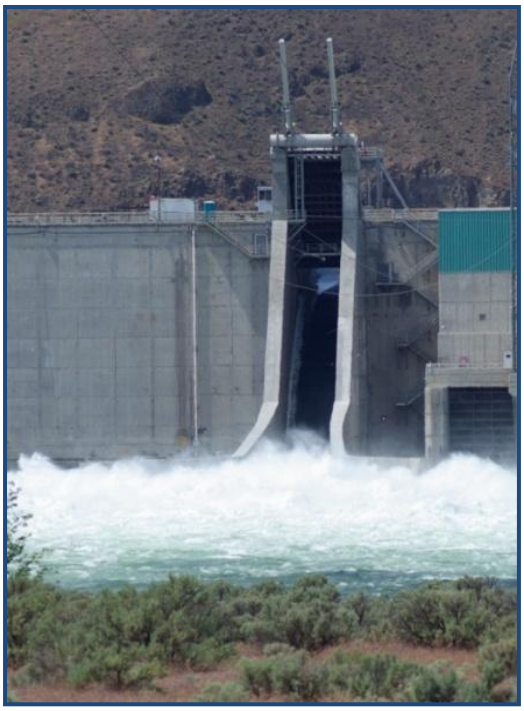

b)

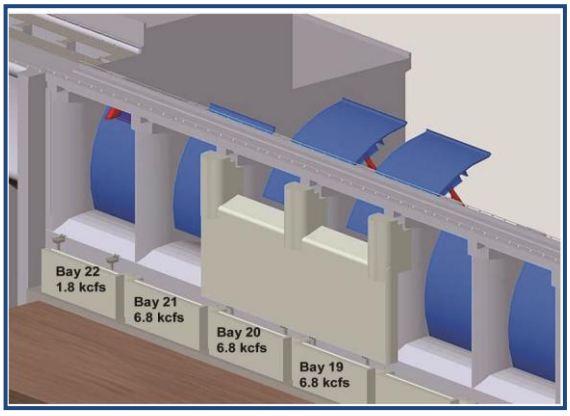

c)

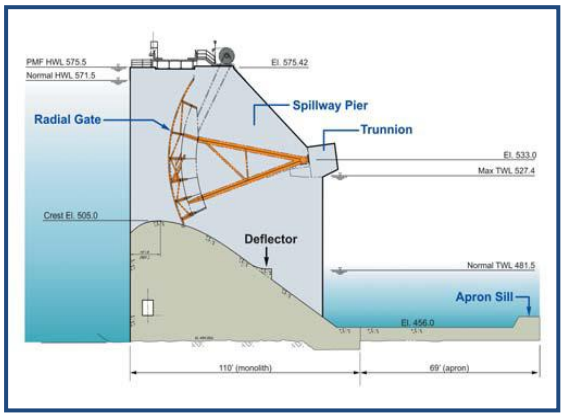

Figure 1.8 Projects in which IIHR has been involved for implementation at the Wanapum and Priest Rapids Dams: a) top-spill fish bypass unit constructed at Wanapum Dam in 2008, b) top-spill with bulk-head being studied, intended for fish bypass at Priest Rapids Dam, and c) installation of deflectors downstream of the tainter (radial) gates at the Wanapum spillway.

Image b) from Grant County PUD [39] and image c) from Griffith et al. [43]

II - Site Identification

As it has done for thousands of years, the vitality of the Columbia River continues to etch its path as it meanders North from its headwaters' nested in the Rocky Mountains of British Columbia, Canada, eventually turning south into the United States. As it travels into the United States it carves through the basalt layers that form the Columbia Plateau in the eastern region of Washington State and then turning westerly, delineating the border with Oregon State and joined by the Snake and Walla Walla Rivers, it forges a path through the Cascade Mountain Range to reach the Pacific Ocean. Approximately 225km east southeast from Seattle, WA, located in Grant County, Wanapum Dam transects the Columbia River at river kilometer 669. Roughly 30 river kilometers downstream, Priest Rapids Dam spans across at river kilometer 638.9. Figure 2.1 provides a geographical orientation of the location of the dams.

Figure 2.1 Location of Wanapum Dam (inset at upper right hand corner) and Priest Rapids Dam (inset at lower left corner) along the Columbia River.

Images from Google Earth

2.1 Priest Rapids Project

For the purpose of electricity generation, a coordination agreement exists between seven dams spanning across the Columbia River that tries to utilize the water resource flowing through the dams in such a way that the maximum amount of power is generated from each project in the most efficient manner. As opposed to unregulated rivers which have discharges governed by precipitation or temperature cycles that melt snow in the headwaters, the time scale of flow variations in a regulated river like the Columbia will not be weekly or seasonally, but in the order of days or even hours, closely matching electrical demand [33].

The Mid-Columbia Hourly Coordination Agreement (HCA) established in 1972 involves two federally operated projects, Grand Coulee and Chief Joseph, and the five dams that follow downstream: Wells, Rocky Reach, Rock Island, Wanapum, and Priest Rapids Dam. The complexity associated with the coordination effort is drawn from a series of interlacing environmental and economic considerations that have to be satisfied. In the course of a day the collective communication proceeds through the interpretation of signals sent from the projects to the mid-Columbia control computer which updates the generation control every four seconds. The effects of the coordination have to keep in mind sites further downstream, such as the lower dams on the Columbia and the nuclear generating facility at Hanford. The environmental impact of the dams is also taken into account, allowing for the seasonal discharges necessary for salmonid smolt outmigration to the Pacific Ocean and the control of water levels downstream of Priest Rapids Dam, in the Hanford Reach, during the Chinook salmon spawning season. In general, spanning from Grand Coulee Dam down past Priest Rapids Dam, the Columbia River is still expected to have discharge fluctuations with short time frames that closely match the electrical load requirement of each facility. Figure 2.2 shows the daily fluctuations typically associated with regulated rivers and correspond to those observed in the Priest Rapids tailrace from 2007 to 2009.

It is observed that during most of the year the flow going through the dams meets the demand felt at the powerhouse, with continuous spikes showing the night to day fluctuation.

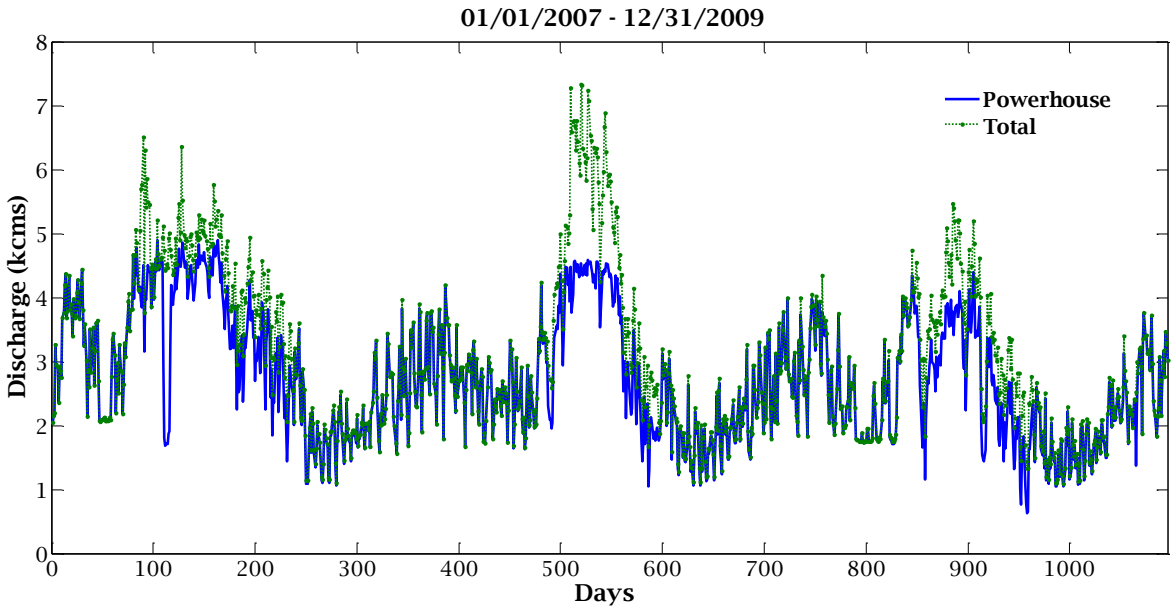

Figure 2.2 Daily average fluctuations of the total and powerhouse flow rates at Priest Rapids Dam. The data, obtained from Grant Country PUD, spans the period of time from 01/2007 through 12/2009 [44].

The Wanapum Dam consists of a 5,941-hectare reservoir and a 2,633-meter-long by 56.8-meter-high dam spanning the river. The dam consists of left and right embankment sections; left and right concrete gravity dam sections; a left and right fish passage structure, each with an upstream fish ladder; a gated spillway; an intake section for future generating units; a downstream fish passage structure in one of the unused intake sections (unit No. 11); a powerhouse containing 10 vertical shaft integrated Kaplan turbine/generator sets with a total authorized capacity of 1,038 MW; the Wanapum Dam Heritage Center; and three 230-kilovolt (kV) overhead transmission lines. The first transmission line is 2.5 kilometers long and connects to two switchyards of the Wanapum development. The second transmission line runs from one of the switchyards north for 50 kilometers to the Bonneville Power Administration's (BPA) Columbia substation, and the third runs south for about 27 kilometers and connects the Wanapum substation with the Priest Rapids substation [45]. Figure 2.3 shows an aerial photograph of the dam looking north, where the spillway is located in the lower left quadrant of the image and the powerhouse runs in a northward

direction at an angle offset from the spillway. The construction of the fish bypass unit had not been completed at the time this picture was taken but a red crane is seen where the unit now stands. The left embankment is located immediately upstream from the powerhouse and spans across to the right side of the image.

Figure 2.3 Aerial view of Wanapum Dam.
Image from Grant County PUD [46]

The Priest Rapids development consists of a 3,126-hectare reservoir and a 3,079-meter-long by 54.7-meter-high dam spanning the river. The dam consists of left and right embankment sections; left and right concrete gravity dam sections; a left and right fish passage structure each with an upstream fish ladder; a gated spillway section; a powerhouse containing 10 vertical shaft integrated Kaplan turbine/generator sets with a total authorized capacity of 855 MW; a fish hatchery; the Wanapum Indian Village; and three 230-kV transmission lines running from transformers at the powerhouse to the Priest Rapids switchyard located 1.6 kilometers away, then continuing for 10 kilometers to the BPA's Midway substation [45]. In figure 2.4, a photograph of Priest Rapids Dam shows the aligned spillway and powerhouse spanning across the river. The image captures spill occurring through bays 19-22 and surface upwellings in front of the powerhouse associated with

various units operating. The left embankment of the dam runs to the upper right hand corner of the picture.

Figure 2.4 Aerial view of Priest Rapids Dam.
Image from Grant County PUD [46]

2.2 Total River Discharge

With daily and seasonal discharge fluctuations dependent on a multitude of variables, a statistical approach was considered appropriate for the conducting analysis [10,33]. Operational data spanning from 2007 to 2009 were made available by Grant County PUD [44]. The data consist of daily averages of total, powerhouse, regulating spill, fish spill, and fish ladder discharge, as well as hourly power generation from the individual turbine/generator units for both dams. Additional total daily average discharge data for the Priest Rapids Project were found in the Columbia River Data Access in Real Time (DART) databank [47]. This databank is made available by the Columbia Basin Research and is provided to DART by the USACE Northwestern Division, Grant County PUD, and the Oregon Department of Fish & Wildlife. The data initially provided by Grant County

PUD and data obtained through DART for the same time period were compared to ensure accuracy. Discarding three dates without data from the DART records, the median absolute relative error between the data sets was found to be roughly 0.02% for both dams and the probability distribution of the total river discharge was calculated using fifteen years of daily average discharge measurements obtained through DART.

Figures 2.5 and 2.6 show the annual exceedance cumulative probability distribution for both dams, i.e. the probability that a discharge is greater than some given discharge. The tabulated probability distribution is found in Appendix A. Vertical lines have been placed at the 5%, 50% and 95% total river exceedance discharges. As should be expected, the distributions are very similar. Both dams are categorized as "run-of-the-river" dams, with reservoirs that are not intended to store a significant amount of excess water, thus requiring the discharge of the incoming flow in a short cycle of time.

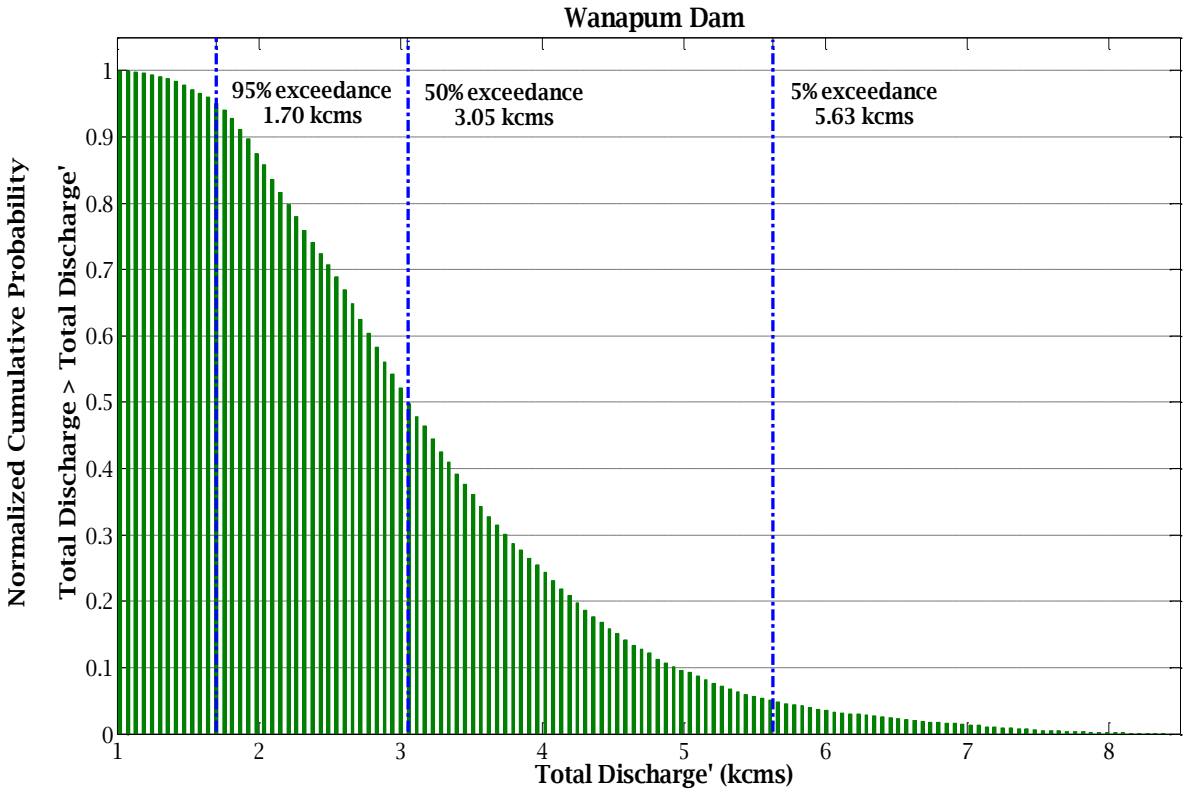

Figure 2.5 Annual exceedance probability of total river discharge through Wanapum Dam

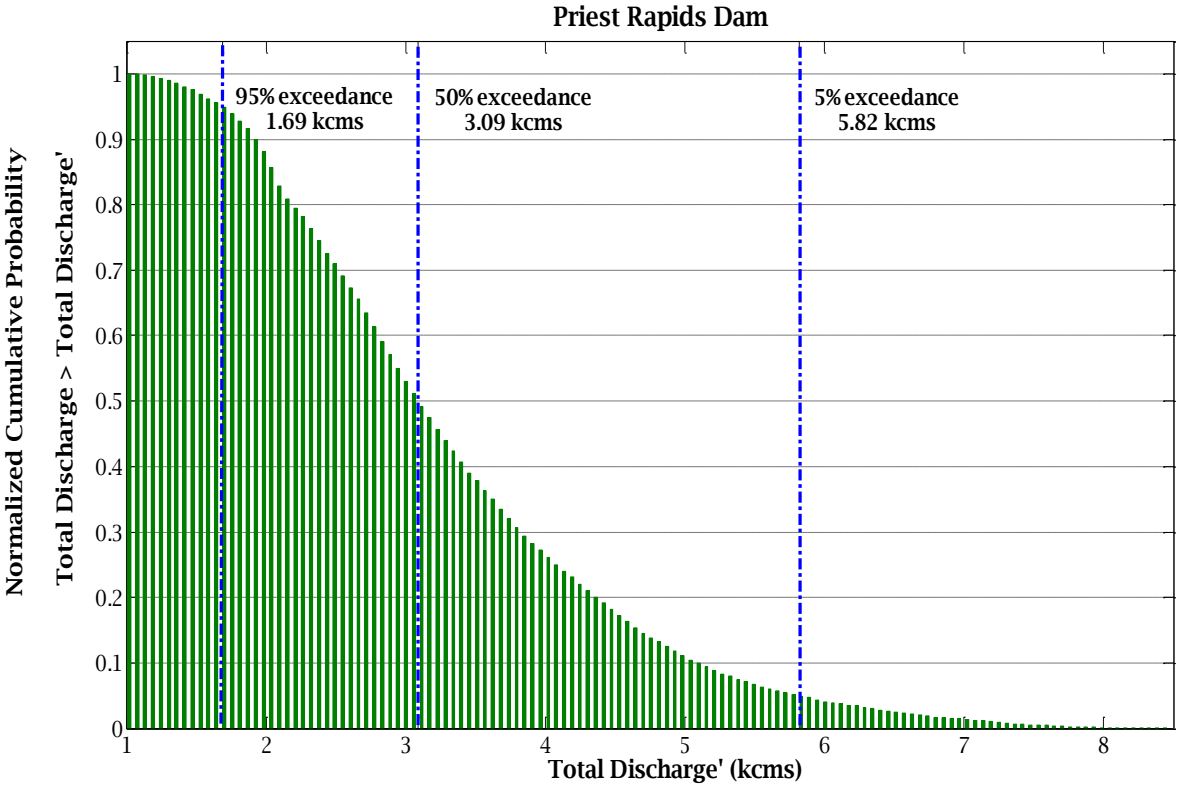

Figure 2.6 Annual exceedance probability of total river discharge through Priest Rapids Dam

2.3 Downstream Sites

As a first and very important step in analyzing the available resource, the images and computational results provided by IIHR were studied with the intention of identifying regions downstream from the powerhouse offering the optimal conjuncture of the following set of criteria: 1) velocities above 1 m/sec, 2) sufficient depth, 3) ease of access, 4) avoidance of regions prone to large scale dynamic fluctuations, 5) regions with sub-critical flow, 6) sensitivity to environment, and 7) river bed composition. As is common, the assignment of 'left' and 'right' when identifying locations is taken from the point of view of an observer travelling in the flow direction.

To investigate the chosen regions, a vertical data plane spanning across the river, i.e., a transect, was obtained from simulations representative of the 5%, 50%, and 95% characteristic discharges. The data from each transect contained steady-state (i.e. no time dependence) simulation results for

the time average of the three dimensions of the velocity and the position of the data node. This data was visualized and manipulated using Tecplot 360.

2.3.1 Wanapum Dam Tailrace

The configuration of the powerhouse, spillway, and fish bypass at the Wanapum Dam has a significant influence over the flow distribution that can be expected in the tailrace. Figures 2.7 through 2.9 show images generated from simulation results ran at river flow rates close to the characteristic exceedance discharges. The images are contoured with the resulting velocity magnitude at a depth of 1.5m below the free surface. The inset found in the images corresponds to a vertical transect approximately 600m downstream from the spillway face. The total distance shown is close to 1500m. As seen, depending on whether the spillway or the newly added fish bypass is operating, velocity distributions in the tailrace are highly altered. A comparison between figures 2.8 and 2.9 shows a significant decrease in velocities along the left bank when the spillway is operating, close to 50% less, although the flow coming from the powerhouse is 22% more (i.e., 3.7 versus 3.0 kcms). The simulation depicted in figure 2.7 with the fish bypass operating shows a large recirculation region in front of the spillway with high velocities found in the outlet of the bypass and along the left embankment. High velocities are also observed along the left embankment when only the powerhouse is active. A constriction is found in the river approximately 1400m downstream of the powerhouse (near the bottom of the figures).

The bathymetry of the tailrace is shown in figure 2.10. The reference level for the bathymetry is taken to be sea level. It can be seen how the left embankment was constructed close to perpendicular to the thalweg, defined as the line connecting the deepest points of successive cross-sections along the course of a river. Downstream of the left embankment the thalweg runs along the left bank (right side of the image) down to the constriction, from where it starts to shift over to the right bank (left side of the image). Separating the spillway pool from the thalweg is an elongated area of higher elevation running ~580m downstream alongside the thalweg. When the spillway is

not operating, this ‘rib’ appears to act as a funneling mechanism accelerating the bulk of the flow along a ~230m reach of the thalweg until the channel coming from the spillway pool and the thalweg join upstream of the constriction. As noted above, high velocities are found along the stretch of the thalweg immediately downstream from where the discharge of the fish bypass joins into the thalweg when fish spill occurs.

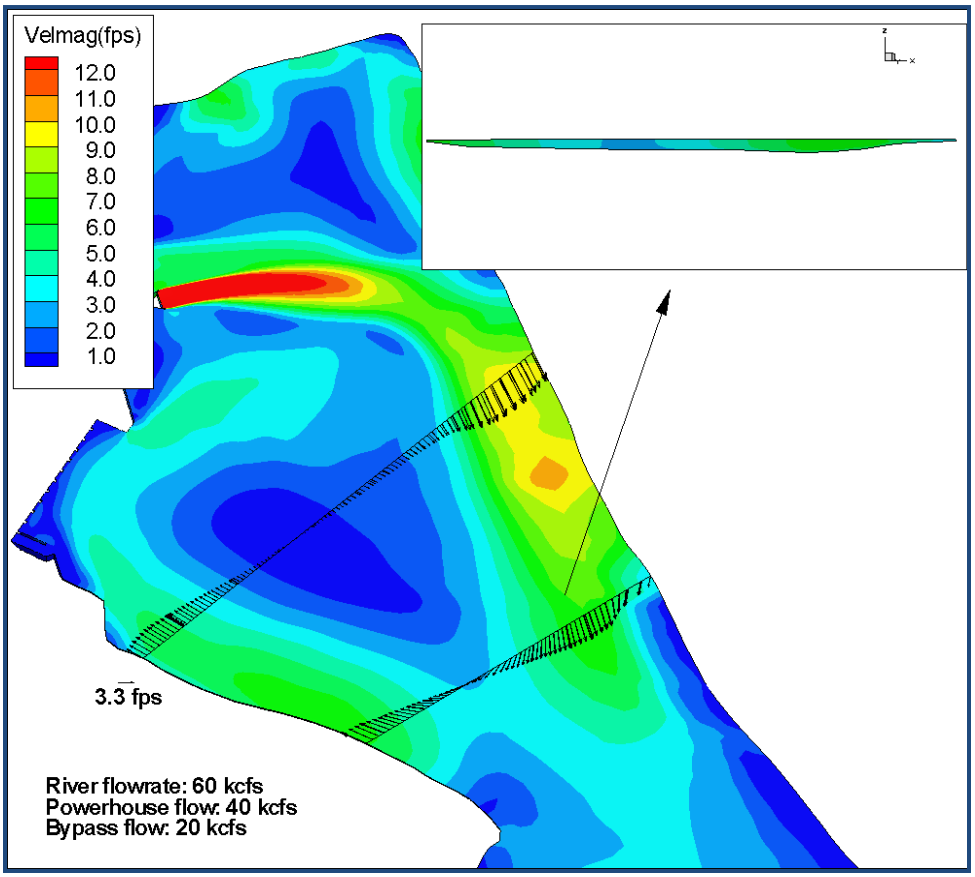

Figure 2.7 Wanapum Dam tailrace; total river flow rate of 1.7kcms with 0.566kcms flowing through the fish bypass. The fish bypass and the powerhouse are hidden by the velocity magnitude scale but the region of high velocity (next to the 3fps scale) clearly demarks the outlet location of the fish bypass.

Image courtesy of IIHR

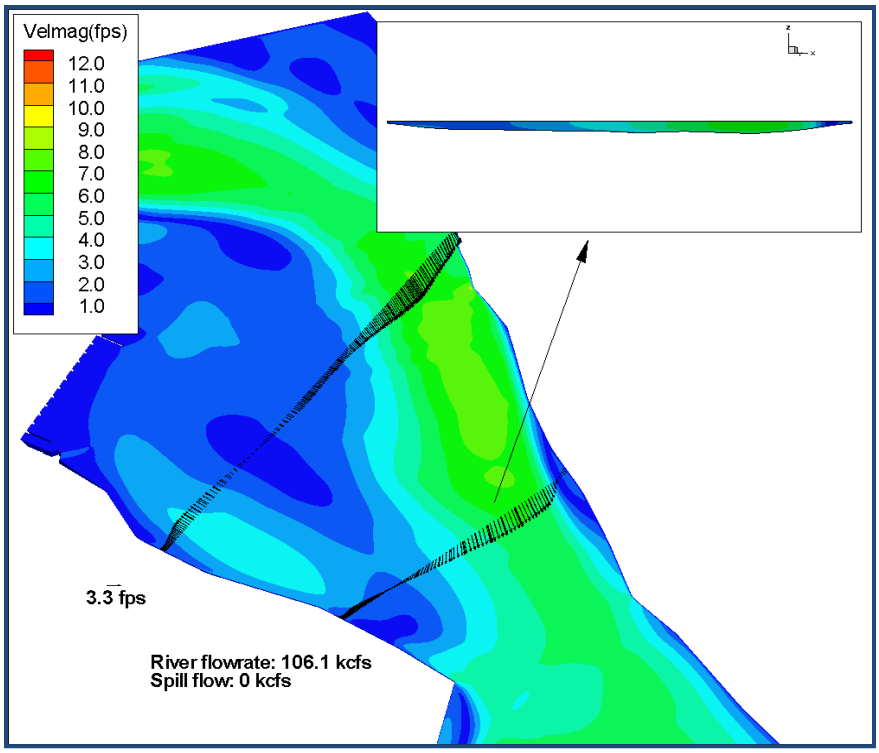

Figure 2.8 Wanapum Dam tailrace; total discharge of 3.0kcms with all of the flow going through the powerhouse. *Image courtesy of IIHR*

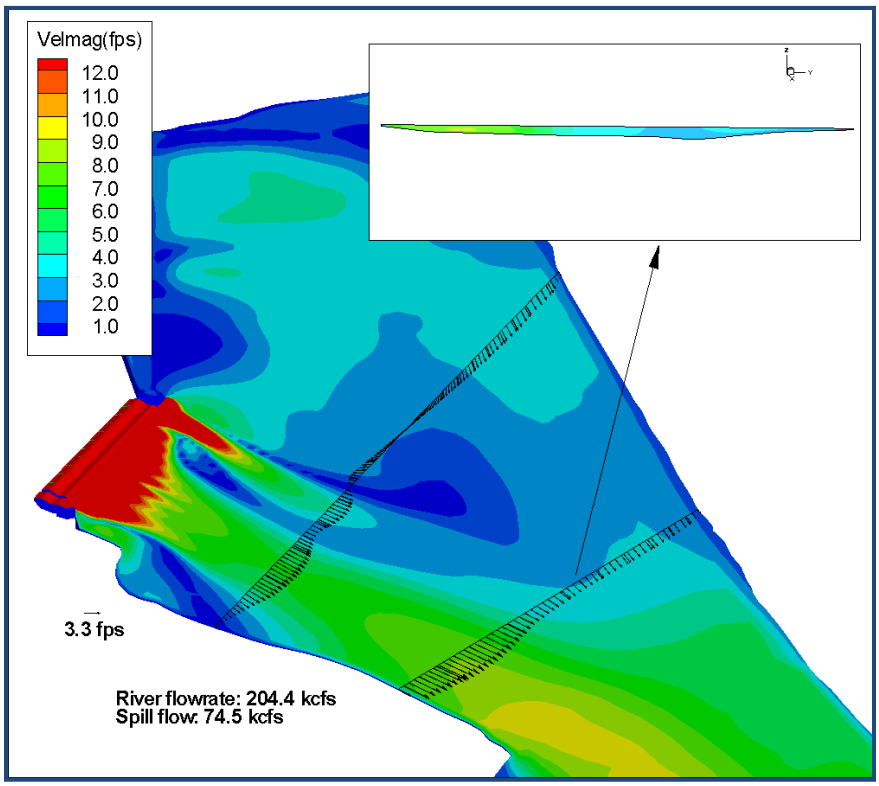

Figure 2.9 Wanapum Dam tailrace; discharge of 2.1kcms going through the spillway (clearly demarked by the high velocity contour) and a total flow rate of 5.8kcms. *Image courtesy of IIHR*

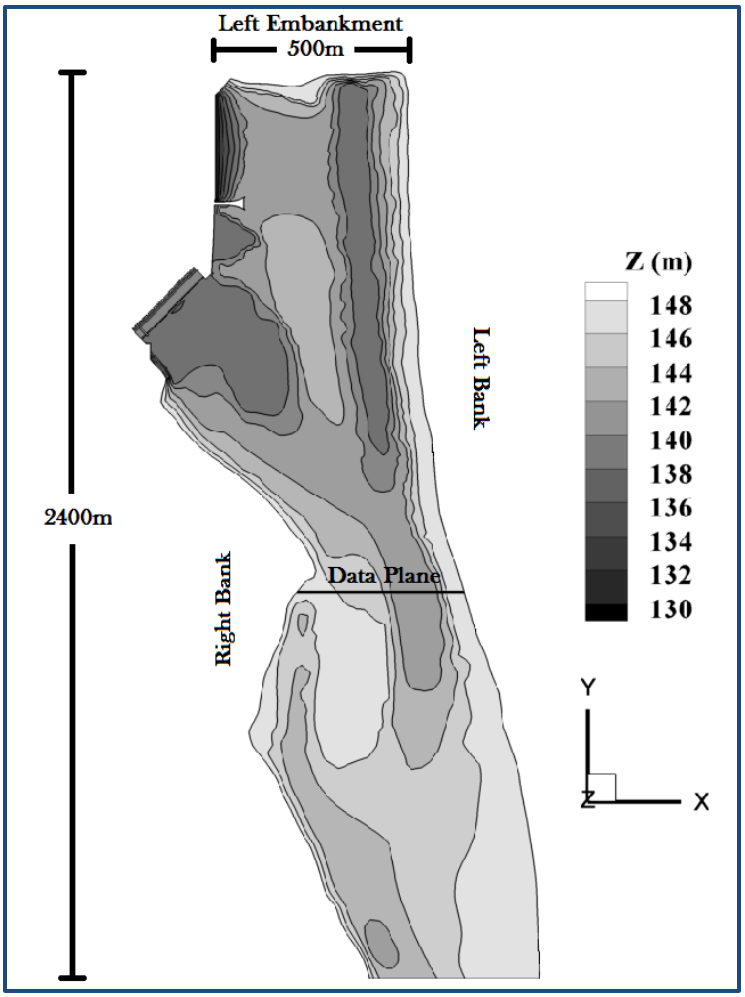

Figure 2.10 Bathymetry of the Wanapum Dam tailrace. The image is a top-down view of the bathymetry data provided by IIHR, visualized using Tecplot 360. The location of the data plane used to examine the chosen site is demarked by the black line approximately 1360m downstream from the left embankment.

The narrowing of the river at the constriction helps to distribute the flow across the river regardless of what structure is operating upstream. This constriction was identified by Sinha, Weber, and Odgaard [40] during the development of the undistorted 1:100 physical model of the tailrace as having a significant effect on how the flow behaves downstream from the constriction. By providing access to all of the dam's discharge and aiding to isolate the large scale recirculation region, the region immediately downstream of the constriction is chosen for further consideration. The location of the data plane used to exemplify the velocity distribution in this region is denoted in figure 2.10 with the dashed black line. Figure 2.11 provides a visualization of the data plane

contoured with the streamwise velocity, calculated using the ‘x’ and ‘y’ components of the velocity, for the low and high discharges, along with the independent bathymetry data.

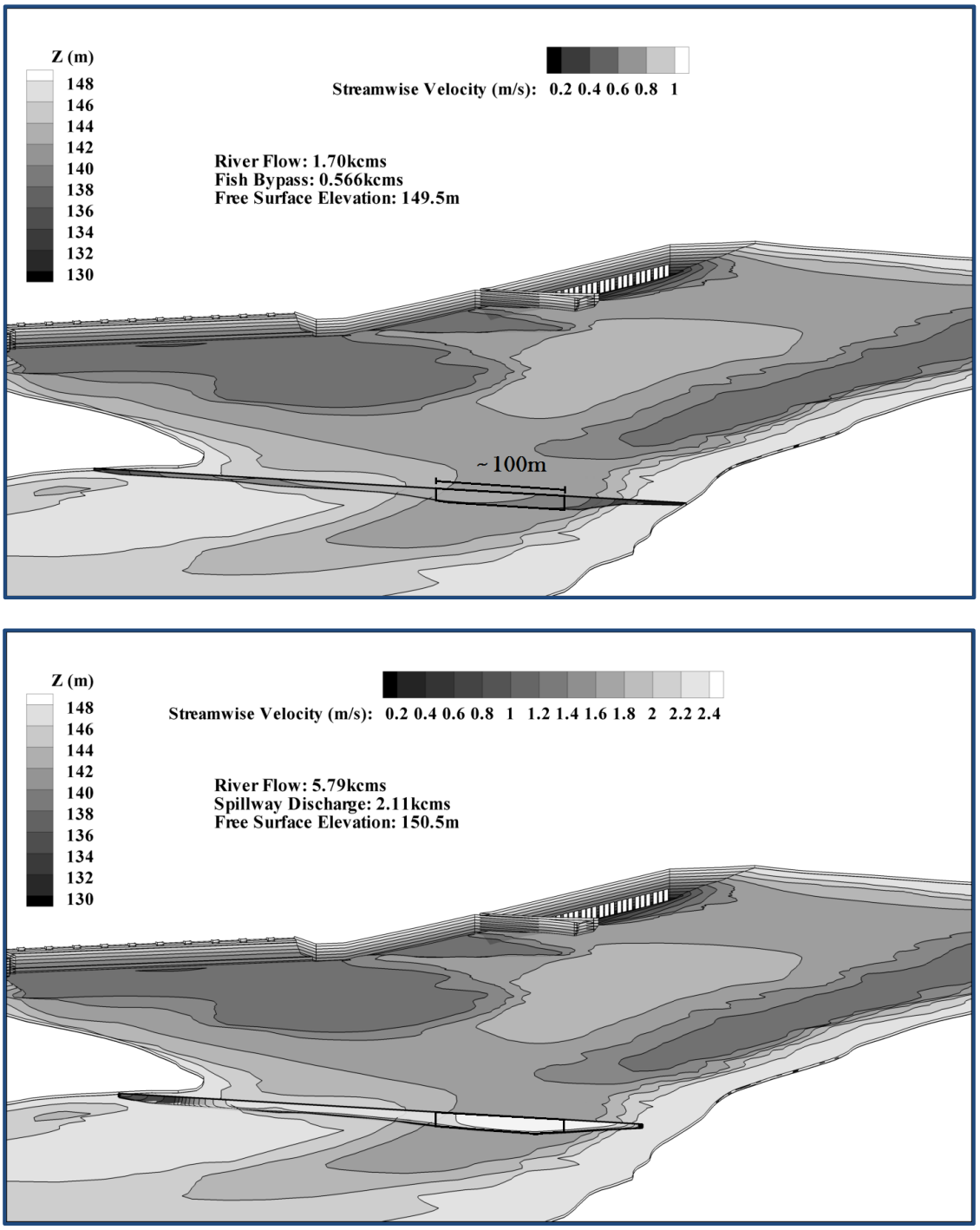

Figure 2.11 Data plane used to describe the downstream site in the Wanapum tailrace contoured with the streamwise velocity and tailrace bathymetry. a) ~95% and b) ~5% exceedance probability discharges. The siting region of interest studied is approximately 100m wide as shown in a).

From the fluid modeling results, velocity profiles are determined along the siting region of interest, and from these the depth-averaged velocity, V_d (m/s), is found. The cross-sectional area of the stream between successive locations (i.e., between successive velocity profiles) is a_c (m^2).The specific discharge, q(m^2/s), is calculated across this region using equation 2.1,

$$q_n = Q_n / T_{wn} \qquad (2.1)$$

where Q_n(m^3/s) is the discharge calculated as $Q_n = a_{cn} * \overline{V_d}$, with $\overline{V_d}$ (m/s) being the average of the depth averaged velocities at the two sides of the cross-sectional area considered, T_{wn} is the distance between the vertical velocity profiles , and n denotes the cross-section considered. Figure 2.12 shows plots for the maximum streamwise velocity, the specific discharge, and the depth across the siting region of interest for three characteristic discharges. The datum is taken at the edge of the site farthest from the left bank. It can be seen how q shifts from the right side of the region to the left side depending on the operational configuration. Figures 2.11 and 2.12 include the thalweg.

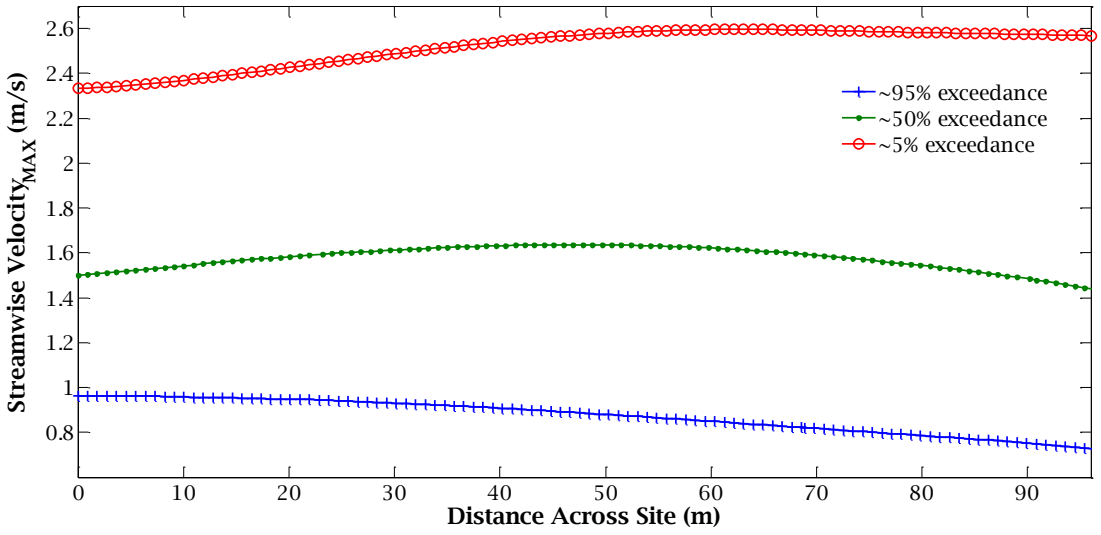

a)

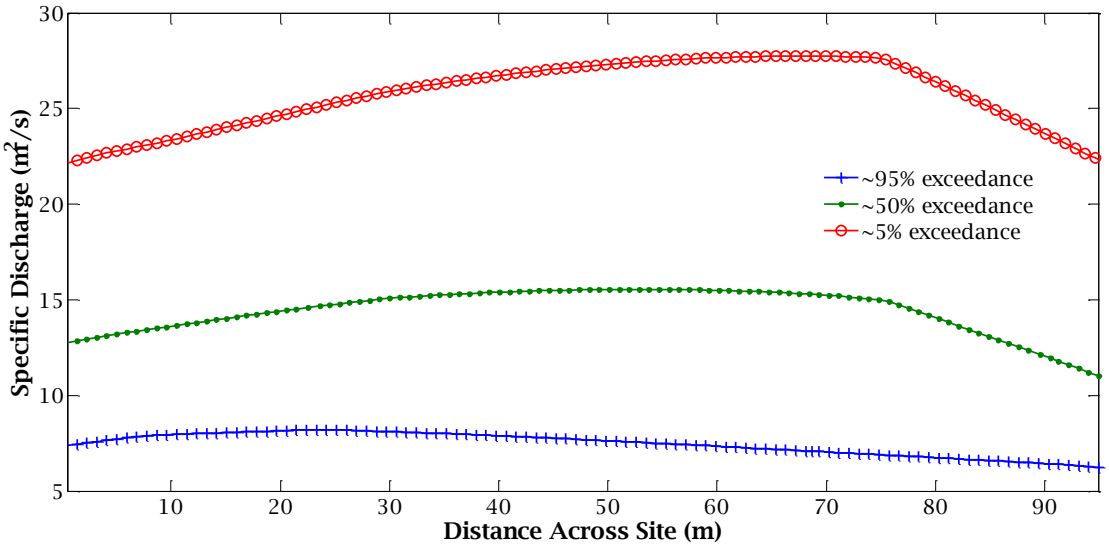

b)

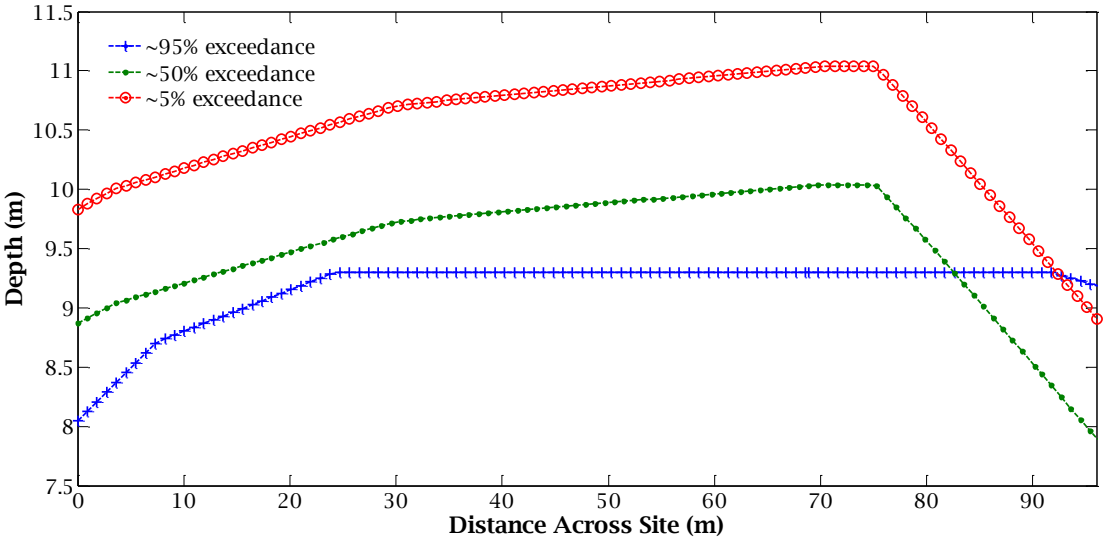

c)

Figure 2.12 Distribution of a) maximum streamwise velocity, b) specific discharge, and c) depth, across the downstream site in the Wanapum tailrace. Plots show results for the three river discharge simulations used to characterize the variations as a function of discharge. Note: the river bed bathymetry assumed by IIHR in the CFD simulations for low flow discharge (1.70kcms) is different than used in the medium and high discharge simulations[1].

[1]Differences in the data planes obtained from the simulations are seen by comparing figures 2.11a and b, and are noted in the depth distribution in figure 2.12c. The construction of the fish bypass is the most recent addition to the Wanapum Dam and to the bathymetry domain used in the numerical simulations of the tailrace; the available bathymetry data is matched exactly by the river bed elevation of the data plane for the low discharge (1.70kcms) that corresponds to the simulation with the fish bypass operating. The elevation of the river bed for the other two simulations, albeit similar between each other, cross below and are elevated at other points in relation to the bathymetry data. The difference between the river bed boundary for the other two planes is exemplified in figure 2.11b, where the plane does not extend all the way to the left bank and the region around the thalweg is narrower and not as broad at its deepest point in comparison to the plane shown in 2.11a. These differences are thus taken to demonstrate the continual progress in the modeling of these tailraces.

For each velocity data point along a velocity profile the point's power density is calculated as,

$$power\ density = \frac{1}{2}\rho u^3 \qquad (2.2).$$

For each cross-sectional area (a_c) the power is calculated by multiplying the area between two consecutive velocity profiles by the average of the depth-averaged power density of the two profiles. The total power (P) over the region of siting is then obtained by summing the power determined for each a_c over all of the cross-sectional areas,

$$P = \sum_n (a_{cn} * \overline{\frac{\rho}{2h}\sum_{i=0}^{h}(u^3)_i}) \qquad (2.3)$$

where the averaged term in 2.3 is taken to mean the average of the two velocity profiles that demark the vertical boundary of a_{cn}.

The total cross-sectional area (A_c) of the siting region of interest is calculated by summing the values of a_c across the region,

$$A_c = \sum_n a_{cn} \qquad (2.4).$$

A mean hydraulic depth (d_h) for A_c is calculated using equation 1.4, with the width (T_w) equal to the sum of T_{wn} across the region,

$$T_w = \sum_n T_{wn} \qquad (2.5).$$

An average *Fr* number for the region is calculated using the hydraulic depth in equation 1.3 and a mean velocity (V) calculated as:

$$V = \frac{\sum_n Q_n}{A_c} \qquad (2.6).$$

Although differences exist in terms of the bathymetry domain used during the different simulations, most of the parameters for the site increased proportionally for increasing river discharges. To account for the dissimilarity in bathymetry, the wetted perimeter (P_w) calculated from the low discharge data plane is used as a baseline and is adjusted accordingly based on the change in hydraulic depth for the higher discharges. This wetted perimeter is used in equation 1.6 to calculate the hydraulic diameter (D_h). The value for V calculated using equation 2.4 is used

along with D_h to calculate the *Re* number using equation 1.5. A value for the kinematic viscosity is taken at 11.26 °C, the average temperature of the tailrace waters as determined from data found through DART. Table 2.1 lists the main parameters of the cross-sectional area spanning the siting region. The value for P_w as calculated from the data extracted from the planes is provided in parenthesis alongside the value calculated using a baseline perimeter.

Table 2.1 Averaged and Integrated Parameters for the Downstream Site at Wanapum Dam for the Three Characteristic Flows

Total River Q (kcms)	1.70	3.00	5.79
$\sum_n Q_n$ (kcms)	0.73	1.41	2.49
P (kW)	264	1,690	7,492
A_c (m^2)	900.13	931.14	1017.10
V (m/s)	0.81	1.51	2.45
T_w (m)	97.23	97.23	97.23
d_h (m)	9.26	9.58	10.49
Fr	0.08	0.16	0.24
P_w (m)	114.47	115.11 (114.00)	116.94 (115.24)
D_h (m)	31.45	32.36	34.79
Re	2.02×10^7	3.88×10^7	6.75×10^7

2.3.2 Wanapum Dam Tailrace Dynamics and Frequency

Politano, Carrica, and Weber [42] carried out a multiphase numerical study on the performance of the deflectors that were added below the radial gates of the spillway chutes as shown in figure 1.8c. The results show that the tailrace dynamics are highly altered during times of spill because of surface jets that are formed when the super-critical flow that emerges from underneath the gates is redirected. This spill would otherwise plunge into the depth of the stilling basin. The “detour”

caused by the deflectors prevents air bubbles present in the forebay water, plus air bubbles entrained in the energetic regions of the stilling basin, from reaching deeper into the water column and dissolving, leading to increased levels of total dissolved gases (TDG) , which have been identified as a source of severe stress for fish.

Politano et al. found that when the effects on turbulence by the presence of the bubbles are accounted for in the numerical model, the results capture the dynamics of the flow observed in field measurements taken in the tailrace of Wanapum Dam after the deflectors were installed. The presence of bubbles in a flow has been reported as having the potential for either attenuating or incrementing turbulence levels depending on the bubble size [48]. For a scenario where the spillway flow accounted for 37% of the total discharge, the effect of the bubbles in suppressing turbulence is reported to have a dominant influence on the progression of the surface jets. The reduction in turbulence allows the surface currents associated with the jets to persist further downstream from the spillway at high streamwise velocity. Without the inclusion of the bubbles, these currents are found to rapidly dissipate near the spillway due to the higher turbulent mixing levels at the point.

The prolonged distance of the faster surface currents has an effect of increasing the entrainment of the slower surrounding fluid [42]. In comparison to field observations performed before the installation of the deflectors, it is reported that a larger portion of the powerhouse flow is redirected towards the spillway and away from the thalweg (running at the left). In figure 2.9, entrainment by the spillway jets is indicated, with a split of the flow coming from the powerhouse occurring around the shallow ‘rib’ as the fluid to be entrained moves to the right towards the spillway jets. This entrainment diminishes the flow going through the thalweg and hence causes the decrease in velocity noticed in the thalweg when the spillway is operating. Similarly, due to entrainment, in figure 2.7 the discharge through the fish bypass can be observed to generate a substantial recirculation eddy in front of the spillway if the latter is not operating.

A look through the available operational data shows that flow is generally discharged through the fish bypass from April through August. The design capacity for the fish bypass is 0.566kcms when the tailwater elevation ranges between 148.7m and 151.8m [49]. Since its installation in 2008, it has been operated at a mean discharge of 0.570 ± .04kcms during 98% of the spring and summer fish spill season. Fish spill is then reduced to a mean discharge of 0.05 ± .015kcms during the fall season. Regular spill is primarily observed to occur during the spring and summer time, when peak run-off from melting snow is the highest. Occasionally there is spill during other times of the year, but mostly due to maintenance or involuntary spill. The fish and regular spill cycles for the period of time from 2007 through 2009 is seen in figure 2.13.

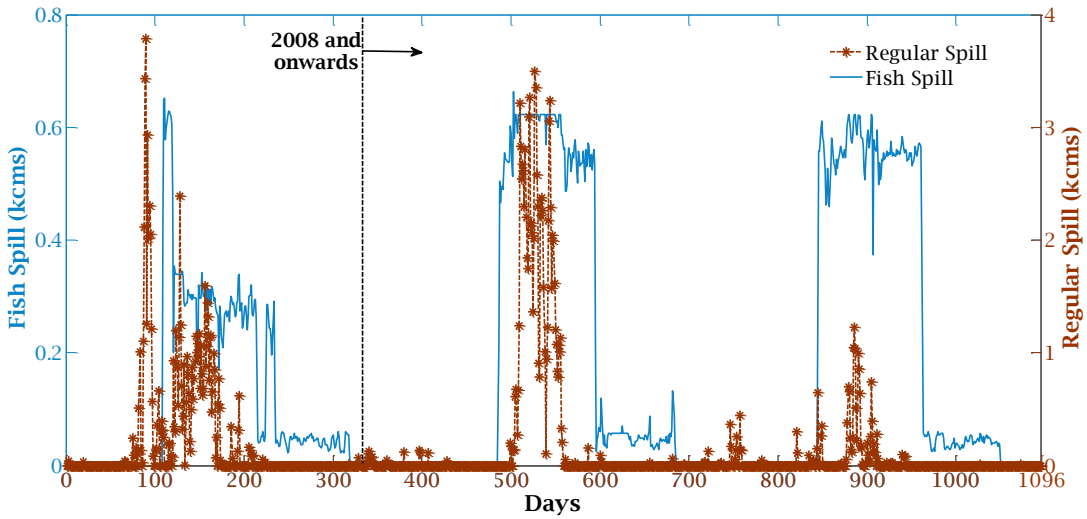

Figure 2.13 Fish and regular spill at Wanapum Dam. The seasons of fish spill occur during the spring and early summer but continue on until late fall. Peak regular spill is seen to occur during the late spring and early summer months.

During the months in which the fish bypass is operational, April through August, the frequency of a total river flow being lower than 1.8kcms is found to be zero. The spillway discharge was between zero and 0.075kcms, with a 55% frequency of occurrence, and 95% of the time the spill did not exceed 2.325kcms. Roughly 80% of the time when the spillway discharge was between zero and 0.075kcms, the river discharges ranged between 2.21 and 4.37kcms.When the fish bypass was not operated, 85% of the time there was no more than 0.81kcms of flow coming from the spillway. The detailed frequency distributions are found in Appendix A.

Considering the frequencies of occurrence in the time frame analyzed, it is concluded that the more probable scenario during the spring and summer fish spill season is one with the fish bypass operating at its design capacity and a total river flow rate between 4.01- 4.19kcms, with zero to 0.075kcms of regular spill occurring. This corresponds to a powerhouse operating between 76 and 80% of its hydraulic capacity (taken to be 4.53kcms), which is close to three time that coming from the powerhouse in the simulation with the fish bypass (with a powerhouse operating at 25% capacity). Additionally, during peak times of regular spill it is most likely that the fish bypass unit will be operating at or near its design capacity rather than not operating at all, as seen in figure 2.13.

Based on the frequency of configuration, the need for understanding the effect of having a large discharge coming from the powerhouse during fish bypass operation and that of having both the spillway and the fish bypass operating at the same time is highlighted. A high discharge coming from the powerhouse when only the fish bypass unit is operating may result in a different velocity distribution at the downstream site if the strength of the recirculation region is altered. During the times when all of the hydraulic structures are operating, the presence of the surface jet coming from the fish bypass may have an effect on the entrainment by the spillway surface jets and vice-versa. This may reduce the amount of flow attracted towards the spillway relative to that observed when only the spillway is operating and allow for more flow to follow along the thalweg. Consideration of these different configurations is important, since they have such an impact on the flow distribution in the tailrace and coincide with the time of peak power potential in the site.

Although the effects of configuration are more pronounced in the tailrace region upstream of the constriction, these effects are still present at the region chosen for a hydrokinetic turbine deployment. The recirculation that occurs in front of the spillway when the bypass is operating is seen to cause the flow direction to shift to the right relative to the general direction of the flow when only the powerhouse is operating. The flow from the spillway discharge is seen to align well

with the direction of the thalweg but with a concentration of higher velocities along the left side. Figure 2.14 shows a top-down close up of the velocity vectors for the three simulations. The black vectors correspond to the operation of the fish bypass plus powerhouse, the white vectors represent the spillway plus powerhouse configuration, and in between, the gray vectors represent the powerhouse only simulation. The vectors correspond to the vertical distribution of the velocity at the data nodes. In the inset in figure 2.14 the decrease in the velocity magnitude and shortening of the vector lengths as the river bed is approached can be seen by the retraction of the arrow head from the maximum vector at the free surface.

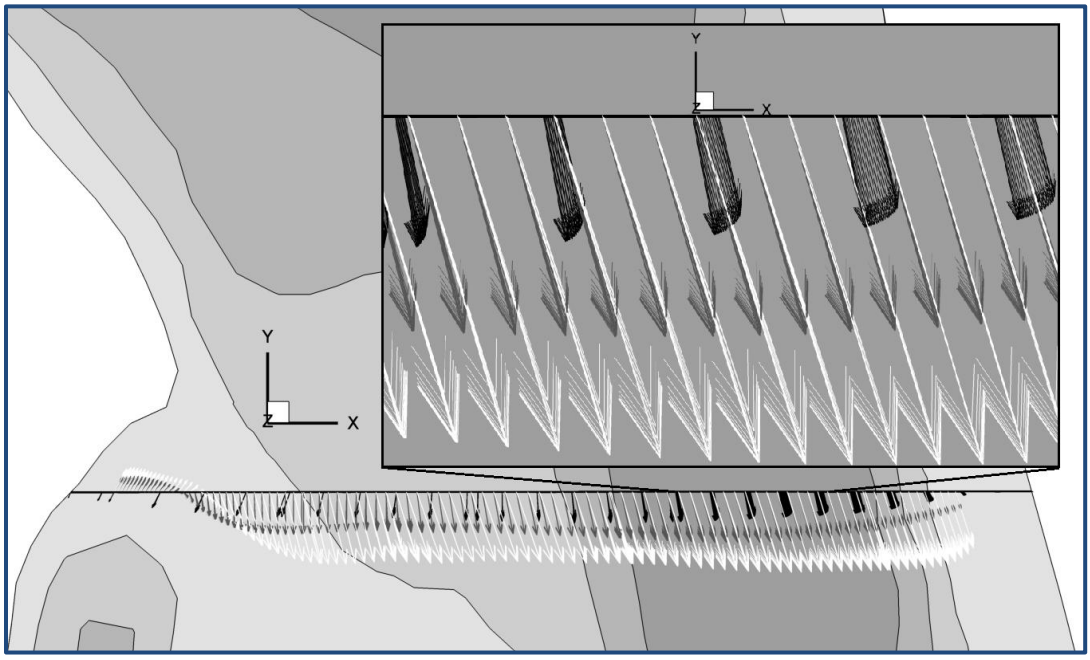

Figure 2.14 Velocity vectors across the river for the three discharge simulations at the Wanapum downstream site. Vector length follows accordingly to total river discharge (black[2] = 1.70kcms, grey = 3.00kcms, white = 5.79kcms). The vectors corresponding to the median discharge (grey) have a mean magnitude of 1.63m/s at the free surface for the vectors seen in the inset.

[2] The distribution of the data nodes in the simulation results that capture the operation of the fish bypass is not the same as that used of the other two simulations. This can be observed in figure 2.14, with the data nodes neither vertically aligned nor equally spaced across the whole data plane. This causes for the vectors (black) not to appear to fade into one as with the other two simulations where the data nodes are vertically aligned and equally spaced across the whole data plane. As stated above, the inclusion of the fish bypass into the bathymetry represents a new addition to the numerical simulation domain and this simulation can be considered to be more recent and appears to have been performed with a different technique of dividing the volumes of fluid.

In the case that a section of the tailrace in the stretch of the thalweg leading up to the chosen site is considered for future analysis, the need for further understanding of the tailrace dynamics for the case when the spillway, the fish bypass, and the powerhouse are operating alongside one another and when the bypass discharge interacts with varying flow rates coming from the powerhouse, is of more significance.

2.3.3 Priest Rapids Tailrace

The bathymetry of the river in this stretch is noticeably different than at Wanapum Dam. The stretch has shallower depths, a pronounced decrease in river width downstream from the dam, and thus a significant region experiencing faster velocities due to the reduced cross-sectional area. There is a shallow rock outcrop running for about 275m found close to 365m directly downstream from the spillway. Recalling that the point of view is from an observer travelling in the streamwise direction, the outcropping appears to promote the concentration of powerhouse discharge towards the left bank with high velocities observed on the right side of the outcropping only during spill flows. Figures 2.15 through 2.17 show that away from the spillway face the flow pattern in the tailrace does not appear to be highly affected by the operational conditions, and thus, an analysis of the frequency of configuration is not deemed necessary. The maximum distance of the tailrace shown in figures 2.15 and 2.16 is roughly 760m.

In the bathymetry shown in figure 2.17, it can be seen that deeper sections of the river bed are concentrated along the left bank downstream from the powerhouse, with a transition towards a more uniform depth occurring about 600m downstream from the dam. Once more, the reference bathymetry elevation is taken to be sea level. In comparison to the Wanapum tailrace, the thalweg in this stretch of the river is not well defined. There is a region located approximately 550m downstream from the powerhouse near to the left bank where consistently fast velocities, around the 3m/s range, appear to be present. The beginning of this reach coincides with the narrowing of

the river and the location of the shallow outcropping. Keeping in mind the proportionality of power to the cube of the velocity, this area was chosen due to the high power density expected. The data plane used to describe the siting region of interest is marked on the bathymetry image with a black line and is located approximately 550m downstream of the dam. Figure 2.18 shows the data plane with velocity contours and the bathymetry for the simulation of the representative median discharge; the area considered for turbine siting is highlighted.

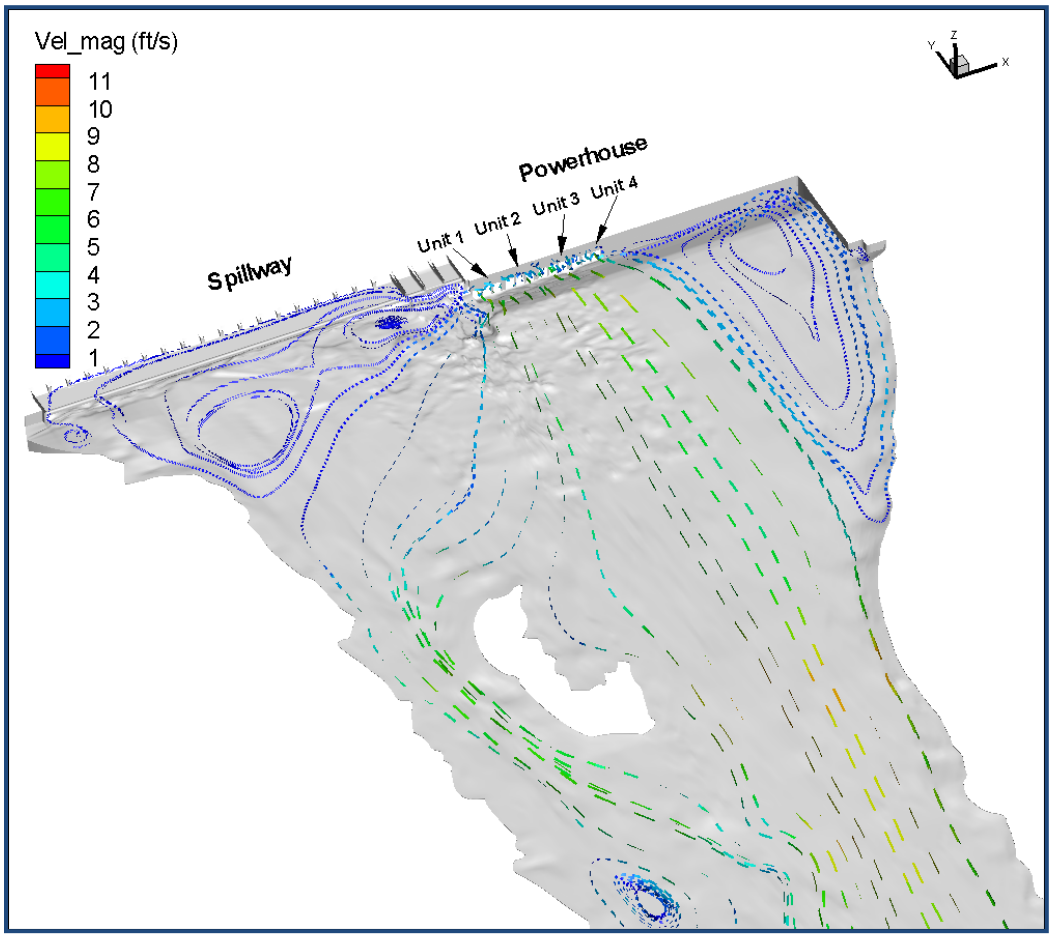

Figure 2.15 Priest Rapids Dam tailrace; contoured streamlines of the flow for a simulation of 1.82kcms being discharged through the powerhouse. *Image courtesy of IIHR*

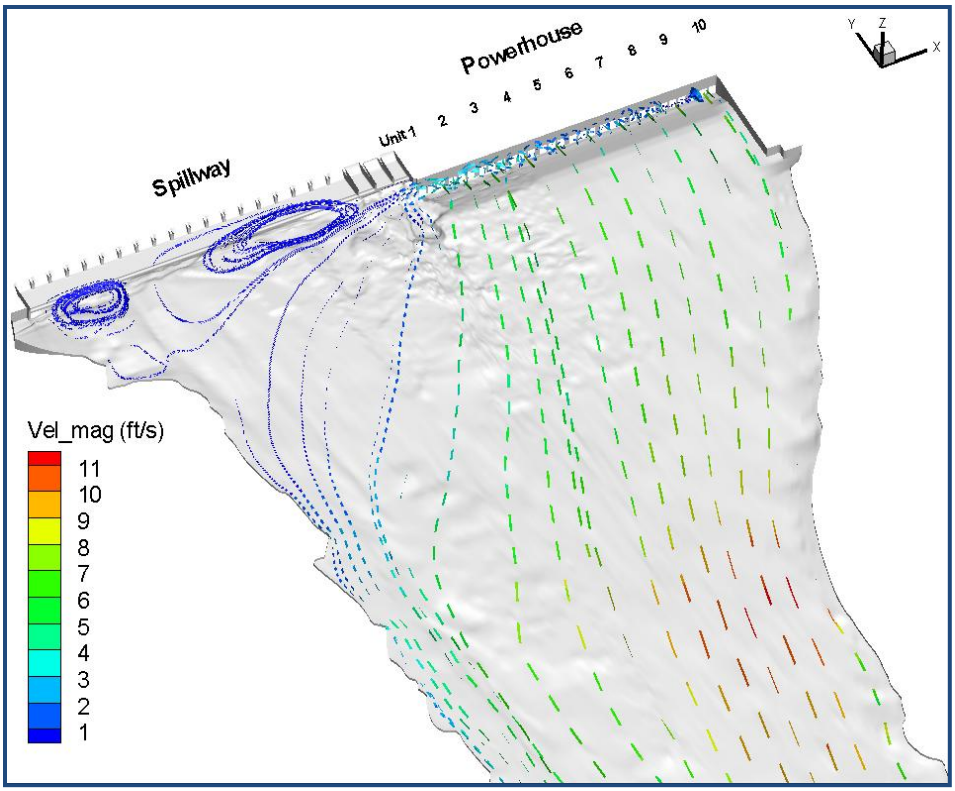

Figure 2.16 Priest Rapids Dam tailrace; contoured streamlines for a flow rate of 3.91kcms going through the powerhouse. *Image courtesy of IIHR*

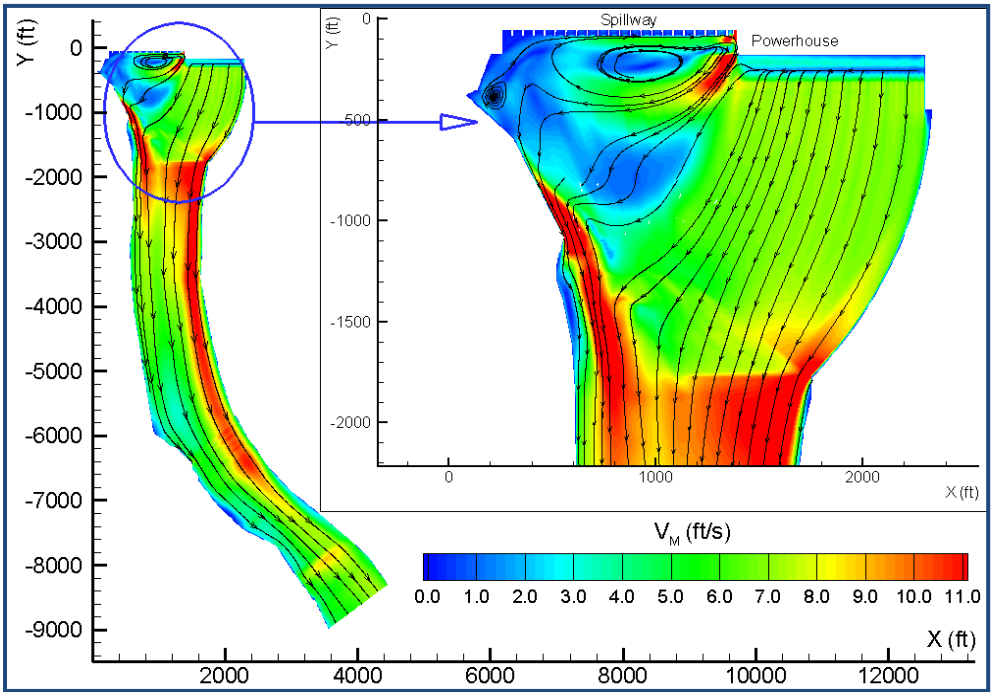

Figure 2.17 Priest Rapids Dam tailrace; velocity contours and streamlines for a configuration of 0.425kcms flowing through the spillway chute 22 and 4.67kcms going through the ten powerhouse units. The length captured in the close-up from the powerhouse is 610m. *Image courtesy of IIHR*

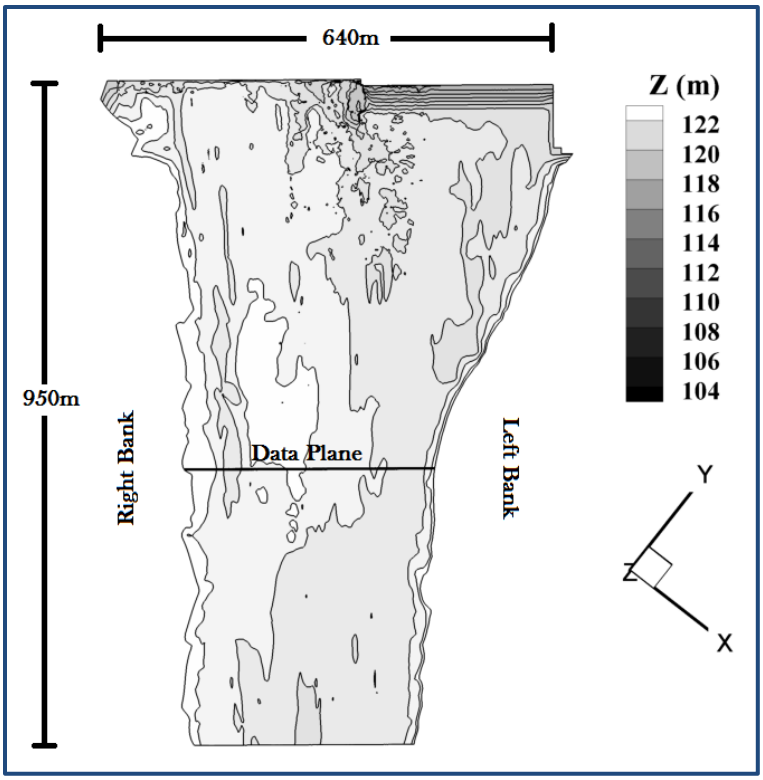

Figure 2.18 Top-down view of the bathymetry data provided for the Priest Rapids tailrace. There is a prominent rocky outcropping that extends for ~200m along the right bank. The greater depths are found along the left bank. The location of the data plane used to study the region of interest is marked with the black line.

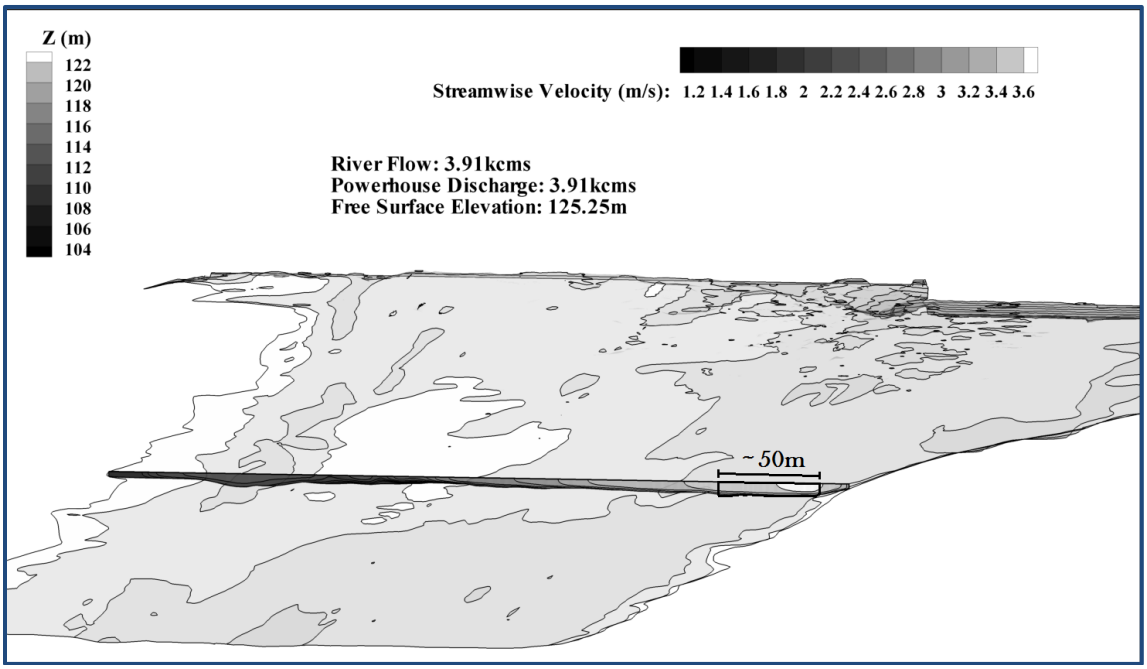

Figure 2.19 Streamwise velocity distribution 550m downstream from the Priest Rapids powerhouse. The simulation is for a ~50% exceedance probability discharge. The siting region of interest is highlighted.

In the same manner as with the Wanapum downstream site, velocity profiles are extracted from the CFD simulations along the chosen area of interest. Figure 2.20 shows the distribution of the maximum velocity, the specific discharge, and the depth for the three simulations chosen to quantify the characteristic flow rates, with the datum taken at the point farthest from the left bank. In the case of the results obtained for the Priest Rapids tailrace, the simulation taken to represent a median discharge is actually closer to the 30% exceedance discharge as can be seen in the annual total river discharge exceedance probability presented in figure 2.6. Table 2.2 lists the main parameters associated with the chosen site for the three simulation results. The parameters are calculated in a similar way as described for the site in the Wanapum tailrace. For these simulations, the river bed elevation of the data planes match with the bathymetry available and the wetted perimeter and hydraulic diameter are calculated based on the data as extracted.

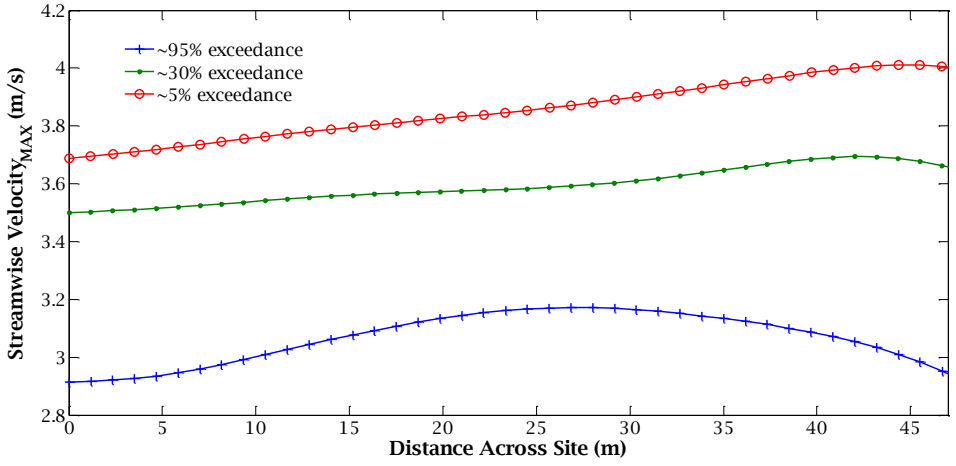

a)

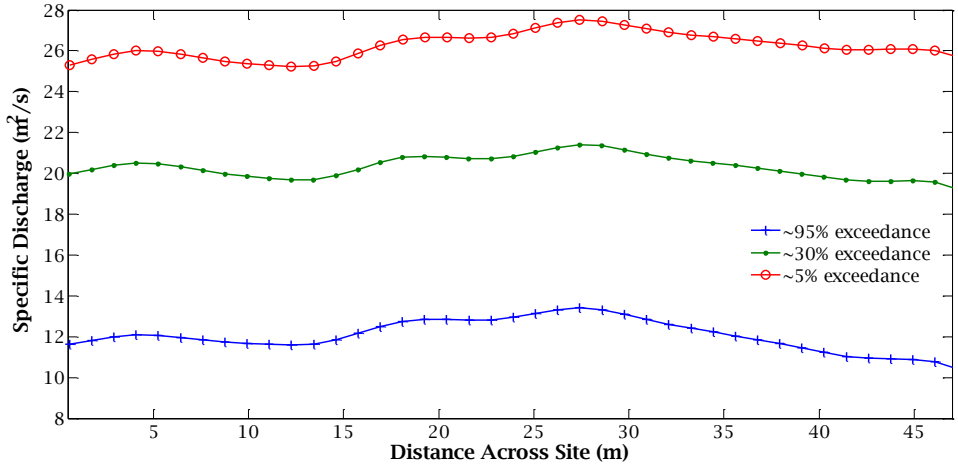

b)

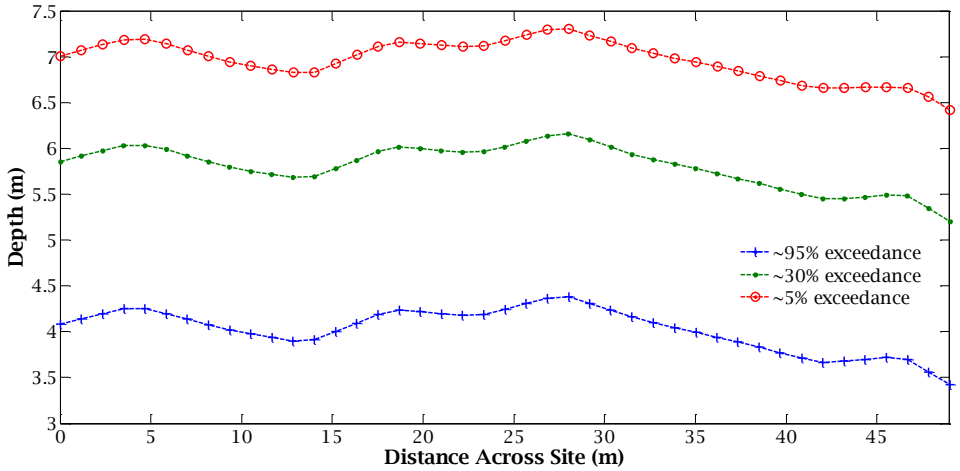

c)

Figure 2.20 Distribution of a) maximum streamwise velocity, b) specific discharge, and c) depth, across the downstream site in the Priest Rapids tailrace. Plots show results for the three river discharge simulations used to characterize the variations of parameters as a function of discharge.

Table 2.2 Averaged and Integrated Parameters for the Downstream Site at Priest Rapids Dam for the Three Characteristic Flows

Total River Q (kcms)	1.82	3.91	5.72
$\sum_n Q_n$ (kcms)	0.60	0.99	1.29
P (kW)	2,724	6,201	9,254
A_c (m^2)	201.56	284.84	341.74
V (m/s)	2.98	3.49	3.76
T_w (m)	49.00	49.00	49.00
d_h (m)	4.02	5.81	6.97
Fr	0.47	0.46	0.45
P_w (m)	57.62	60.13	62.50
D_h (m)	13.99	18.95	21.87
Re	3.30 x 10^7	5.24 x 10^7	6.53 x 10^7

2.4 Powerhouse Vicinity

The vicinity of both powerhouses is also possible for in-stream turbine siting. This has been the practice of Hydro Green LLC in 2090-10, and the Electric Kite Corporation about 8-10 years ago.

Since it is of operational interest to run the hydro turbines in the powerhouse at their highest efficiencies, the range of discharge going through each turbine and out the draft tube is regulated. The controlled discharge can provide flow velocities in the near powerhouse vicinity that do not depend on the total river discharge but instead follow on the flow rate going through each individual turbine. Greater depths are also found near the powerhouse for both dams. This favorable combination of essentially constant velocity and large depth make the powerhouse vicinity a site of interest. Figure 2.21 shows two images of the velocity contours and vectors expected near the powerhouses according to the simulations. Figure 2.21a shows a cross-section running parallel to the powerhouse, located 33m downstream, and figure 2.21b shows a transect running perpendicular to the Wanapum powerhouse and aligned with unit 6. The simulation corresponds to that when the spillway is discharging 2.11kcms and the total river flow is 5.79kcms. The discharge through the powerhouse is taken to be 3.68kcms, which corresponds to an average of 0.460kcms going through each of the eight units seen operating. The variation in the peak velocity for each jet is attributed to different discharges being simulated through the units in order to match operational conditions observed in the field [42]. The numbering of the units goes from north to south for the Wanapum powerhouse, with unit 1 being the one furthest north and unit 10 being the one next to the fish bypass. The numbering at Priest Rapids goes from west to east, with unit 1 being nearest to the spillway and unit 10 next to the left bank.

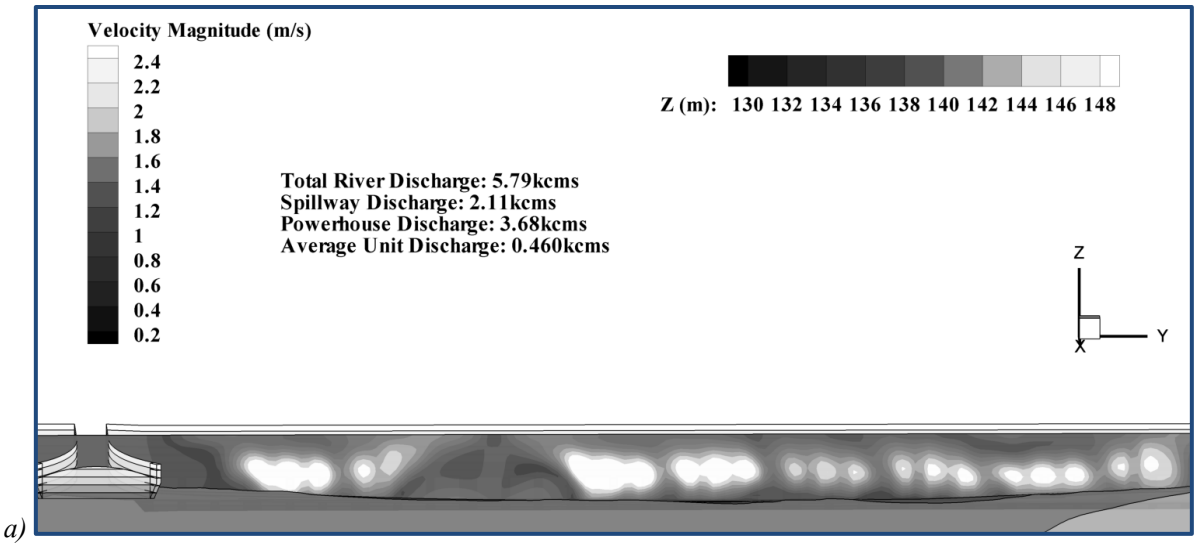

a)

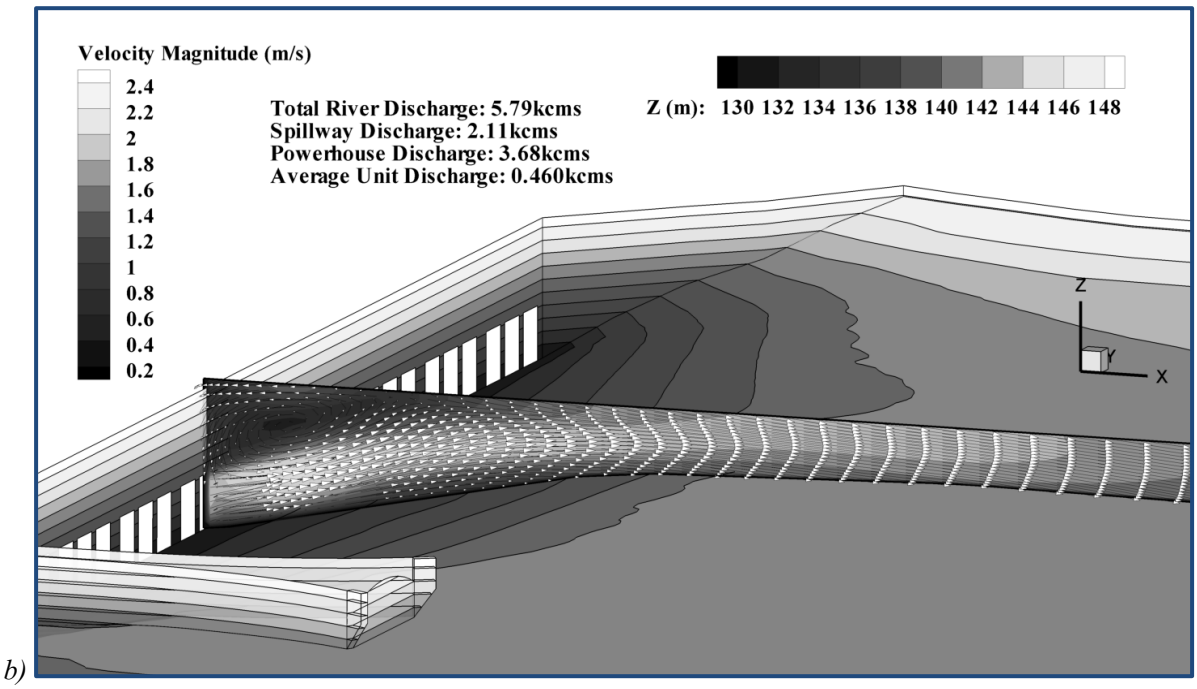

b)

Figure 2.21 Simulation data planes in the vicinity of the Wanapum powerhouse contoured with the velocity magnitude for a) a cross-section parallel to the powerhouse located 33m downstream, and b) a transect running ~150m in the streamwise direction from the powerhouse with velocity magnitude vectors included.

In analyzing conventional hydroelectric facilities, the power generated by the powerhouse (P_{gen}) can be expressed as:

$$P_{gen} = \eta_{gross} \rho g H_{gross} Q \qquad (2.7)$$

where Q is the total discharge going through the powerhouse, H_{gross} is the gross head measured as the difference between the surface elevation of the forebay and the free-surface of the tailwaters, and η_{gross} is the gross efficiency that accounts for head losses experience in the duct work, and turbine and generator efficiencies. By assuming that the gross head and the gross efficiency are constant for all of the units operating at a given instant, the total power becomes directly proportional to the discharge. Through this proportionality, the portion of the power generated by each unit can be converted into the corresponding percentage of the flow going through the unit.

For three out of five simulation results provided near the powerhouses of both dams for which the number of units being simulated and the total powerhouse discharge is known, it is found that the peak velocity at the upstream boundary of the simulation can be closely approximated by an area-average velocity calculated using the cross-sectional area of the Wanapum draft tube outlets and an average unit discharge determined by dividing the total flow through the powerhouse by the number of units operating. The three data planes correspond to the results from the Priest Rapids tailrace. The number of units operating in the low discharge (1.82kcms) simulation is four, while all ten are operating for the other two results (3.91kcms and 5.72kcms). In the case of the high discharge, 5.08kcms are flowing through the powerhouse. Accordingly, the average unit discharge is 0.453kcms, 0.391kcms, and 0.508kcms. Using the cross-sectional area of the Wanapum draft tube outlet (170.49m^2), the area-average velocities are calculate to be 2.66m/s, 2.29m/s, and 2.98m/s, for the respective simulations. In comparison, the peak velocity found in the extracted velocity data points along the upstream boundary of the simulation is 2.64m/s, 2.28m/s, and 3.00m/s, respectively. An average of the absolute relative error of these three values is 0.62%, showing a very good approximation for the peak velocity. For this initial assessment and with such a close estimate found for the three Priest Rapids cases, the outlet velocity at each draft tube for both dams is calculated using the daily average discharge through each powerhouse and the cross-sectional area of the Wanapum draft tube outlets.

Dimensions for the original draft tubes used in the Wanapum powerhouse are based on the hydraulic model built during the fish diversion development of the dam [40] and on parameters provided by Grant County PUD [50]. Grant County PUD also included information pertaining to the Priest Rapids' draft tubes and the new draft tubes being installed in the Wanapum powerhouse as part of an ongoing replacement of the original Kaplan turbines that began in 2005. Table 2.3 provides the dimensions of the draft tubes obtained from Grant County PUD. The approximate locations of the areas given are marked a, b, c, and d, in figure 2.22, which provides the layout of a draft tube and Kaplan turbine at the Wanapum Dam and can be taken to exemplify the layout found at Priest Rapids. The figure is adapted from images found in a fish study done by the Pacific Northwest National Laboratory (PNNL) on the new turbines [51]. It is noted that the actual cross-sectional areas for the draft tube outlets at the two dams is likely not the same. The draft tubes in the Priest Rapids powerhouse are smaller but there is insufficient information to determine the final expansion of the diffuser. Using the expansion ratio for the original rectangular diffuser at the Wanapum powerhouse gives a total cross-sectional area of 116.21m^2 for the three bays at the outlet of a Priest Rapid draft tube, in comparison to 170.49m^2 for Wanapum. This decrease in cross-sectional area results in an increase of the average velocity expected at the outlet. As shown above however, the magnitude of the velocities extracted from the CFD simulations for Priest Rapids Dam have better agreement with outlet average velocities calculated using the Wanapum draft tube outlet area. It is restated that for this initial assessment, the mean velocity (V) at the draft tube outlet for both dams is calculated using the outlet area of the Wanapum draft tubes.

Typically, operation of the powerhouse units is dependent on energy demand. However, during fish outmigration the turbines are ran in 'fish mode', with a limited discharge range that has been determined to provide the safest passage. As a way to further decrease the impact of fish passage through the powerhouse, when all of the units are not needed, turbines are operated in groups since it has been shown to decrease predation rates [49]. For this analysis it is assumed that the discharge

through the turbines is independent of the total river discharge and the computed velocities for a three year span are used to determine the velocity frequency distribution for each unit. For the Wanapum powerhouse, the time for which units 3, 6, 9, and 10 were off as a result of the turbine upgrade is accounted for. Figure 2.23 shows the relative frequency distribution for V for each unit of both powerhouses.

Table 2.3 Dimensions of Draft Tubes Found at the Wanapum and Priest Rapids Powerhouses

Draft Tube	**Wanapum 'Original'**	**Wanapum 'New'**	**Priest Rapids**
Last Circular Section Downstream of the Runner (m^2)	52.12	52.12	45.71
Midway Thru the Elbow (m^2)	91.04	81.20	67.63
1st Section Downstream of Pier Noses (m^2)	103.59	103.59	70.61
Combined Bay Outlet Area [24] (m^2)	170.49	N/A	N/A

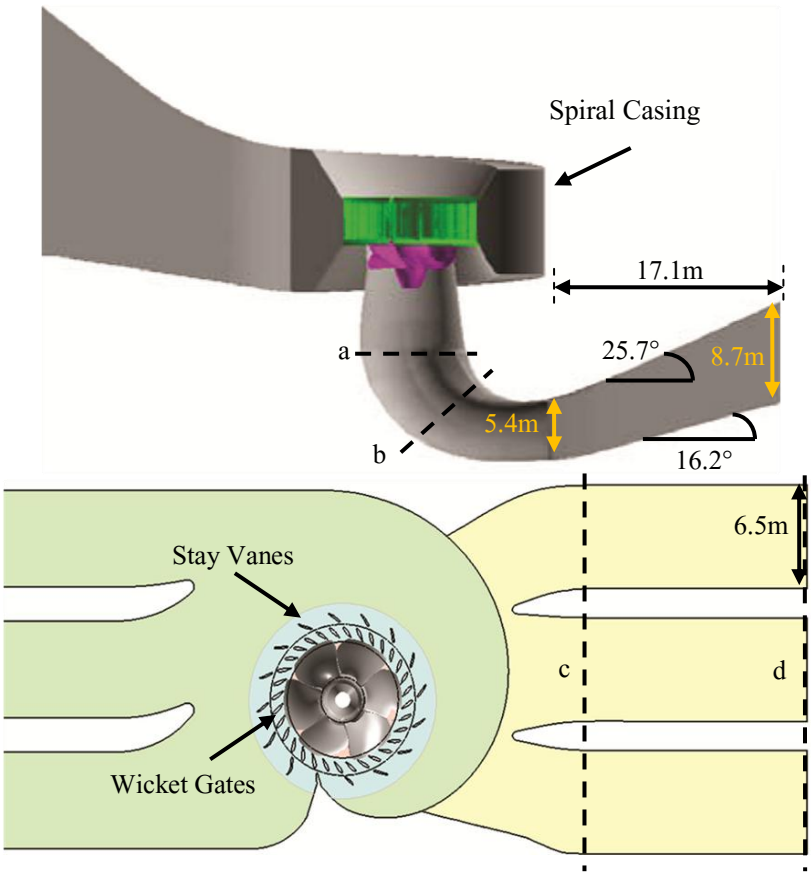

Figure 2.22 Layout of a Kaplan turbine and draft tube in the Wanapum powerhouse.
Adapted images from Dauble et al. [51]

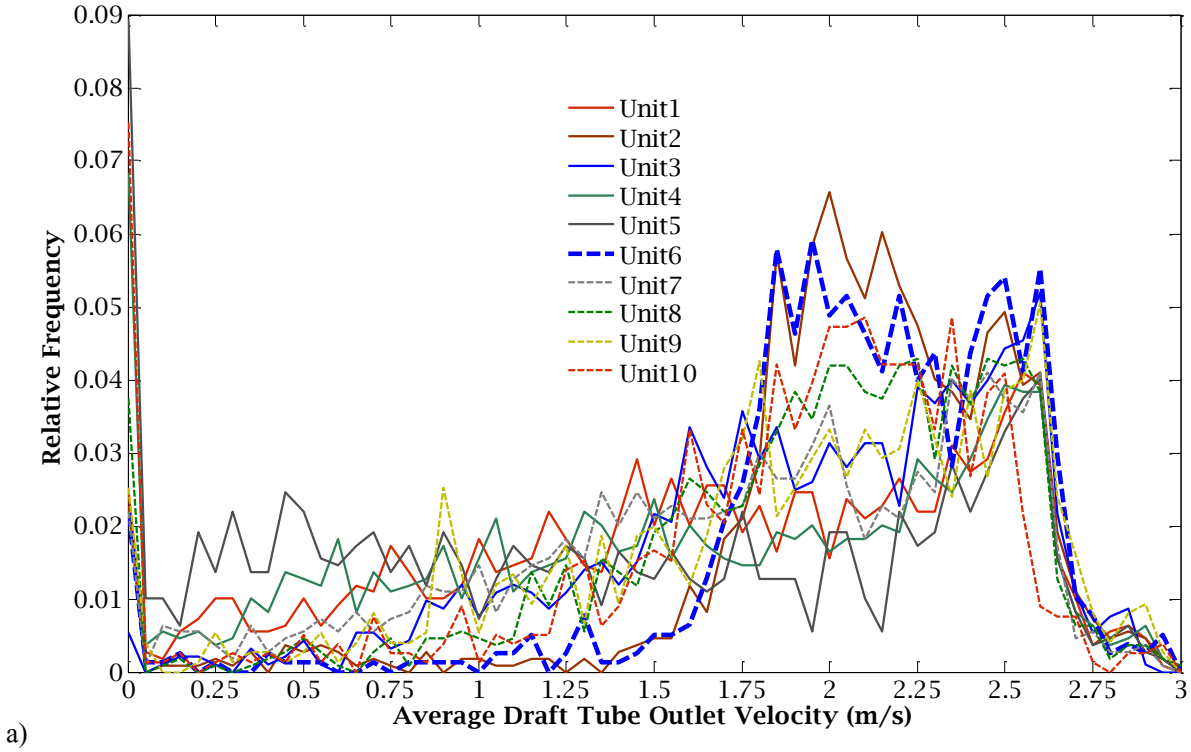

a)

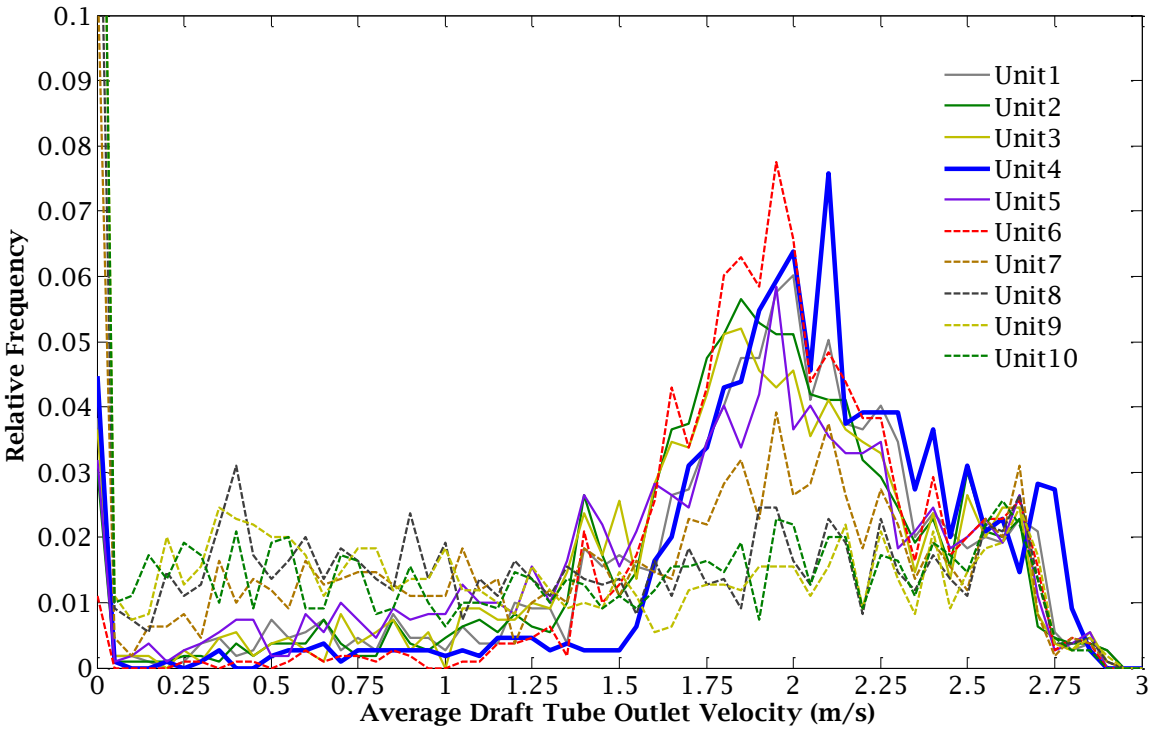

b)

Figure 2.23 Relative frequency of the area-averaged draft tube outlet velocity at a) the Wanapum powerhouse and b) the Priest Rapids powerhouse.

Unit 6 at the Wanapum powerhouse and Unit 4 at the Priest Rapids powerhouse are found to have the highest relative frequency for the highest velocities. The velocities calculated at the outlet of these units and their frequency distributions are used in determining the kinetic power associated with the flow in the powerhouses' vicinity. The tabulated results for the velocity distributions of the various units can be found in Appendix A.

2.5 Sediment Transport and River Bed Motion

As witnessed during a field visit in the spring of 2010, fine sediment is present at the shore of the forebay of Wanapum Dam but alluvial overburden consisting of large cobble stones is found on the tailrace side of the dam. Similarly, large cobble stones were observed in the tailrace of Priest Rapids Dam, as well as exposed bed rock. Figure 2.24 shows photographs taken of the tailraces, where the cobble stones are visible.

A well reported problem associated with dams is the fact that the structure acts as a barrier to natural sediment transport that occurs in rivers. This accumulation, or aggradation, of sediment in the forebay of dams has been sufficient to consume the reservoir capacity of a facility in short periods of time and has led to the decommissioning of some dams. However, sediment transport in the tailraces of the Wanapum and Priest Rapids dams is not considered to be a pertinent issue of concern.

The motion of a river bed is dependent on the composition of the latter and the force associated with the friction between the flow and the grains [11]. If river beds or banks are unstable, the bathymetry of a river reach can change with seasonal frequencies or over prolonged periods of time. In physical and numerical simulations of the Wanapum tailrace the river bed has been considered fixed [12,40,42], pointing to a stability of the river bed and indicating that the path of the thalweg and presence of smaller channels and banks can be taken to remain unchanged. The similar strata composition of the region, consisting of volcanic rock from the Columbia River

Basalt Group, and the similar presence of large cobble stone in the shore, are assumed to point towards comparable river bed stability of the Priest Rapids tailrace.

a)

b)

Figure 2.24 Images taken from the shore of the tailrace of a) the Wanapum Dam and b) the Priest Rapids Dam. Varying sized cobble stones are observed lining the banks. A 'rib' of exposed bed rock is seen in the bank of the Priest Rapids tailrace extending from near the center of the image to the right side of the picture.

III - Resource Assessment

Having established the regions of interest for in-stream turbine siting, the next step in properly identifying the available resource is to examine in more detail the vertical profiles of the streamwise velocity at the sites. The importance of understanding the velocity profiles spans from the boundary layer near the river bed to the location in the water column where the highest velocities are found. Before presenting the discussion on the velocity profiles for the downstream sites (section 3.2) and the analysis of the powerhouse vicinity (sections 3.3 and 3.4), a general review on open channel turbulent velocity profiles is given in section 3.1.

3.1 Open Channel Turbulent Velocity Profiles

At high Reynolds numbers, such as those found in the tailraces, the flow is fully turbulent. It is well understood that turbulent flows are extremely complex, and even with the current techniques and knowledge, prediction of the turbulent flow details at the various scales that exist is close to impossible. Fully turbulent flows are characterized by having large chaotic fluctuations in the form of eddies that are spinning, stretching and dividing. These random perturbations can enhance mixing and energy transfer from the large scale eddies down to smaller scales and so on until the energy reaches the smallest perturbations and becomes dissipated by the viscosity of the fluid.

Modeling turbulent open channel flows through non-uniform cross-sectional areas is not considered a trivial task. This type of flow is expected to be highly three dimensional and the distribution of the velocity is dependent on a number of factors, such as: 1) the friction force exerted on the flow by the river bed, 2) the river bed roughness, 3) the transfer of momentum as a result of turbulent fluctuations, 4) the development of velocities perpendicular to the streamwise velocity referred to as secondary currents, and 5) the existence of pressure gradients that can develop if the free surface of the flow and the river bed are not uniform (non-uniform flow) [52-58]. It is then important to keep in mind that the differences between the multiple approaches used

to simulate turbulence have an effect on the prediction of the secondary currents and transfer of momentum that is occurring in the highly turbulent nature of large natural river flow [55].

In order to quantify a turbulent flow, a Reynolds decomposition of the instantaneous velocity (u) is commonly considered [11,13,59]. When doing so, the instantaneous velocity is considered along the different coordinates and taken as a combination of two different components, the time averaged component, $\bar{u}$ (m/s), and the fluctuating component, $\acute{u}$ (m/s),

$$u_i = \bar{u}_i + \acute{u}_i \; ; \; i = 1{:}3 \qquad (3.1)$$

where i denotes the three Cartesian coordinate. Decomposition is also considered for the pressure (p (N/m^2)) distribution in a flow.

If the time averaged component is determined from a series of instantaneous data collected over a significantly long period of time, the time averaged velocity will become independent of time and considered to be a steady-state velocity. The numerical simulations provided by IIHR consist of these time averaged, steady-state values. The time averaged velocity ($\bar{u}$) is also referred to plainly as velocity (u) in this report. Through similar time-averaging, the velocity fluctuations have an average value equal to zero if averaged over a significant period of time.

By introducing the above decomposition of the flow variables into the conservation equations for mass and momentum, it can be shown that all three components of the velocity satisfy the necessary conservation of mass and that an extra term appears in the momentum equation, which acts as an addition of stress to the flow. The extra term,

$$-\rho\overline{\acute{u}_i\acute{u}_j} \; ; \;\; i,j = 1{:}3 \qquad (3.2)$$

where ρ (kg/m^3) is the density, appears due the flux of momentum induced by the fluctuations as fluid particles are transferred from faster moving regions to slower regions and vice-versa. These fluctuations drive water particles into different velocity layers and can be seen as a mechanism that acts similarly to the viscosity of the fluid. Since the particles are much larger than the molecular

scale at which the viscosity of the fluid acts, when present, the effects of turbulent fluctuations supersede those of the viscosity of the fluid. The nine components that result from an expansion of the extra term are representative of a stress tensor, with the diagonal terms representing normal stresses and the symmetric off-diagonals corresponding to shear stresses. These terms are known as Reynolds stresses and must be considered for turbulent flows in addition to the viscous stresses. Although the time average of the fluctuations is zero, the time average of the mixed products of velocity fluctuations is generally non-zero.

When a decomposition and time-averaging of the velocity and pressure parameters are employed in solving the conservation laws, an additional model is necessary in order to provide the information that allows closure to the problem, in particular the relation between production and dissipation of the turbulent kinetic energy. A number of models have been suggested by researchers over the years and a review of each goes beyond this work. From the available literature sources [11,42], it is found that the general closure scheme used in the corresponding numerical modeling is the k-ε model, where k represents the production of turbulence and ε the dissipation of it. By solving for these values through equations that describe the transport of k and ε with the flow, an equivalent to the kinematic viscosity of the water is suggested, commonly referred to as the 'eddy' viscosity (ν_t), which is proportional to k^2/ε. By solving for the eddy viscosity it can then be incorporated into the conservation laws in order to account for the effects that the turbulent fluctuations have on the flow.

In these open channel flows, the turbulent water is bounded on all sides except at the free surface. It is generally understood that if the river bed is considered stable and stationary, then the velocity at the river bed is equal to zero, satisfying the no-slip condition. In a very small region that next to the no-slip boundary, referred to as the viscous sublayer, velocity fluctuations and their effects are dissipated and only the viscosity of the water acts in generating a shear force on the river bed. This shear force exerted onto the river bed is equally and oppositely exerted on the flow and constitutes

a friction force resisting the flow. This force primarily arises as a balance to the driving gravitational force. As one moves away from the bed, the high shear rate between the stationary wall (i.e. river bed) and the moving flow leads to turbulent outbursts. The Reynolds stresses associated with these outbursts become predominant over the stresses associated with viscosity and account for the large majority of the shear stress acting on the fluid as these fluctuations move through the water column [11,13,59].

von Kármán demonstrated through dimensional analysis the existence of a velocity scale representative of the turbulent shearing stress that results from the wall-flow interaction [59]. This velocity parameter is known as the *shear* or *friction velocity* and is defined as,

$$u_* = \sqrt{\tau_0/\rho} \qquad (3.3)$$

where τ_0(N/m^2) is the shear force per unit area exerted on the river bed. This parameter provides a scale for the turbulent eddies and transfer of momentum occurring due to the fluctuations associated with the terms introduced in equation 3.2.

Through the years, by combining empirical observations and hypotheses on the scale at which turbulent fluctuations enhance mixing and particle transport, variations of logarithmic velocity distribution profiles and other distributions based on power laws have been formulated [56-63]. The finer details governing the effects of turbulence continue to be a source of dispute among researchers due to the complexity and the different assumptions and theories employed in formulating the equations found.

In general, the height above the river bed where viscous effects lose importance is very difficult to determine exactly due to its small size. Defining a dimensionless height as,

$$z^+ = \frac{zu_*}{\nu} \qquad (3.4)$$

where z (m) is the height above the bed, u_* (m/s) is the shear velocity, and ν (m^2/s) is the kinematic viscosity of the fluid, this viscous sublayer typically is found to have a maximum height corresponding to $z^+ \cong 5$ [11,13]. For flows along rough surfaces, the size of the roughness elements has been found to impact the shape of a velocity profile more than the effects of viscosity. If the roughness size is larger than the viscous sublayer, experiments have shown that the drag exerted on the bed is dominated by the cumulative shape drag of the roughness elements and not by the viscous effect. Abrupt changes in the bathymetry which can correspond to bends, banks, ripples, etc, have been reported as causing unrealistic sizes for the surface roughness parameter when attempting to run regression fits on equations that use the surface roughness length scale; this is believed to occur because of excess drag induced by the intricacy of the bathymetry [12,57].

For ~ $5 < z^+$ there exists a buffer layer, or transition region, where both viscous and turbulent stresses play a role [13]. Depending on the friction Re number of the flow, defined as

$$Re_\tau = lu_*/\nu \qquad (3.5),$$

it has been reported that the extent of the buffer layer can vary from the typically considered value of $z^+ = 30$ and increase upwards of $z^+ > 200$ for $Re_\tau > 13{,}300$ [64]. In the case of open channel flow the length scale (l) is typically taken as the channel half-height, or $.5h$ (h = depth of the water column).

It is generally understood that at the height of the buffer layer the velocity profile takes on a logarithmic distribution. In a similar manner as the lower bound of this logarithmic profile, the upper bound depends on the Reynolds number [13], with upper limits reported as high as $z^+ = 6{,}000$ for $Re_\tau > 50{,}000$ [64].

For values above the logarithmic distribution, the change in velocity stops being dependent on the 'inner' variables, such as the fluid viscosity, and becomes a function of the larger scales like the total depth of the flow and the strength of the inertia characterized by the free surface velocity. This

region is known as the outer layer of the velocity profile. Equations that have been derived for velocity profiles using roughness sizes or viscosity length scales are typically valid only within a small distance above the bed and do not provide accurate fits to measured velocities in the outer regions of the profile if these deviate from the logarithmic distribution.

3.2 Downstream Sites

Following on the well documented empirical formula known as Cole's Law of the Wake and the variations that have been suggested [56,62,63], the modified log-wake law as reported by Guo and Julien [57] is used to fit the velocity data points extracted from the IIHR-provided simulations. This modified log-wake law reads as follows,

$$u = \frac{u_*}{\kappa}\left[ln\frac{z}{z_o} - \frac{1}{3}\left(\frac{z-z_o}{\delta-z_o}\right)^3\right] + \frac{2\Pi u_*}{\kappa} sin^2\frac{\pi(z-z_o)}{2(\delta-z_o)} \quad (3.6)$$

where the velocity (u) is in the streamwise direction, z (m) is the height above the river bed, δ (m) is referred to as the 'dip position' by Guo and Julien [57] and corresponds to the height of the maximum streamwise velocity point, κ is the universal von Kármán constant taken to be equal to 0.41, Π is Cole's wake strength parameter, u_* (m/s) is the shear velocity as defined in equation 3.3, and z_o (m) is the height above the bed where the no-slip condition is satisfied. The 'dip position' arises from the fact that the presence of strong secondary currents can drive the point of maximum velocity, or cause it to 'dip', below the free surface. The strength and impact of secondary currents has been found to strongly depend on the geometry of the cross-sectional areas of channels and the meandering of the channel's path [52-55].

The first bracketed term in equation 3.6 accounts for the logarithmic layer found for $z^+ > 30$ and the height at which the no-slip condition is satisfied, plus a third degree term to satisfy a zero velocity gradient at the point where the maximum velocity is reached. The second term in the equation (incorporating Π) corresponds to the empirical expression added to capture the shape of the outer region for profiles that deviate from the logarithmic distribution.

For each data plane and discharge, spatial coordinates and time averaged velocity components are considered. Focus is on planes in the siting regions of interests. As shown in the bathymetry images for both river reaches in section 2.3, the natural curvature of the river's path, and hence the direction of bulk flow movement, is generally not parallel to the 'x' or 'y' coordinates. The streamwise velocity is then calculated using both the 'x' and 'y' velocity components, while ignoring the 'z' component since it does not contribute a velocity component perpendicular to a device's working cross-sectional area.

In equation 3.6 the initial slope of the logarithmic profile near the river bed corresponds to a value of u_*/κ . As found in Sturm [11], typically values corresponding to $z/h < 0.6$ should used to determine the shear velocity but this depends on the extent of the water column where the logarithmic distribution is valid. As mentioned in section 3.1, the bounds on the logarithmic distribution have been found to depend on the friction Reynolds number (Re_τ). To determine the points to use for proper fitting of the slope, a graph of u vs. (z/h) on a semi-log plot can be used to identify the approximate reach of the logarithmic distribution. As seen in figure 3.1, the range where the logarithmic relation appears to be valid is found to hold approximately for $z/h < 0.4$.

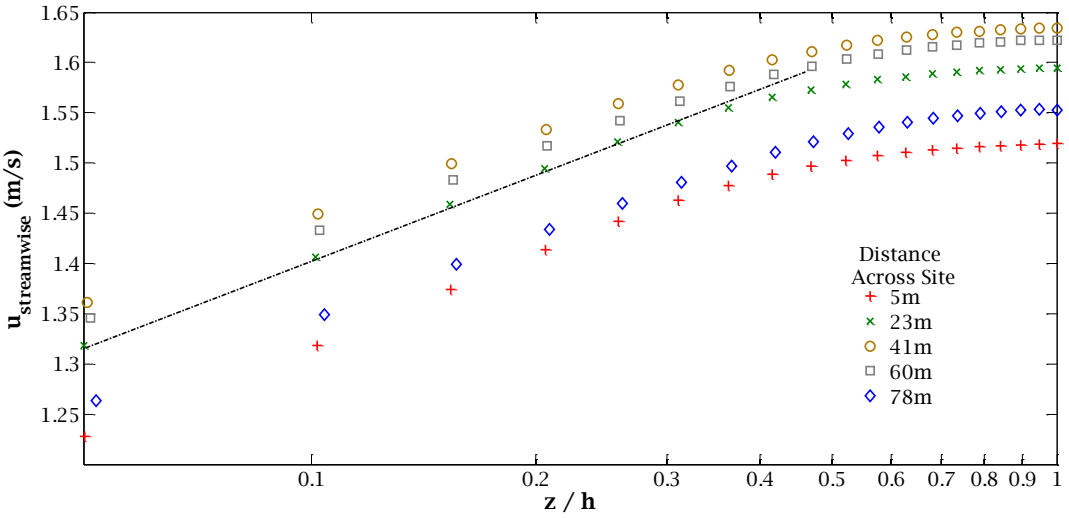

Figure 3.1 Plot of the streamwise velocity vs. the normalized depth at five different locations across the Wanapum downstream site. The normalized depth is plotted on a log scale. Data corresponds to a river discharge of 3.00kcms.

Four parameters have to be determined in order to complete equation 3.5: 1) u_*, 2) Π, 3) δ, and 4) z_o. As suggested by Guo et al. [58], a least-square curve fit is employed to determine these parameters. Close attention is paid to providing good initial guesses for each variable, as a high level of sensitivity is observed with respect to the shear velocity and the wake strength.

Using a mean of the fitted values for u_* from the different simulations and a half height determined from the hydraulic depth of the cross-sectional areas considered, Re_τ is calculated to range between 77,500 and 400,500 for the Wanapum downstream site and from 160,000 to 374,000 for the Priest Rapids site. The mean values for u_* in the simulations range between 0.02 - 0.14 m/s, and the logarithmic distribution appears to fit well for values of $z^+ > 100{,}000$, where as defined in equation 3.4, $z^+ = \frac{zu_*}{\nu}$.

From the results of the fits, z_o is found to be very close to zero in both regions of interest. Increasing in value as Re_τ increases, the order of magnitude for the fitted value of z_o is found to fall between 10^{-7} and 10^{-5} in both sites. Using the results for which the largest values of z_o were found in the fit across the sites, which also corresponds to the simulations with the largest fitted value of u_*, the mean value z^+ is 1.80 across the Priest Rapids site and 5.15 for the Wanapum site. Since these values for $z^+$are equal or less than $z^+ \cong 5$, z_o can be viewed as the height of the viscous sublayer. The values fitted for z_o demonstrate a negligible impact of river bed roughness on the location of the no-slip condition for both sites. This coincides with that stated by Politano et al. [42] for the Wanapum tailrace, where it has been found that there is very little effect of the surface roughness on the flow field. Sinha et al. [12] similarly determined in the early simulation of the Wanapum tailrace that the reach of river from the left embankment down pass the constriction can be considered as being hydraulically smooth and any surface perturbations are smaller than the viscous sublayer. Further discussion on the parameters can be found in Appendix B.

3.2.1 Wanapum Site

In figure 3.2 the distribution of the fitted values of u_* for the velocity profiles across the Wanapum downstream site during powerhouse-only operation is plotted alongside the bed elevation. The river discharge is medium (3.00kcms). The plot is accompanied by an image of the whole data plane spanning across the river contoured with the streamwise velocity. The shape of the cross-section is seen to resemble the shape of a compound channel, with a trapezoidal shape along the main channel encompassing the thalweg and a rectangle-like shallow plain extending towards the right bank. The region studied for siting falls inside the trapezoidal main channel and is demarked by the two vertical black lines.

Studies on compound open-channel flows are numerous [52-54,66-69]. It has been well established that the flow in the shallow plains can have a large effect on the flow in the main part of the channel. Typically the bulk of the flow found in the main channel has a higher velocity than that of the flow in the shallow areas. This velocity difference between the two sections and the change in the geometry leads to the formation of a shear that generates turbulence and vortices that cause the transfer of momentum to occur between the flows in the sections. Results from flume experiments performed by Knight and Hamed [53] and Tominaga and Nezu [69] on symmetrical and asymmetrical cross-sections comprised of a rectangular main channel and a wide rectangular shallow plain, show how the effects of the geometry and turbulence anisotropy (direction dependence), results in secondary currents resembling helical vortices that propagate downstream with an axis parallel to the streamwise flow. The appearance of these secondary currents is found to drive the point of maximum velocity in the main channel below the free-surface. This effect is found to lessen as the depth increases and is also dependent on the width to depth ratio of the main channel, the ratio of the main channel width to the width of the cross-sectional area, and the relative depth difference between the different sections.

As reported by Knight and Demetriou [54], normally the flow in the shallow banks will slow down the flow in the main channel, corresponding to a transfer of momentum between the flows. The thickness of the shear layer and the intensity of turbulence occurring are dependent on the relative depth and width of the sections that make up the cross-sectional area of the channel and the specific geometry of each.

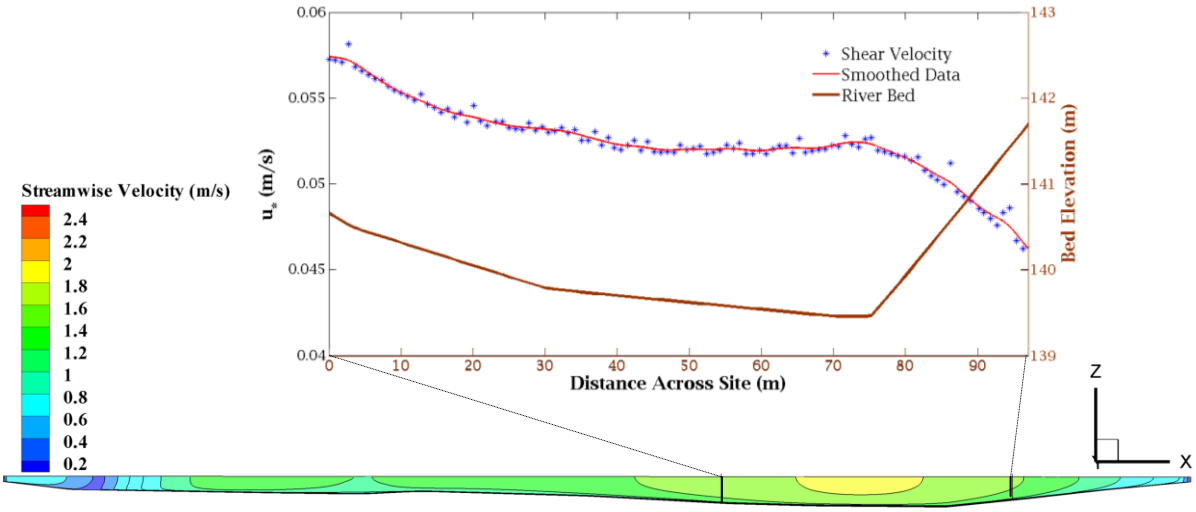

Figure 3.2 Distribution of shear velocity across the Wanapum site for a river discharge of 3.00kcms. The simulation corresponds to discharge that is only occurring through the powerhouse. The view on the data plane is looking upstream, with the wide shallow plain corresponding to the right bank of the river. The site boundary is demarked with black lines, with the datum taken at the point farthest from the left bank. The smoothed data line is intended for visualization.

The relation between the flows and their interaction is very complex even for cross-sections consisting of symmetrical trapezoidal and rectangular shapes. Nonetheless, from figure 3.2 the distribution of the velocity and shear velocity found in the deeper trapezoidal region is consistent with that found in the literature, reaching an almost constant value around the center of the region and decreasing towards the left bank as the side wall is approached. The point of maximum velocity (δ) is found at the free surface for all of the Wanapum tailrace CFD simulation results and secondary currents are not considered to be relevant. Although the k-ε model is not typically expected to capture the full strength of secondary currents because it does not account for the anisotropy of turbulence [55], the impact of these currents can be expected to be minimal in the

main channel encompassing the thalweg based on the large aspect ratio of the channel (~8) and the large relative depth (0.5) even at the low discharge (1.70kcms) [53,69]. The increase in shear velocity in the direction of the right bank is attributed to an increase in turbulent stress intensity due to a shear layer developing between the flow in the wide shallow bank to the right and the flow in the main channel.

In the shear velocity, a certain amount of random 'noise' is observed. A close look at the vertical velocity data extracted from the CFD simulations with Tecplot showed occasional discrepancies in the location of the bed elevation in comparison to the data planes. The sensitivity of the shear velocity to the location where the no-slip condition is satisfied is seen in these spikes, which are associated to interpolation errors incurred during the extraction of data. In figures 3.2 a smoothed curve is also plotted.

The distribution of the shear velocity for the cases when the fish bypass and the regular spill are operating is dominated by the operational configuration (the dependence on operational configuration of the dam was also seen in figure 2.12.); these distributions are found in Appendix B. The powerhouse-only scenario is thus viewed as a 'neutral' case, where the velocity distribution is primarily influenced by the characteristics of the natural river. Based on this, the stretch from the 45m to 65m mark is further identified as the most optimal location along the region of siting for placement of a pilot scale deployment, with a relatively constant shear stress distribution that is not influenced by the effects of the wall on the left bank nor the interaction between the flow in the main channel and the shallow plain extending towards the right bank.

In figure 3.3, the normalized height (z/δ) is plotted against the velocity defect normalized by the fitted shear velocity ($(U-u)/u_*$) for the velocity profiles from the 45m to 65m mark across the site. Based on the data, at the Wanapum site δ is equal to h and U is taken to be the streamwise velocity at the free surface. In these representative profiles, the presence of the various factors

contributing to the vertical velocity distribution does not allow a collapse of the data from all of the simulations onto a single profile. This shows that the flow as the discharge and operational configuration change is not self similar. The spatially different profiles from each simulation do, however, show a self similarity among each other through a good collapse onto a single curve.

The operation of the fish bypass corresponding to the low discharge case is seen to offer the highest variability between the profiles, showing the high impact on the flow field attributable to the operation of this hydraulic structure. The presence of the fast surface jet and the formation of the strong recirculation in front of the spillway lead to a significant increase in the velocity deficit throughout the whole water column when compared with the 'neutral' and spillway operational conditions. During the medium discharge the velocity is more uniformly distributed along the upper 20% of the water column and the velocity deficit in the lower 80% is reduced when compared to the low discharge. Using the medium discharge profile as the baseline, the high discharge simulation shows a further decrease of the velocity deficit throughout the water column that leads to a nearly uniform velocity found in over 50% of the water column. This is attributed primarily to an enhancement in the transfer momentum and mixing as the flow coming from the powerhouse and that coming from the spillway interact.

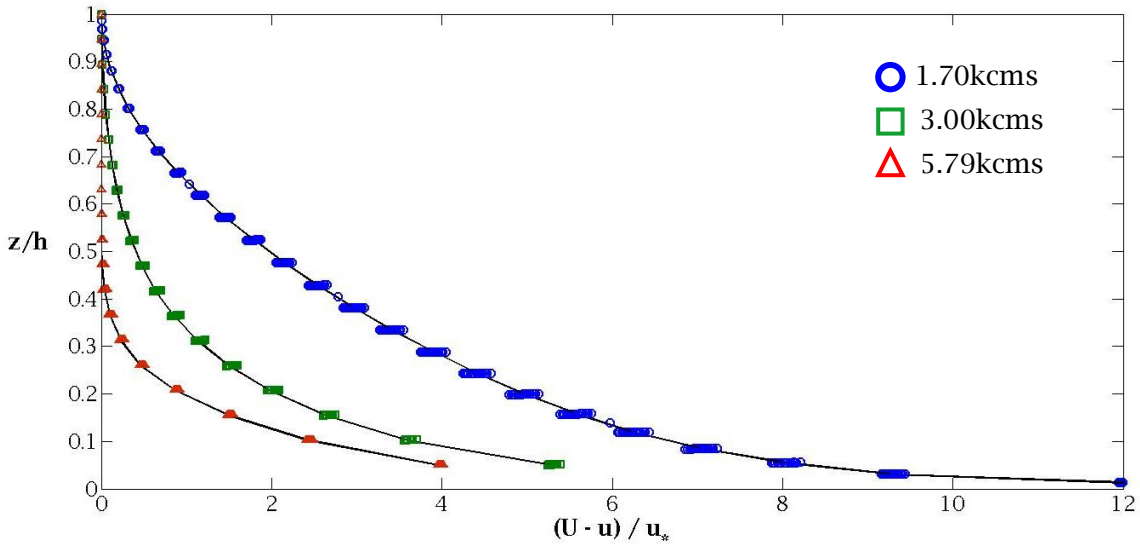

Figure 3.3 Normalized depths vs. normalized velocity deficits for the three Wanapum tailrace discharge simulations. The velocity data are from the profiles extracted between the 45m and 65m marks.

Figure 3.4 shows representative velocity profiles at the different discharges with the data and the fitted profiles plotted. Median values of the root-mean-square deviation (RMSD) and the correlation coefficient (R^2) are presented in table 3.1 for all of the fits made to the data extracted from the three characteristic discharge simulations. As expected, the increase in streamwise velocity associated with an increase in discharge is also accompanied by an increase in the shear velocity. As noted with the increase in the velocity gradient with respect to the height above the river bed ($\partial u/\partial z$) in the lower 15% of the water column, this increase in shear rate near the river bed increases the strength of the turbulent outburst. The value for the wake strength parameter was found to be positive for the low discharge/fish bypass operational simulation, whereas for the other two, the wake strength parameter was found to be negative. The positive value of Π is also attributed to the effects of operating the fish bypass; the distributions and a discussion of the wake strength parameter across the site are found in Appendix B.

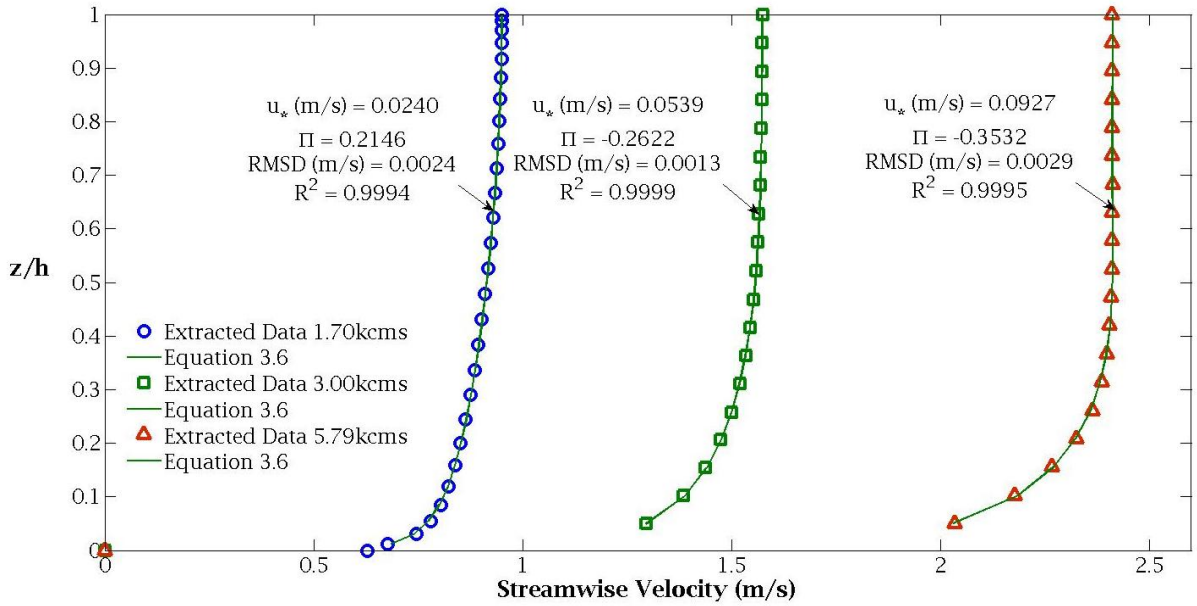

Figure 3.4 Typical velocity profiles for the downstream Wanapum site

Table 3.1 Median RMSD and R^2 Errors for All of the Fitted Velocity Profiles in the Wanapum Downstream Site

Total River Discharge (kcms)	1.70	3.00	5.79
RMSD (m/s)	0.0021	7.5750e-04	0.0031
R^2	0.9995	1	0.9995

3.2.2 Priest Rapids Site

The distribution of the shear velocity across the site downstream from Priest Rapids dam is shown in figure 3.5. A stronger dependence of the distribution on the river bed bathymetry is observed over the operational configuration. The cross-sectional area across the whole river for a medium river discharge is also shown in figure 3.5 contoured with the streamwise velocity. As a whole, the cross-section is characterized by a more jagged bed boundary than that at the Wanapum site and has two deep regions near each bank separated by a shallow plain.

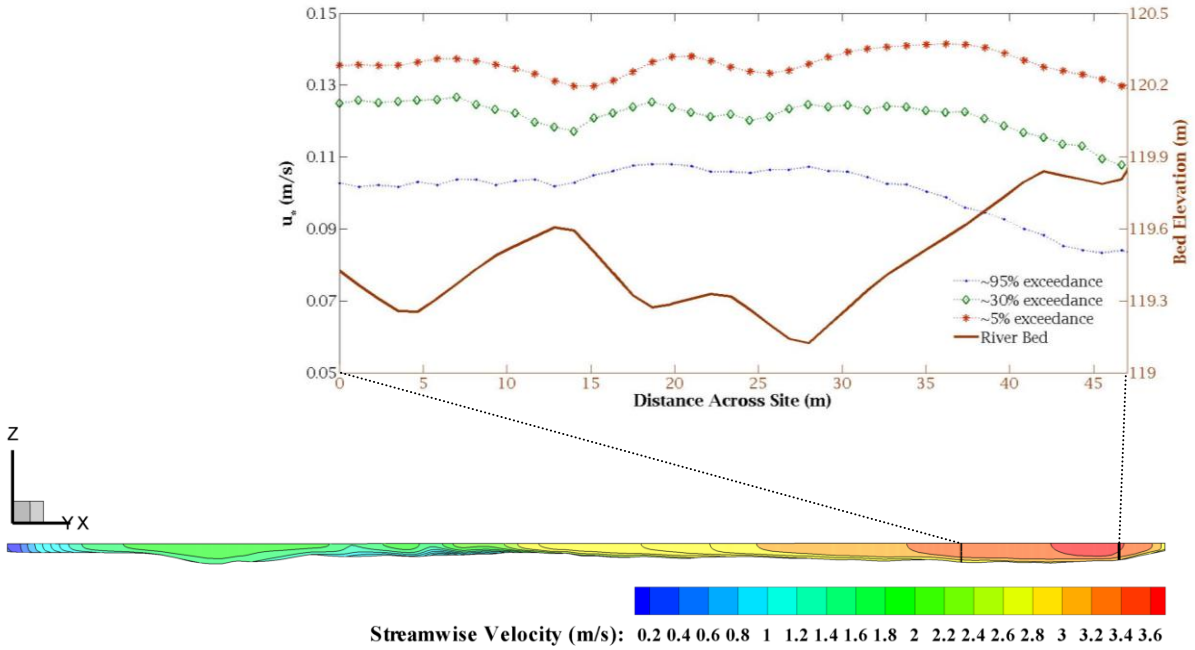

Figure 3.5 Shear velocity distributions for the three discharges across the Priest Rapids downstream site. The data plane across the whole river corresponds to the simulation of a 3.91kcms river discharge (~30% total river discharge exceedance). The view on the plane is looking upstream, with the higher velocities located closer to the left bank. The boundary of the site is demarked with black lines; the datum is taken at the farthest point from the left bank.

The shear velocity is seen to increase while maintaining a similar distribution with a rise in river discharge. However, as the discharge and depth increase there is a more pronounced difference between the shallower and deeper sections as seen with the dips around the 15m and 25m marks for the medium and high discharges. A higher shear velocity generally appears near the deeper regions, which corresponds to a larger weight contribution to the frictional shear. There is also an increase and gradual evening out of the shear velocity in the direction of the left bank occurring with an increase in discharge between about the 30m and 40m marks. However, the effect of the left bank wall is still observed, with an eventual fall off in the shear velocity at the left edge of the region. The effect of the wall has a larger impact on the siting area of interest for the low discharge case.

Considering that this general area of the Priest Rapids tailrace is shallower when compared to the main channel following the thalweg in the Wanapum tailrace, the effects of the bed bathymetry and the proximity of the free surface to the river bed are expected to have a more pronounced impact on the vertical velocity distribution [50,53]. The results point towards the likely influence of bed bathymetry on shallow turbulent flows in open channels. The distribution of Π and δ across the siting region similarly show a correlation with the shape of the river bed and are examined in Appendix B.

Unlike the Wanapum downstream site, the fitted value for δ is not found at the free surface but instead varies between 70 to 85% of the total depth. The velocity gradient ($\partial u/\partial z$) calculated from δ up to the free surface for the three simulations, in terms of a length that scales with the depth, is found to be on average 0.28%. Based on the extracted data, the velocity does in fact increase up to the free surface. With such a minimal change in the velocity in terms of the outer variables, the fitted value of δ can be taken to represent the beginning of a constant velocity region that extends up to the free surface.

The limitation presented by the lower depths found in the Priest Rapids tailrace make the deeper section found between the 15m and 35m marks the more optimal place within the region studied for siting of a stand-alone hydrokinetic turbine. The plot of z/δ versus $(U-u)/u_*$ is shown in figure 3.6 for spatially varying velocity profiles from the 15m to 35m mark. The value used for U is the streamwise velocity at the free surface of each profile considered. As opposed to the Wanapum site, the data from the three simulations are seen to collapse well around a single curve, showing a self similarity at the different discharges. Higher fluctuations away from a single curve are seen for $0.3 < z/\delta < 0.6$ and can be attributed to the sensitivity of the various factors influencing the velocity distribution and the higher variability of these factors due to the ragged bathymetry across the site.

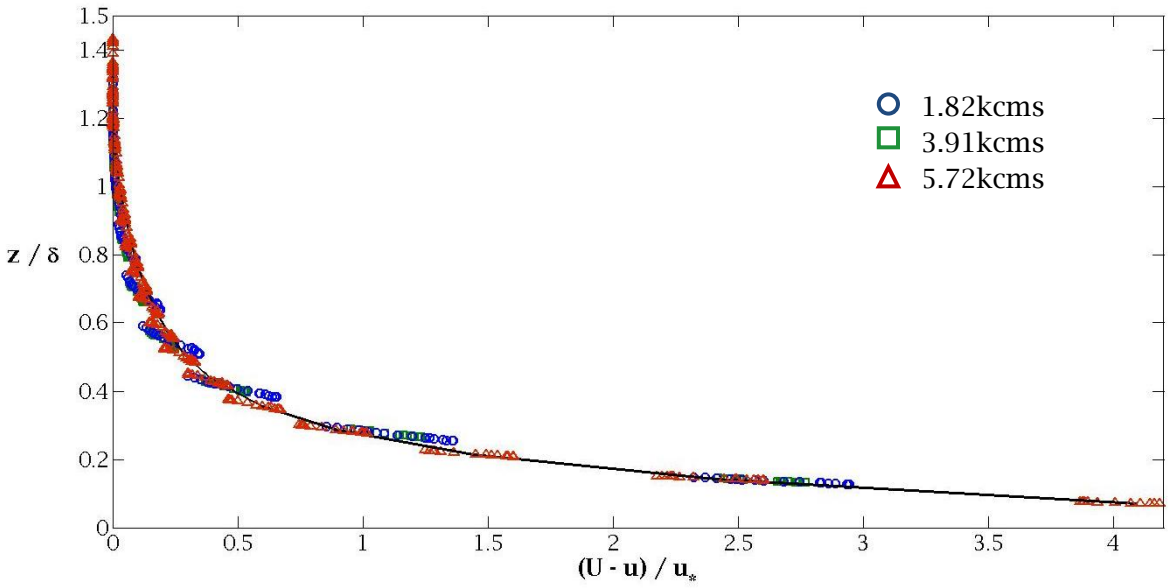

Figure 3.6 Normalized depths vs. normalized velocity deficits for the three Priest Rapids tailrace discharge simulations. The velocity data are from the profiles extracted between the 15m and 35m marks.

Figure 3.7 shows representative velocity profiles at the different discharges with the data and the fitted profiles plotted. The height has been normalized by the total depth (h). Median values of the RMSD and R^2 are presented in table 3.2 for all of the fits made to the data extracted from the three discharge simulations.

Comparing with the shear velocity found for the Wanapum downstream site, it can be seen how the increase in the velocity gradient near the river bed continues to be associated with an increase in the shear velocity. For this site, the significantly higher velocities cause for much stronger shear velocities; for the profile representative of the low discharge, the shear velocity is close to 15% greater than that of the high discharge profile in the Wanapum case. However, the change in the shear velocity between the low and high discharge profiles in this case is not as large, varying by only 30%, whereas for the Wanapum profiles, the change between the low and high discharges is close to 290%. This lower range in shear velocity can be taken to represent the smaller impact expected on the flow field from operational configurations in comparison to the Wanapum tailrace. At the high discharge, the results obtained through using equation 3.6 deviate from the data, slightly overshooting the velocity profile between $0.3 < z/h < 0.5$ and slightly under predicting it for $0.5 < z/h < 1.0$. The RMS deviation for the high discharge profile fit is small, with a median value of only 0.19% across the site and is considered negligible. The distribution and discussion of the other fit parameters are found in Appendix B.

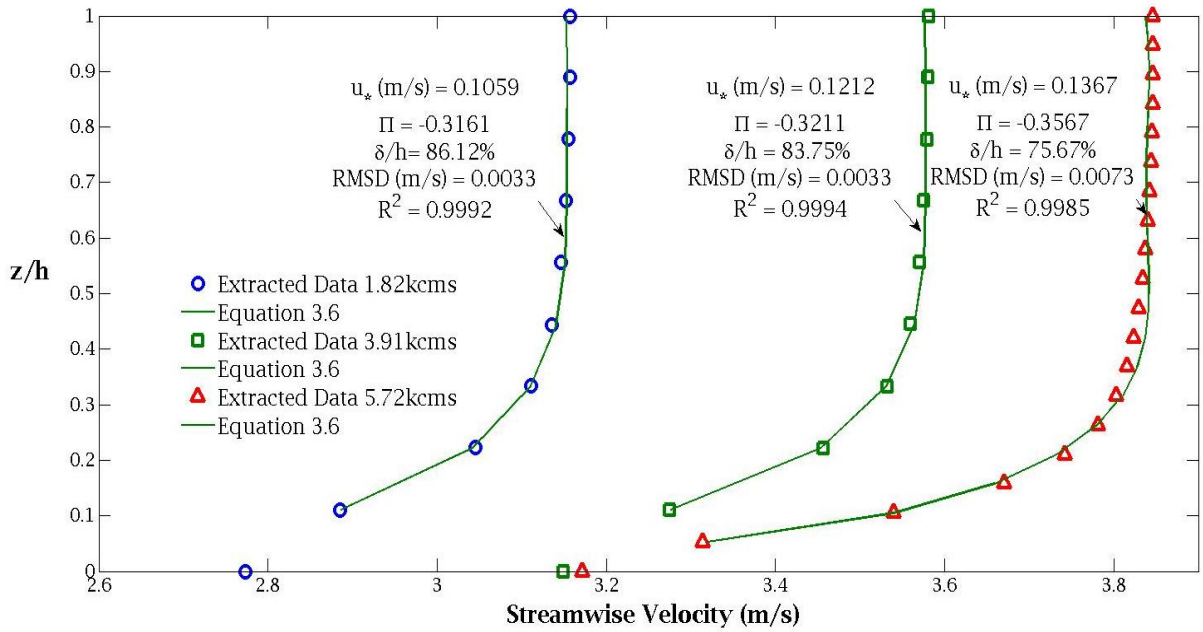

Figure 3.7 Typical velocity profiles for the downstream Priest Rapids site

Table 3.2 Median RMSD and R^2 Errors for All of the Fitted Velocity Profiles in the Priest Rapids Downstream Site

Total River Discharge (kcms)	1.82	3.91	5.72
RMSD (m/s)	0.0036	0.0031	0.0072
R^2	0.9992	0.9995	0.9986

3.3 Powerhouse Vicinity

As water is drawn from the dam's forebay through the penstock and Kaplan turbine, and then released through the draft tube into the tailrace, the confined flow that occurs represents a pressurized internal pipe flow. The characteristics of the draft tube discharge and its interaction within the tailrace waters are of interest in understanding the flow just downstream of the powerhouses. Here, turbulent wall-bounded jets are expanding into a body of water closely resembling a deep pool with a relatively low ambient velocity.

In addition to determining what the time averaged vertical velocity profiles will look like, the placement of a hydrokinetic turbine in the vicinity of the powerhouse needs to consider the large scale velocity fluctuations that can be found in this area and their dissipation. There are two factors that stand out as the primary contributors to the large scale turbulence which could affect the performance of hydrokinetic turbines: 1) the complex flow found at the outlet of the draft tubes and 2) the interaction of the wall bounded jets with the surroundings.

3.3.1 Draft Tube Flow

The flow in a draft tube can be highly varying and dynamic, exhibiting swirling flow that can experience regions of boundary layer separation, flow reversal, strong secondary flow and vortices induced by path curvature. By the time the flow reaches the entrance of the draft tube it has been through a cascade of filaments, starting with the stay vanes and wicket gates located in the spiral casing of the Kaplan turbine distributor and lastly the runner blades. Consequently, in designing the

distributor system and the blades, a close link is maintained with the layout of the draft tube in order to have a well behaved flow leaving the runner that will reduce the occurrence of large unsteady fluctuations further on in the draft tube.

The turbines used in the Wanapum and Priest Rapids powerhouses are doubly regulated Kaplan turbines. As opposed to propeller-type turbines, where the pitch of the runner blades is fixed, these turbines allow for adjustment of the blade pitch in addition to control over the flow rate through the closing or opening of the wicket gates -- thus the term “doubly regulated”. The additional control over the blades allows for a wider range of discharges so that peak efficiencies can be obtained. Figure 3.8 shows a photograph of an original turbine from the Wanapum powerhouse and an image of a new turbine. Among the various changes in the design, the spherical hub and unique blade shape of the new turbine stand out. The hub of the new turbine can be distinguished by the change in angle at the joint with the conically shaped deflector near the bottom of the blades. Figure 3.8a also shows the discharge ring around the blades and a section of the conical diffuser. Table 3.3 provides the general parameters of the turbines used at both powerhouses.

a)  *b)* 

Figure 3.8 a) Original and b) new Kaplan turbine used in the Wanapum powerhouse.
Adapted image b) from Grant Country PUD [40]

Typical values commonly used to compare conventional hydroelectric turbines are the specific discharge $Q_{11}$and the specific speed n_{11}. These parameters correspond to the values necessary for

a geometrically similar turbine with a net head of 1m and a runner diameter of 1m to maintain the original operating conditions. These values are defined as,

$$Q_{11} = \frac{Q}{D^2\sqrt{H_n}} \quad (3.7)$$

$$n_{11} = \frac{nD}{\sqrt{H_n}} \quad (3.8)$$

where D and H_n are ratios of the runner diameter and the net head to a runner diameter of 1m and a net head of 1m, respectively, Q(m^3/s) is the discharge through the turbine, and n is the rpm of the runner.

The bulk of the data available for detailed flow analysis inside low-head axial turbines and their draft tubes has come from work done in three workshops (1999, 2001, 2005) sponsored by IAHR/ERCOFTAC focused on the Turbine-99 draft tube test case and experiments performed by the Consortium on Hydraulic Machines in its Axial-T project. The Turbine-99 workshops were aimed at developing tools for the CFD simulation of the draft tube flow. The simulation domain consisted of a conical diffuser followed by a 90° sharp-elbow and a rectangular diffuser with one single bay. Boundary conditions based on measurements taken near the runner exit of a Kaplan turbine with a Q_{11} equal to 1.5520m^3/s and an n_{11} equal to 140rpm, were used [70,71]. The unit tested in the Axial-T project consisted of a propeller-type turbine with 6 blades, a conical diffuser followed by a smooth 90° elbow, and a rectangular diffuser with one dividing pier and two bays. Reported values for this turbine are: Q_{11} = 1.2945m^3/s and n_{11} = 124rpm. The project focused on obtaining measurements in the runner-stator interface, the runner exit/draft tube entrance, and the draft tube outlet, together with simulations that incorporate these measurements [72-77].

The Kaplan turbines found at Wanapum and Priest Rapids scale within an acceptable range with the propeller-type turbine tested in the Axial-T project and the Turbine-99 Kaplan turbine modeled. This provides useful insight on the flow characteristics expected in the draft tubes of Wanapum and Priest Rapids.

Table 3.3 Parameters of the Priest Rapids Project Kaplan Turbines

Kaplan Turbine	Wanapum 'Original'	Wanapum 'New'	Priest Rapids
Diameter (m)	7.239	7.747	7.214
Number of Blades	5	6	6
Rated Head (m)	24.38	24.38	23.77
Rated Discharge (kcms)	0.402	0.504	0.423
Rated Power (MW)	89.52	111.9	85.04
RPM	85.7	85.7	85.7
Rated Q_{11} (m^3/s)	1.55	1.70	1.67
Rated n_{11} (rpm)	125.63	134.45	126.79

From the results, the curvature of the 90° elbow bend is seen to play a very significant role in the distribution of the flow along most of the draft tube, starting from the edge of the conical diffuser leading up the bend and continuing all the way downstream to the outlet. The presence of the bend leads to the development of a strong pressure gradient due to the force exerted on the flow by the concave (outer) wall. The pressure gradient consists of a radial component extending between the concave and convex surfaces, as well as an adverse pressure gradient along the draft tube wall on the concave side acting against the incoming flow [78].

This adverse pressure gradient contributes to the imbalance in the radial velocity near the exit of the conical diffuser and causes a shift of the average peak velocity towards the convex (inner) wall as the flow enters the bend [75,79]. In passage through the elbow, the inertia of the flow drives the peak velocity back towards the outer wall along the center of the cross-sectional area, whereas the radial pressure gradient pushes the flow towards the convex side, establishing a secondary flow that results in the formation of two large counter-rotating vortices that occupy the whole cross-sectional area [78,80]. This secondary flow underlies the streamwise velocity and its effects are present in time averaged results.

The high Reynolds numbers experienced in turbine draft tubes (>$3x10^7$ for a Wanapum unit) also points to the existence of Görtler vortices that propagate from inside the boundary layer along the concave wall [13,59]. These vortices consist of multiple smaller counter-rotating streamwise

vortices lining the concave wall that grow as they propagate downstream and fluctuate in a wave-like manner through the interaction between regions of downward and upward flow between the lateral walls [80-83]. As the curvature increases the interaction of the vortices can lead to highly distorted fluctuating pockets of low momentum fluid that are introduced into the free stream [82]. Figure 3.9 aids in visualizing the underlying secondary flow that is established in the bend and the Görtler vortices.

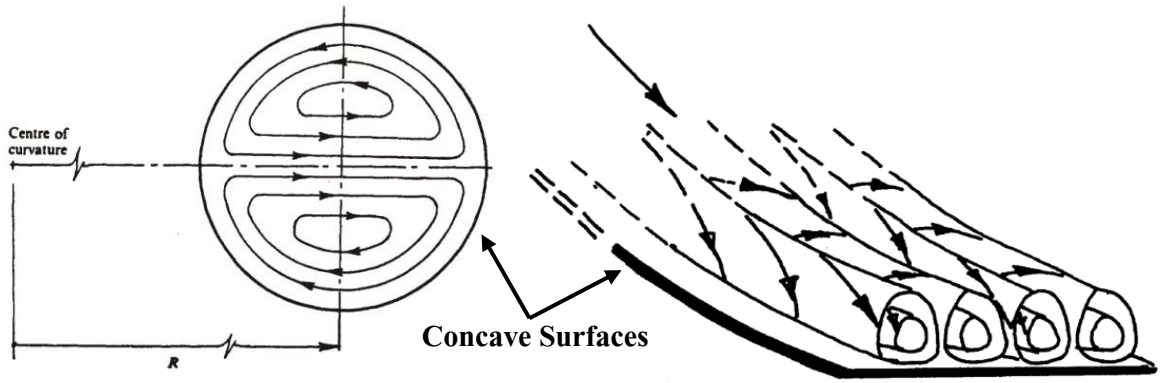

Figure 3.9 Secondary flow and Görtler vortices expected to be present in the 90° bend of the draft tube. The large recirculation pattern shown on the left corresponds to the underlying secondary flow and the pattern of smaller Görtler vortices forming along the concave wall is shown on the right.
Images from Spedding, Benard and McNally [80] and Hall [83]

Through the bend, the cross-section of the draft tube typically goes from a circular entrance to a rectangular exit. The design for the final stretch of the rectangular diffuser out to the tailwaters has been found to vary from one, two or three bays. As shown in figure 2.22, the draft tubes found in the Wanapum and Priest Rapids powerhouses consist of a rectangular diffuser divided by two piers. Paik, Sotiropoulos, and Sale [79] and Zhang, Mao and Wu [84] performed numerical simulations through a Francis turbine draft tube with two piers. Although the inlet conditions to the draft tube are expected to be different for Francis and Kaplan turbines due to varying swirl ratios (tangential velocity/axial velocity) at the runner outlet, the secondary flow induced by the elbow and its strong dominance over the flow is found to be similar. The results show that there is repartitioning of the flow in the draft tube that tends to favor one of the bays.

This split in the flow has similarly been measured at the outlet of the Axial-T draft tube [75] even near the point of best power efficiency and at the outlet of unit 16 at the John Day Dam [85], both cases with the rectangular diffuser divided by one pier. The John Day Dam has slightly larger Kaplan turbines, with a diameter of 7.925m and a rated head of 28.7m. The draft tubes are designed with one single pier and two bays with a combined cross-sectional area of 271.3m^2. Based on testing at various conditions, the split between the two bays of the Axial-T draft tube proved to always favor one of the bays, in this case the right bay. At the nominal operating condition the split was calculated as being 56.5% to 38.5% based on measurements covering 95% of the cross-sectional area. In the case of the John Day draft tube, analysis of Acoustic Doppler Current Profile (ADCP) readings made over the left bay when the discharge was 0.402kcms, revealed a split of 67% to 33%, with the majority of flow going through the left bay. Paik et al. [79] and Zhang et al. [84] conclude that the split is affected by the rotation of the runner and hence that of the swirling flow entering the draft tube. As the draft tube widens laterally downstream of the 90° elbow, the inertia of the rotating particles sends the particles in a tangential direction. If the runner is rotating clockwise the particles will have a tendency to go to the left and if the runner is rotating counterclockwise, as is the case for the Axial-T turbine, the particles will want to go to the right. By looking at the Kaplan turbines used in the Wanapum powerhouse it can be determined that they are designed to rotate in a clockwise fashion and a split in the flow that prefers to go towards the left bay is expected.

From instantaneous profiles generated by Paik et al. [79] at the outlet of the draft tube, a sense is gathered as to how dynamic this area can be, with a highly skewed velocity distribution and regions up to a third of the height of the bays showing strong divergence and precessing circulation. A large region of flow recirculating into the bays and boundary layer separation along the pier walls also appear to be prevalent, especially in the non-preferential bays. Comparing the time-averaged results for these simulations of a Francis turbine draft tube with those of a Kaplan turbine draft tube

reveal a very similar velocity distribution in the preferred bay, with a peak velocity appearing along the outside wall, as determined from the runner rotational direction, and a region of low velocity and possible recirculation along the pier wall.

Figure 3.10 shows the results from the simulation done by Paik et al. [79] at two different time steps as well as the time average results. The images are contoured by the streamwise velocity normalized by a bulk velocity determined with the diameter of the draft tube entrance. Although difficult to distinguish, cross-flow velocity vectors corresponding to the lateral and vertical velocity components are also plotted. Maintaining the point of view travelling with the flow, as expected, the counterclockwise rotation of the flow at the draft tube inlet is seen to lead to higher time-average velocities in the right bay concentrated along the outside wall. The instantaneous results show the high level of variability and strong fluctuations in the flow field expected at the outlet of the draft tube. As reported by Paik et al. [79] the time-averaged cross-flow velocity vectors show that the large scale secondary flow induced by the bend is still present at the outlet, with a counterclockwise rotation noticed in the right bay and a weaker clockwise rotation in the left bay. The velocity distribution for the inlet conditions for the simulation is also shown in figure 3.10.

Findings for the unsteady and periodic phenomena that can be associated with vortices generated in the filament cascade, the strong curvature of the bend, and the presence of the piers, are still lacking in a quantitative sense. Nonetheless, the water at the exit of a draft tube is found to offer a significant challenge in locating hydrokinetic turbines and is not recommended considering the available technology.

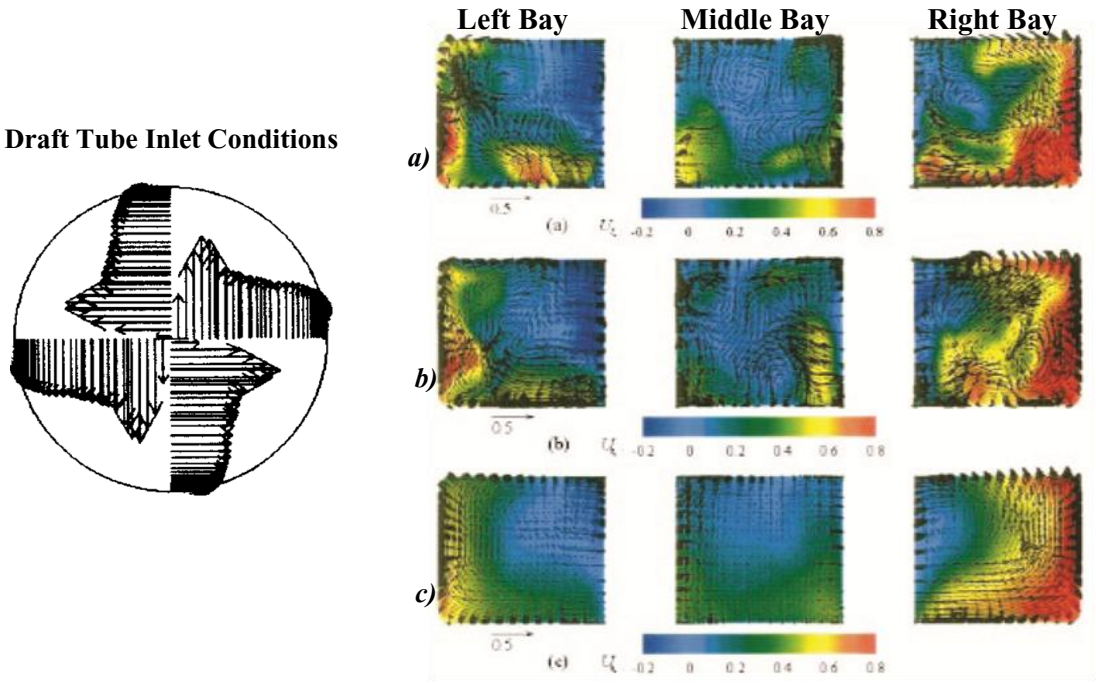

Figure 3.10 Inlet conditions and draft tube outlet results for the unsteady numerical simulation performed by Paik et al. Results show in a) and b) correspond to instantaneous snapshots at two different time steps and c) to the time average results. *Adapted images from Paik et al. [79]*

3.3.2 Draft Tube Outlet Wall-Bounded Jet

Downstream from the draft tube outlet the flow starts to behave like a wall bounded jet. These flows are typically characterized by a velocity profile near the wall, or in this case the river bed, resembling that of an open-channel velocity profile and a top layer similar to that of a free jet [13,86,87]. The situation at hand, however, is more complex than that for which studies have been performed. Four main factors differentiate the case at hand: 1) the turbulent wall jet is exiting onto an inclined surface, 2) there exists a very small ratio between the tailrace depth and the height of the draft tube outlet, severely limiting the volume of surrounding fluid that can be entrained by the jet, 3) the instantaneous flow coming from within the draft tubes has added properties accounting for the convection of turbulence generated in the draft tube, and 4) there are multiple jets coming from the powerhouse at any given time from the different turbines operating, which will have an effect on how each jet interacts with each other and the surrounding fluid.

Among the measurements taken at the John Day Dam by Cook, Dibrani, Serkowski, et al. [85], along-beam readings were made with an ADCP mounted on top of the draft tube's dividing pier, oriented such that the beam was aligned with the direction of the main flow. Although the 1D result does not fully encapsulate the behavior of the emanating jets, it provides the only quantitative result found associated with a spreading draft tube jet. The results for velocity fluctuations presented as RMS values show a very apparent lateral spread of the jet, with the higher levels of fluctuation observed to occur near the draft tube exit plane. At a distance of about 60m downstream from the powerhouse, the velocity fluctuation magnitudes reduce threefold down to between 0 and 0.33m/s. Out of the three different discharges presented, the results for the lowest discharge show both the largest values for the RMS of the measurements near the draft tube outlet and the farthest extension downstream from the powerhouse of these strongest fluctuations, which are observed near the draft tube outlet for all of the discharges presented. This is likely to be associated with the partial loading of the turbine which leads to a substantial division of flow between the bays and sizeable recirculation in the one showing the larger fluctuations. A look at the bathymetry shows that at about the 60m distance, a steep positive bed slope of ~14° (degrees) in front of the powerhouse begins to decrease significantly. In comparison, the slope in front the Wanapum powerhouse based on the independent bathymetry data is roughly 9°, whereas the slope in front of the Priest Rapids powerhouse is steeper, at approximately 19°.

Although the IIHR simulations for Wanapum and Priest Rapids dams do not consider the intricate path through the turbine system and the draft tube, the simulations do capture the time averaged behavior of the jets issuing into the tailrace waters from the powerhouse. Simulation results obtained for planes running perpendicular to the Wanapum and Priest Rapids powerhouses through the middle of one of the draft tube jets are used to study the flow behavior. Similarly to the vicinity of the John Day Dam, the river bed bathymetry is characterized by an initial steep positive slope that decreases in the downstream direction in the transition to a small negative slope. Data from

each downstream location is extracted along lines normal to the river surface. Along this stretch, the streamwise velocity is calculated at each point using the three velocity components $(u_i, i = 1{:}3)$,

$$u = \sqrt{u_1^2 + u_2^2 + u_3^2} \qquad (3.8)$$

For the Wanapum Dam the data plane crosses through the middle bay of powerhouse unit 6 and for the Priest Rapids Dam it corresponds to unit 4.

The results reveal key differences in the progress of the draft tube jets. For the Priest Rapids tailrace, the jet peak velocity is observed near the lower 20% of the water column until its dissipation. Two data sets from the Wanapum powerhouse show a jet peak velocity remaining near the river bed until its dissipation, and two others point to a jet peak velocity moving up through the water column, eventually reaching the free surface. The behavior of the latter two cases coincides with that expected of wall bounded turbulent jets, where the growth of the turbulent boundary layer along the river bed causes dissipation of the velocity near the bed surface [86-91]. Figure 3.11 shows the results for one of these simulations, with an average unit discharge of 0.501kcms. The jet is seen to expand to the free surface immediately downstream from a recirculation region that develops in front of the powerhouse and undergo a transition from a free-jet profile to an open-channel profile.

It is interesting to compare the flow at the powerhouse exit to that of a sluice gate. The principal difference between these hydraulic structures is that the bulk of the energy potential is extracted by means of the turbines in a dam and not dissipated in a hydraulic jump as in the sluice gates. Due to this, the velocity at the draft tube outlet is substantially lower than that found at the sluice gate opening and the flow is subcritical. For instance, using a unit discharge of 0.501kcm, a cross-sectional area of 170.5m^2 (corresponding to the Wanapum draft tubes), and an outlet height of 8.73m, the *Fr* number of the draft tube outlet is 0.32.

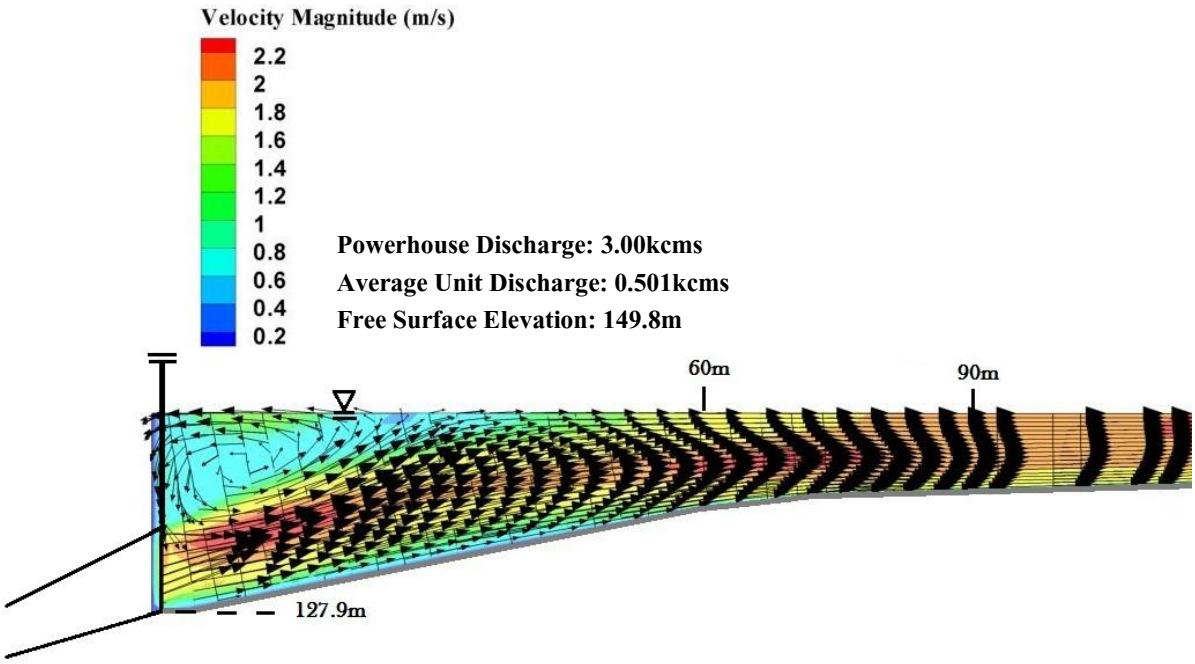

Figure 3.11 Data plane running perpendicular from the Wanapum powerhouse through the middle bay of unit 6. Vectors correspond to extraction lines perpendicular to the river surface. The distance is normal to the powerhouse.

Experimental studies of sluice gates carried out by Dey and Sarkar [88] and Ead and Rajaratnam [89,90], concur that the growth of the turbulent boundary layer that develops between the flow and the bed is responsible for the transfer of the point of maximum velocity up to the surface. The surfacing of the jet is taken to occur just downstream from a recirculation region that develops close to the gate. This recirculation region resembles the recirculation captured in the simulations, as depicted in figure 3.11. The photograph shown in figure 3.12, taken in front of the Wanapum powerhouse, shows the surface of the water where this recirculation in the upper part of the water column is expected to be occurring. Large surface boils are very distinct and can be seen in front of unit 1. The fish ladder, in the right hand side of the figure next to unit 1, is operating.

Figure 3.12 Large surface boils in front of the Wanapum powerhouse.

Next, the behavior of the maximum velocity is studied. Figure 3.13 shows the behavior of the normalized maximum velocity (u_{max}) as a function of the normal distance from the Wanapum powerhouse for the two simulations depicting the expected wall-bounded jet behavior, with the bed elevation also shown. In this figure, u_{max} is normalized by the maximum velocity found at the upstream edge of the simulation domain (corresponding to the draft tube outlet). The flow recirculating back towards the powerhouse is not analyzed. The distribution of the normalized maximum velocity for the other simulations is found in Appendix C.

As seen in figure 3.13, both simulations show a region near to the powerhouse that extends up to about the 15m mark where u_{max} increases in comparison to that found at the draft tube outlet, reaching a maximum of 1.17 for the case with an average unit discharge of 0.501kcms and 1.19 for the 0.460kcms case. This region where the magnitude is increasing is observed to occur underneath the recirculating zone that is seen in figure 3.11. It is noted that the occurrence of this increase is observed in all of the simulations. From the point of maximum increase the value starts to decay as

expected from the literature, however all of the simulations show a second region where the ratio increases again. Generally, the simulations show that the second peak is reached near the region where the positive bed gradient starts decreasing. In figure 3.13 the second peak for the 0.501kcms unit discharge is centered close to the 65m mark and closer to the 50m mark for the 0.460kcms case. This second peak in velocity is attributed to the decrease in depth that occurs as the river bed rises. This follows from conservation of mass, as the decrease in cross-sectional area associated with the decrease in depth leads to an increase in velocity.

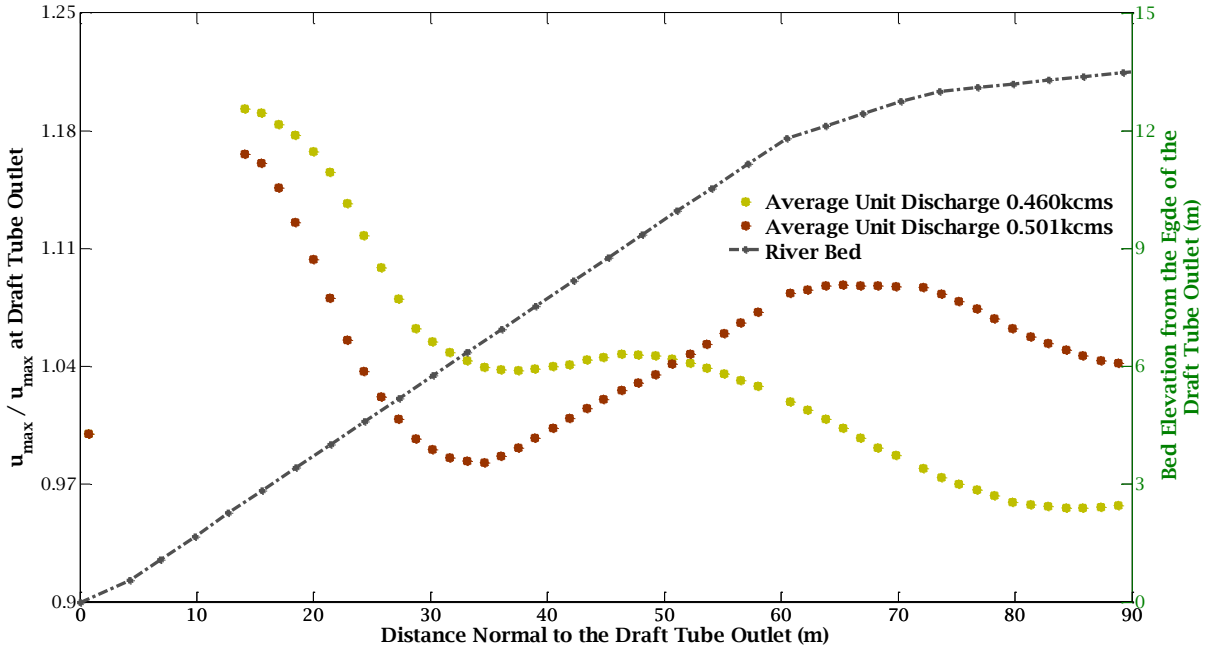

Figure 3.13 Behavior of the normalized maximum velocity as a function of distance from the draft tube outlet. The plots correspond to simulations of the Wanapum tailrace with an average unit discharge of 0.460kcms and 0.501kcms.

Although the two simulations in figure 3.13 capture the behavior of a wall-bounded jet, more information would be helpful to completely understand the combined effects of the steep bed gradient and the interaction with the surrounding jets which will have an impact on both the lateral and streamwise behavior of the jets. The two simulations show agreement in the span of the first region where the velocity magnitude increases. The case of 0.501kcms, however, undergoes a larger velocity magnitude increase than the 0.460kcms case in the second region. For the

0.501kcms case, the jet coming from unit 6 is shadowed on both sides by the discharge from units 5 and 7, whereas in the case of 0.460kcms the simulation corresponds to a jet that is only shadowed on one flank by the discharge from unit 5.This shadowing could be playing a role in the propagation of higher velocities for the case of 0.501kcms due to a smaller dissipation rate that comes from smaller velocity deficits with the surrounding flow. This is a matter that requires further attention.

For an estimate on the kinetic power available along this reach of the tailrace, the location chosen as the most appropriate for placement of a hydrokinetic turbine is the region where the bed gradient first decreases. This corresponds to a distance between 65 to 80m from the Wanapum powerhouse and 35 to 45m from the Priest Rapids powerhouse. These areas are chosen because a significant velocity increase might be occurring along this stretch, and because they coincide with the nearest point to the powerhouse where turbulent fluctuations appear to have decayed substantially, as inferred from the results for the John Day tailwaters.

Figure 3.14 shows a typical velocity profile along the stretch chosen for siting labeled with the characteristic points of interest for a wall-bounded jet profile. In order to see if the behavior of the jet is self similar, the velocity points for each profile along the region of interest are normalized by the u_{max} of each profile, and the height above the bed (z) is normalized by $h_{1/2}$, where $h_{1/2}$ is a characteristic height located above u_{max} (as shown in figure 3.14). For wall-bounded jets that have an immense expanse of fluid above, $h_{1/2}$ is typically taken as the location where the velocity is half of the maximum velocity. In the case of a limited tailrace elevation the free surface velocity is also included [91] and $h_{1/2}$is defined where,

$$u = \frac{(u_{max} + u_{free\ surface})}{2} \qquad (3.9).$$

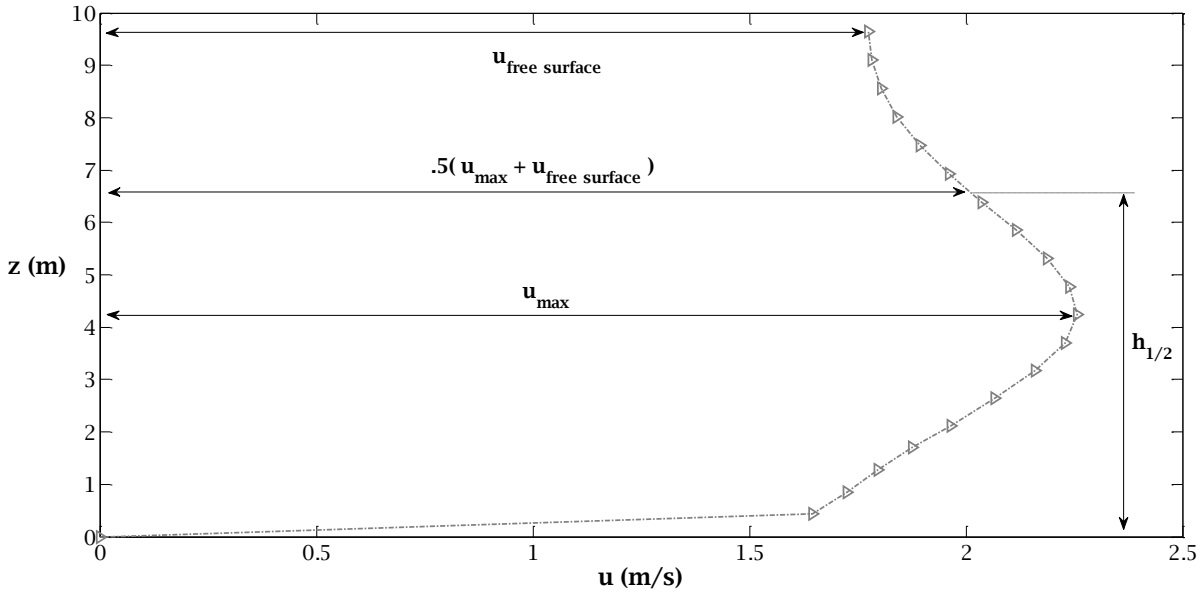

Figure 3.14 Typical velocity magnitude profile along the region where the bed gradient decreases in the vicinity of the Wanapum powerhouse. The data corresponds to one of the profiles from the simulation of an average unit discharge of 0.501kcms. The plot includes labels for the points of interest used to normalize the velocity data.

In figure 3.15 the normalized height versus the normalized velocity magnitude is plotted for the two simulations showing the wall-bounded jet behavior in the span of the bed gradient where the second increase in velocity magnitude is observed.

Attempts to match the velocity profiles with theoretical curves did not prove fruitful. However, an empirical relation is established for the data corresponding to the profiles at x = 65.3m. These data are chosen as a representative velocity profile used to approximate the kinetic power available at the location where the positive bed slope starts to decrease. The relation is given as follows:

$$\frac{u}{u_{max}} = a1 * e^{-((x-b1)/c1)^2} + a2 * e^{-((x-b2)/c2)^2}; x = \frac{z}{h} \qquad (3.10).$$

The lateral spread of the jet at this location is not investigated. This lateral behavior is expected to be quite complex and strongly affected by the presence of surrounding jets. Figure 3.16 shows the normalized extracted data and the empirical fit for the two profiles, and table 3.4 lists the constants found for the empirical formulation.

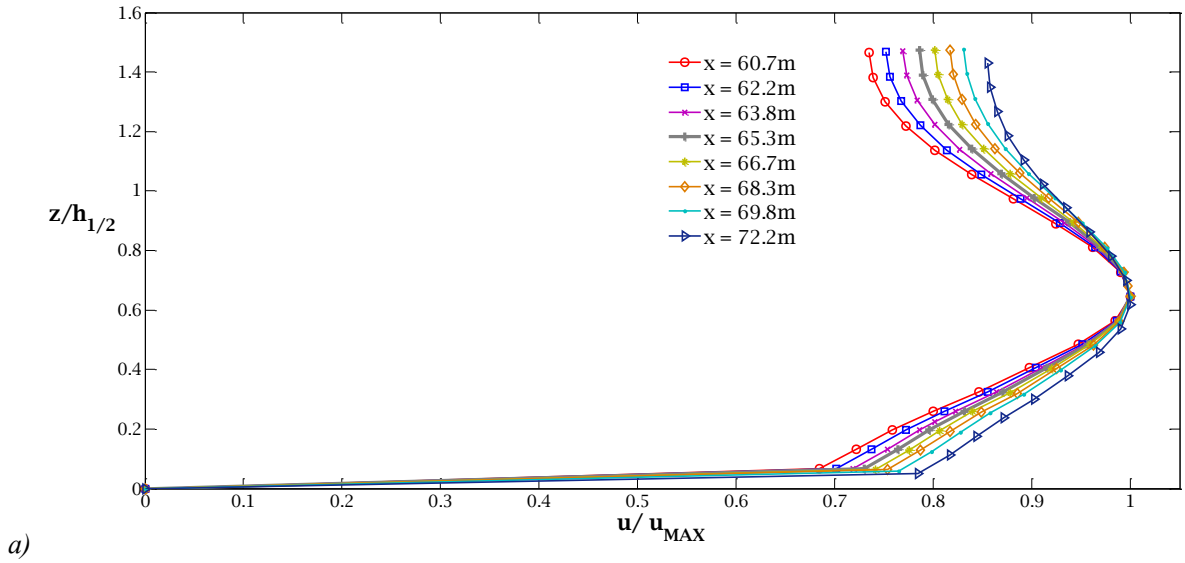

a)

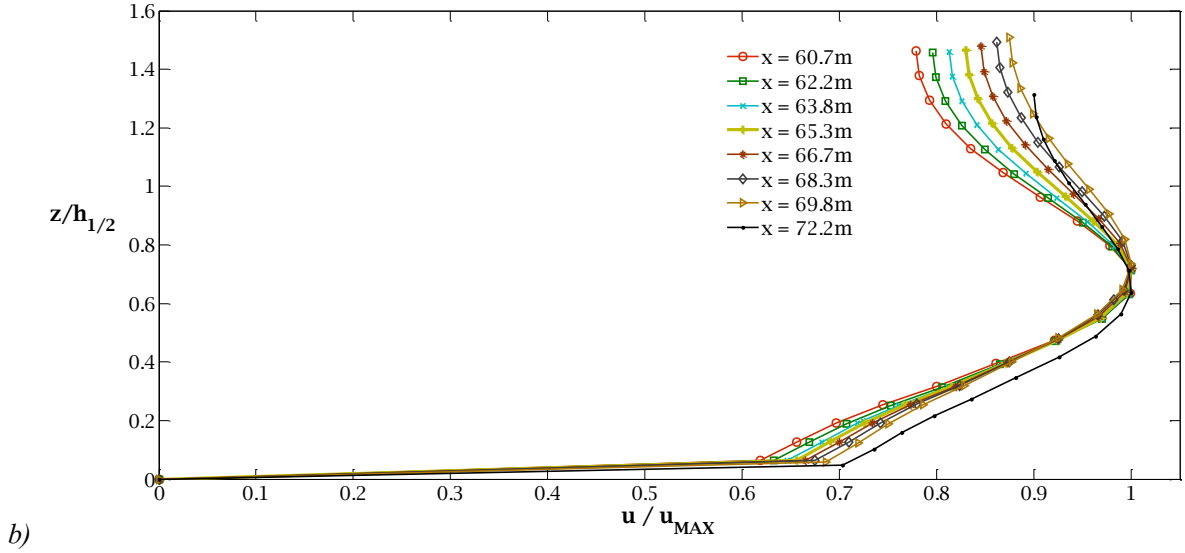

b)

Figure 3.15 Normalized heights vs. normalized velocity magnitude along the region of bed gradient decrease in the powerhouse vicinity for the Wanapum Dam simulations. Plots correspond to the simulation of an average a) 0.501kcms per unit and b) 0.460kcms per unit.

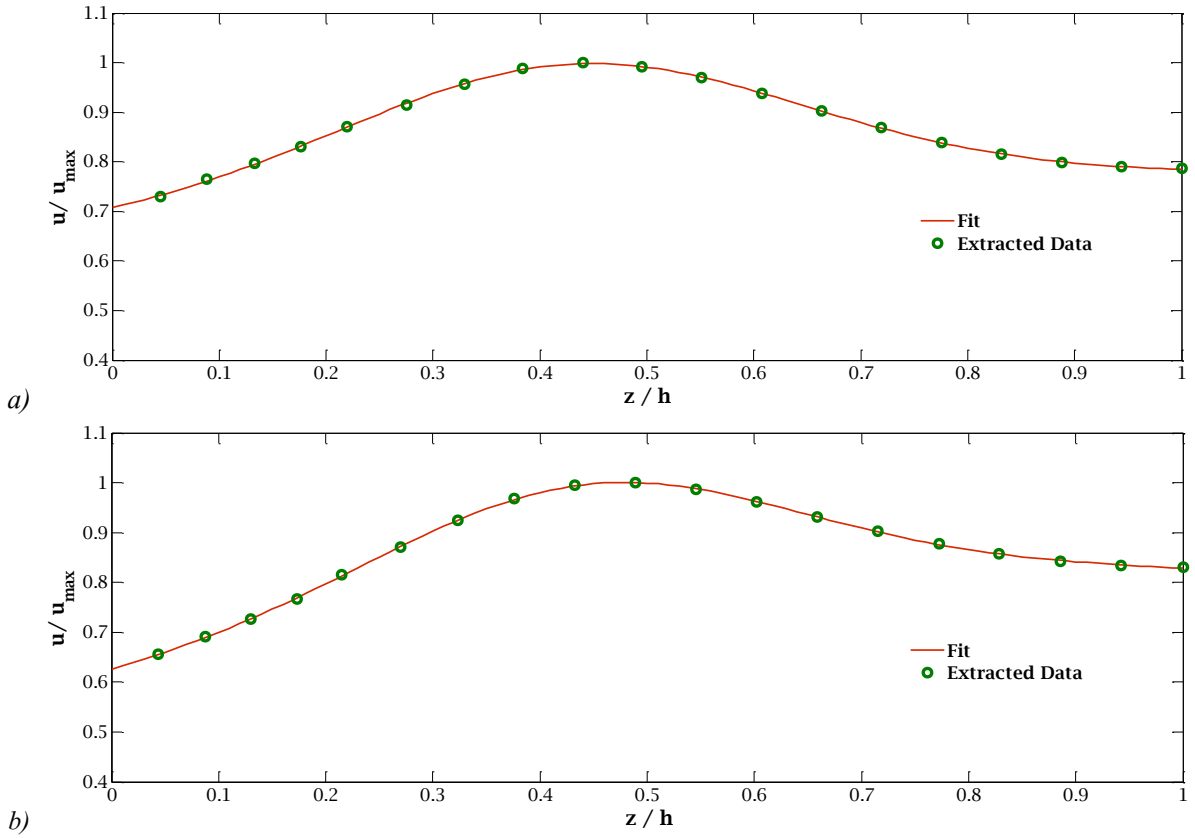

Figure 3.16 Representative normalized velocity vs. normalized height in the powerhouse vicinity. Plots are for a) an average unit discharge of 0.501kcms and b) an average unit discharge of 0.460kcms, at the point 65.3m away from the powerhouse, where the bed gradient is decreasing.

The velocity magnitude distribution exemplified by the profile shown in figure 3.16a has an u_{max} that is 1.09 times larger than the u_{max} found at the draft tube outlet for the corresponding simulation, whereas the profile shown in figure 3.16b has an u_{max} that is equal to the u_{max} found at the draft tube outlet. (This follows from the results indicated in figure 3.16 for x = 65.3m.) The point of maximum velocity occurs near the mid-point of the total depth but is slightly shifted closer to the river bed for the profile shown in figure 3.16a. It is also noted that both profiles exhibit a similar velocity deficit in the upper part of the profile, with a free-surface velocity close to 80% of the peak velocity. The case depicted in figure 3.16a shows a smaller velocity deficit in the lower part of the water column, by almost 10%, providing a fuller profile across the whole water column that is deemed more optimal for hydrokinetic turbine placement.

Table 3.4 Constants for the Empirical Velocity Profile Equation Used in the Powerhouse Vicinity

Fit Parameters	$a1$	$b1$	$c1$	$a2$	$b2$	$c2$	R^2	**RMSD (m/s)**
Average Unit Discharge 0.501kcms	0.2573	0.428	0.3008	0.7781	1.049	2.761	0.9997	0.0019
Average Unit Discharge 0.460kcms	0.2336	0.4375	0.2769	0.8271	0.906	1.627	0.9998	0.0019

IV- Deployment

Deployment of a hydrokinetic turbine in a tailrace needs to take into account a variety of matters that can have an effect on performance and safety. Ideal placement would provide sufficient clearance between the rotor blades and the free surface at all stages of the river and would not conflict with other uses of the water while remaining closely aligned with the highest power density in the flow and reasonably low levels of turbulence.

For a shallow water deployment, depending on the design of the blades and the pressure drop that occurs across them, losses associated with cavitation near the tip of the blades could be of concern. The turbine conceptualized in the EPRI study on river deployments for Alaska [10] set a blade tip speed of 8m/s as a limiting factor in order to prevent low pressures on the blade tips from inducing cavitation. Mr. Monty Worthington [18], director of project development for ORPC Alaska, and Dr. Ed Lovelace [25], executive vice president of engineering for FFP, stated in conversations that in their expected deployments they did not foresee cavitation being of concern in the functionality of their devices. For the high speed EnCurrent turbines rated between 5 and 25kW, the tip speed does not exceed 7.5m/s [20] and can be assumed to not present a problem.

At this early stage in the development of RISEC technology, the effect of turbulence on the performance of hydrokinetic turbines and the size scales of the turbulence that matter are still under investigation. Deployment of turbines in turbulent waters will undoubtedly have an effect on the dynamics of the flow over the blades and have an effect on the drag and stress loadings on a turbine system.

For placement of the turbines, conflicting use of the waters close to the powerhouses is not seen as being of concern. Based on the field visit, the tailrace waters for the Priest Rapids Dam do not appear to be a place frequented by boats and are not easily accessible. Fishing and boating activity

appears more prevalent in the tailrace of Wanapum Dam, but mainly about 900m downstream from the constriction, near two islands that exist along the left bank.

Two ways deemed feasible for positioning the turbines at the sites are to float them off of a barge on the free-surface or to mount them on a standing structure resting on the river bed. Most of the turbines that will become available offer this duality, with the specific configuration site dependent. Options for anchoring either a floating barge or a standing structure can vary from using gravity based to drilled piles to anchor plates. The detailed specifics of these options have not been considered in this work. As a starting point, this would require structural analysis for different system designs, geotechnical information on the river bed composition, and a detailed price comparison between the various options. Table 4.1 lists general characteristics associated with each type of deployment. Table 4.2 lists some pros and cons that could be expected from gravity and fixed anchors. Applicable experience found in the literature is used as guidance, however, this is limited to barge mounted deployments. The information in the tables has not been validated with actual results and does not account for details concerning deployment of hydrokinetic turbines; thus, it should be considered as an overview. With the limited experience in deploying hydrokinetic turbines, the expertise found in the deployment of ocean drilling oil platforms and that of constructing bridges in rivers should be a source for acquiring skills relevant to underwater drilling, deploying bottom support structures, and in designing floating platforms.

Table 4.1 Characteristics of Floating and Bottom Mounted Structures

Characteristics	**Structure Type**	
	Floating	**Bottom Mounted**
Energy Generation	Optimal; captures higher power density found near the free surface	Sub-optimal; can be subject to lower velocities and higher turbulence generated near the river bed
Conflicting Water Use	Presents a clear obstacle in the waterway that forces it to delineate a perimeter	Can offer clearance above allowing for boat traffic to pass except for cases of low water levels and placement in shallow rivers
Essential Equipment	- floating barge/pontoon - debris diverter (possible) - work boat - ~150m of chains or attachment lines - safety lines running to shore - guide buoys during deployment, not fixed - pulley system attached to shore or structure for positioning the work boat, not fixed (possible)	- work boat with a winch or crane - debris diverter (possible) - safety lines running to shore - guide buoys during deployment, not fixed - pulley system attached to shore or structure for positioning the work boat, not fixed (possible)
Electrical Cable	- Run along the attachment line to the anchor and from there to shore or connection point for multiple units - Weighed down or laid in a trench for section running along the river bed	- Run down the downstream side of the support structure to the river bed and from there to shore or to connection point for multiple units - Weighed down or laid in a trench for section running along the river bed

Table 4.2 Anchoring Options

Anchor Type	*Pros*	*Cons*
Gravity Based	- Can be lowered into position - Easier to remove if needed - Does not require divers - Does not require drilling, trenching or excavating - Can offer more economical options for materials used such as concrete or aggregate	- Requires high density material to reduce the footprint - For floating deployments: requires attachment lines that cross through the water column, increasing the system's overall footprint - If too large, can be more susceptible to scouring effects that lead to instability - Requires sufficient mass and size to resist the overturning moment exerted on the anchor by the turbine - Economical material options can require a high volume to achieve robustness - For bottom mounted deployments: large anchors can interfere with the flow and affect the performance of the blade when it is in a position close to the anchor
Fixed Anchor Plate / Drilled Pile	- Can offer a smaller footprint since higher density materials are used - Can obtain higher robustness without substantially increasing the volume - For bottom mounted deployments: a low profile anchor plate will offer the least interference with the flow and the performance of the turbine blades	- Requires heavy machinery for drilling - Likely requires the use of divers - Minimal footprint and high robustness requires deeper drilling - Can present a higher degree of environmental stress during installation - Offers a more complicated scenario to remove

Some environmental effects that accompany a deployment can arise from the alteration of habitat for fish and animals. The structures could become predation sites, could inhibit the ecosystem or offer a new structure for enhanced biological growth.

4.1 Downstream Sites

Based on the velocity profiles studied in the preceding chapter, the region of highest power density is located in the upper part of the water column. For power extraction purposes a free-surface deployment would be preferable, since it continuously remains in best position relative to the fast-moving water. However, in shallow water difficulties could arise for such a deployment if the depth reduces to a distance similar to that of the turbine diameter. This would require action to prevent the turbine from touching the river bed. For free-surface deployments, additional consideration has to be given to the frequencies at which the floating barge will fluctuate due to free surface waves, due to rotation of the blades, and due to the response of the anchor chains. If necessary, a means to dampen resonance amplification that could arise from the combined frequencies may need to be put in place in order to prevent excesses that could result in damage to the system or degrade turbine performance.

If the support system of the turbine is mounted on the river bed instead, it would be preferable to keep the rotor fully submerged at all times to ensure generation if the velocities allow for it. It would also be beneficial to keep the rotor above approximately a third of the depth in order to avoid the lower part of the turbulent boundary layer where the highest velocity deficits and shear forces are expected to occur. By default, as the river stage increases the turbine is left in a non-optimal position since the power density shifts upwards from the center of the turbine. This form of deployment would avoid the use of attachment lines necessary for a floating barge, but if boat traffic is expected a minimum clearance will need to be determined.

4.1.1Wanapum Tailrace

In section III it was shown how the simulation for the ~50% exceedance discharge can be considered as the 'neutral' operating condition, with the velocities more evenly distributed across the main channel including the thalweg. For positioning of a pilot scale deployment, the power density across the site calculated for this medium discharge is once more used as the guideline. Figure 4.1 shows a plot of the power density across the whole river and a close-up of the siting region of interest for the 3.00kcms discharge. A rough depiction of a 25kW low speed EnCurrent turbine is placed in the chosen micro-site recommended for a pilot scale deployment within the region studied. Figure 4.2 similarly shows the power density contours for the low (1.70kcms) and high (5.79kcms) discharges across the whole river, accompanied by a close-up showing the approximate areas that would be occupied by the two largest turbines considered. The portrayal of the turbines is also shown in the plane spanning the river. In figure 4.2a the drawing is representative of a Tocardo T150-A and in figure 4.2b it corresponds to a 125kW low speed EnCurrent turbine. The average depth at the micro-site is 9.30m, 9.89m, and 10.88m for the low, median, and high discharges, accordingly. Note: the datum for the depth is set at the river bed elevation corresponding to the chosen micro-site centered near the 50m mark across the site and the view is looking upstream.

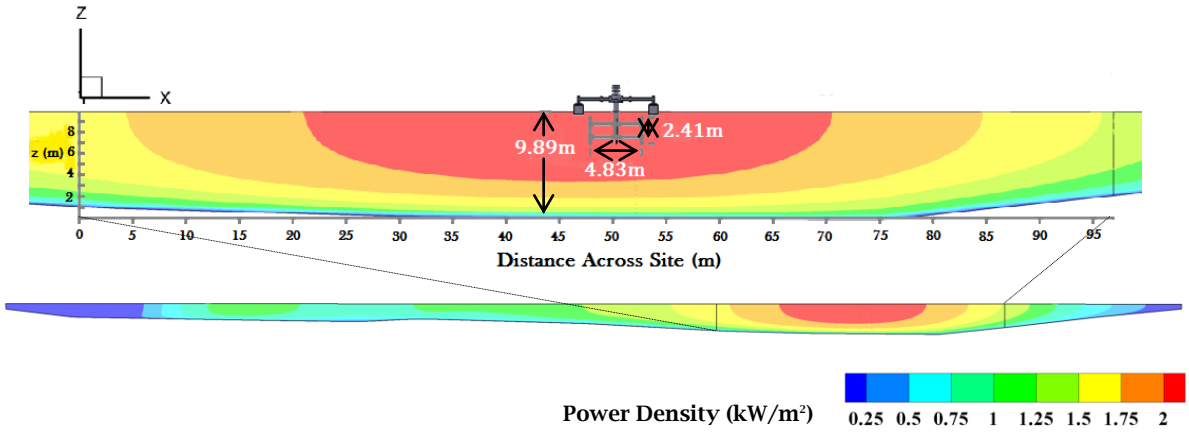

Figure 4.1 Power density contours in the Wanapum downstream site and across the whole river for the ~50% exceedance discharge. An approximate depiction of the low speed 25kW EnCurrent turbine is shown in the area (micro-site) chosen to quantify a pilot scale deployment.

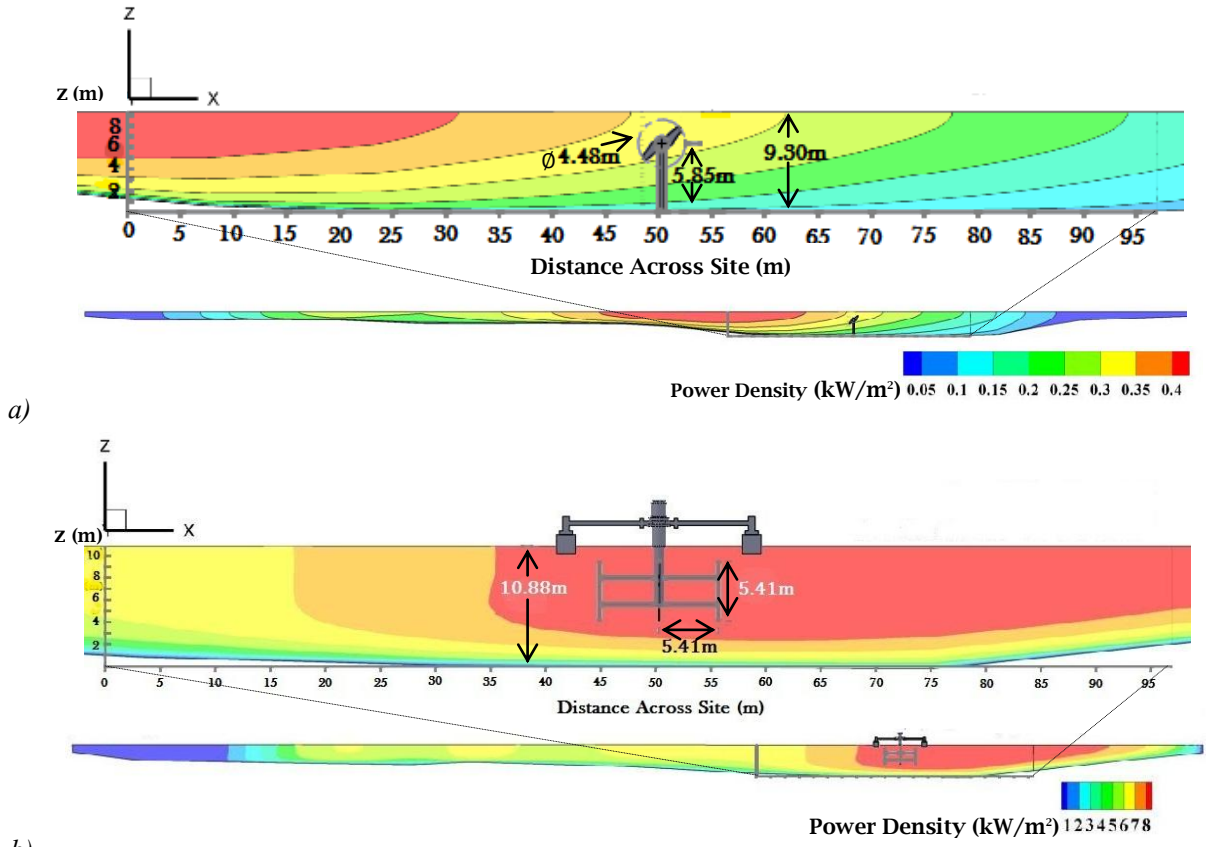

Figure 4.2 Power density contours across the whole river and the siting region for the Wanapum downstream site. The figures in a) correspond to the 95% exceedance discharge and b) the 5% exceedance discharge. The representative scale of the Tocardo T150-A turbine is shown in a bottom mounted scenario in a). It is noted that the operational configuration associated with the fish bypass causes for the peak power density to shift to the right side of the site. In b) a representative figure is shown for the low velocity 125kW EnCurrent turbine in a floating deployment.

4.1.2 Priest Rapids Tailrace

Positioning of a single unit in the downstream site in the Priest Rapids tailrace is influenced primarily by the depth. Access to the high power density that is observed in the flow throughout the site is seen to be limited by a place to fit a turbine without experiencing some of the drawbacks addressed above for shallow sites. Based on the 15yr probability distribution, around 10% of the time low river stages will cause rotor exposure for bottom mounted supports and would require the need for a preventive mechanism so the turbine does not touch the river bed from a floating

deployment. Figure 4.3 shows the power density distribution across the river and the site for the ~50% exceedance discharge (3.91kcms). The location recommended for power extraction falls where the representative image of a Tocardo T50-A mounted in a floating structure is shown. In figure 4.4, the power density contours for the low (1.82kcms) and high (5.72kcms) discharges are shown alongside the considered bottom mounted positioning for the Tocardo T50-A, as well as a characteristic free-surface deployment scenario for the high speed 25kW EnCurrent. The power density for the whole data plane spanning across the river is shown for both discharges. In the same manner as with figures 4.1 and 4.2, the datum for the height is taken at the river bed elevation along the micro-site identified inside the siting region and the view on the planes is looking upstream. The average depth at this micro-site is 4.31m, 6.08m, and 7.23m for the low, median, and high discharge, respectively.

The Priest Rapids site has greater velocities than the Wanapum site, as discussed above. This trend is seen by comparing maximum power density in figure 4.3 with figure 4.1, as well as figure 4.4a/b with figure 4.2a/b. The maximum magnitude of velocity is 3.9 m/s for Priest Rapids for high discharge (figure 4.4b), which compares to a maximum of 2.5 m/s for Wanapum for high discharge (figure 4.2b).

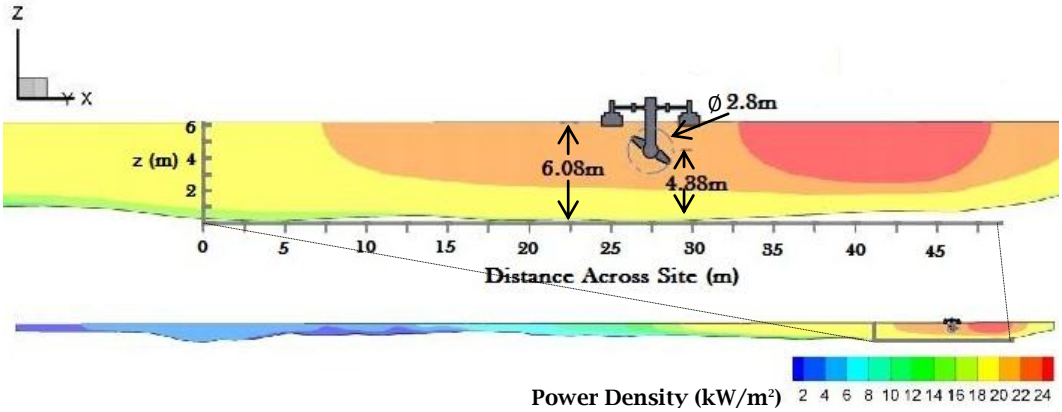

Figure 4.3 Power density contours across the Priest Rapids downstream site and the whole river for the ~50% exceedance discharge. The area chosen to site a pilot scale deployment is identified by the placement of the representative figure, considering a Tocardo T50-A floating off of a free-surface deployment.

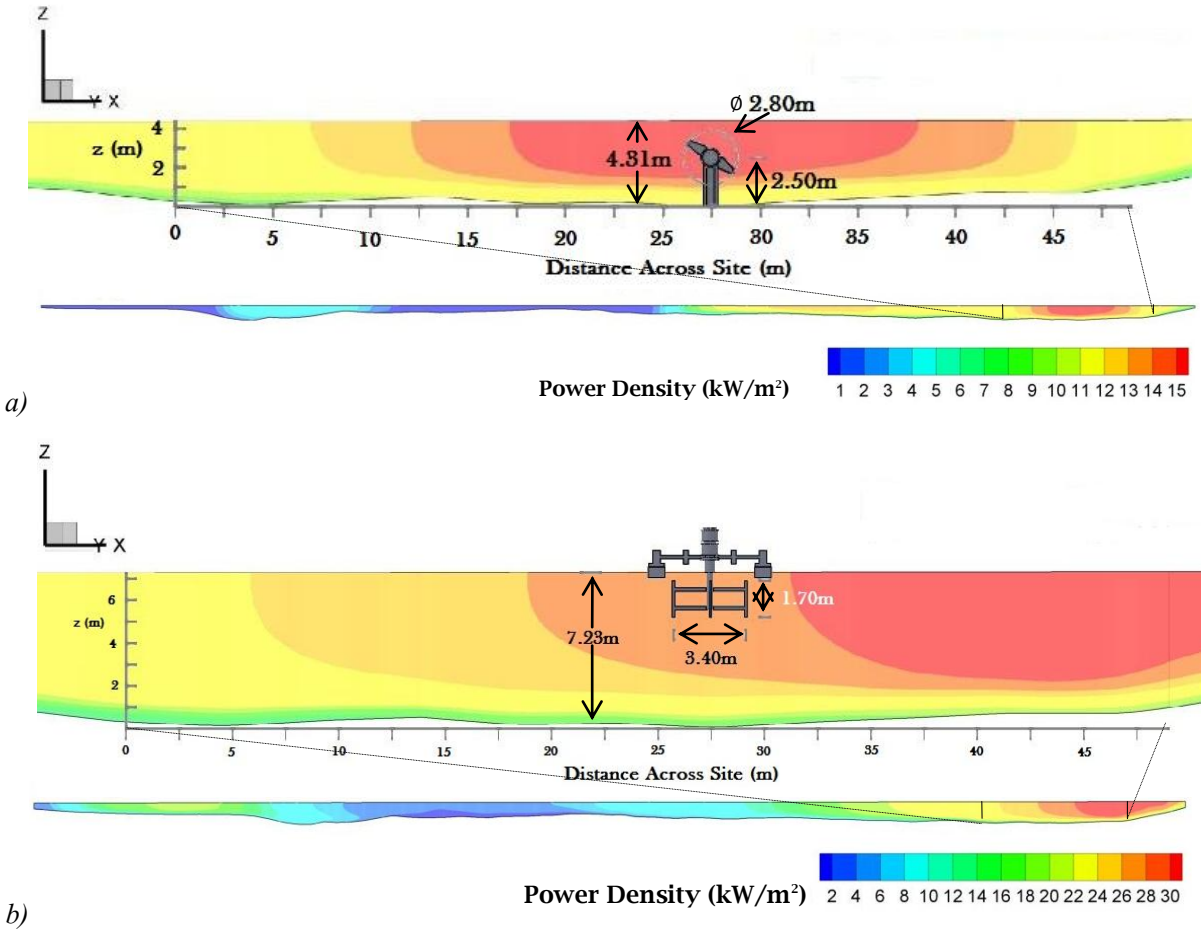

Figure 4.4 Power density contours across the river and region for siting in the Priest Rapids tailrace for a) the 95% exceedance discharge and b) the 5% exceedance discharge. Figure a) shows a representative scale of the Tocardo T50-A mounted on the river bed and figure b) shows a high velocity 25kW EnCurrent turbine positioned in a floating scenario.

4.2 Powerhouse Vicinity

As seen in section III, the jet-like profile coming from the draft tube has a peak found near the mid-span of the water column. A free-surface deployment by barge would enable a continuous placement of a device in this area of peak power density for varying surface levels. For a floating structure, the powerhouse can serve as an anchor point, but for this type of structure the dynamic response to the active waters found in this vicinity will likely need further consideration. A bottom mounted device can offer higher stability through the rigidity expected of a foundation resting or

attached to the river bed away from the influence of any strong surface waves or upwellings that are likely to appear in the powerhouse vicinity.

Figures 4.5 and 4.6 show a layout considered for a bottom and free surface deployment in the vicinity of the Wanapum and Priest Rapids powerhouses, respectively. Figure 4.5 depicts a turbine occupying an area scaled to that of a Tocardo T150-A device. A close-up of the illustration is also shown in figure 4.5 alongside the velocity vectors corresponding to the profile presented in figure 3.16a. In figure 4.6, the vertical axis turbine portraying a floating scenario is scaled to the low velocity 25kW EnCurrent model. The profile chosen to describe the stretch of the powerhouse vicinity where the positive river bed slope starts to change is also shown in figure 4.6.

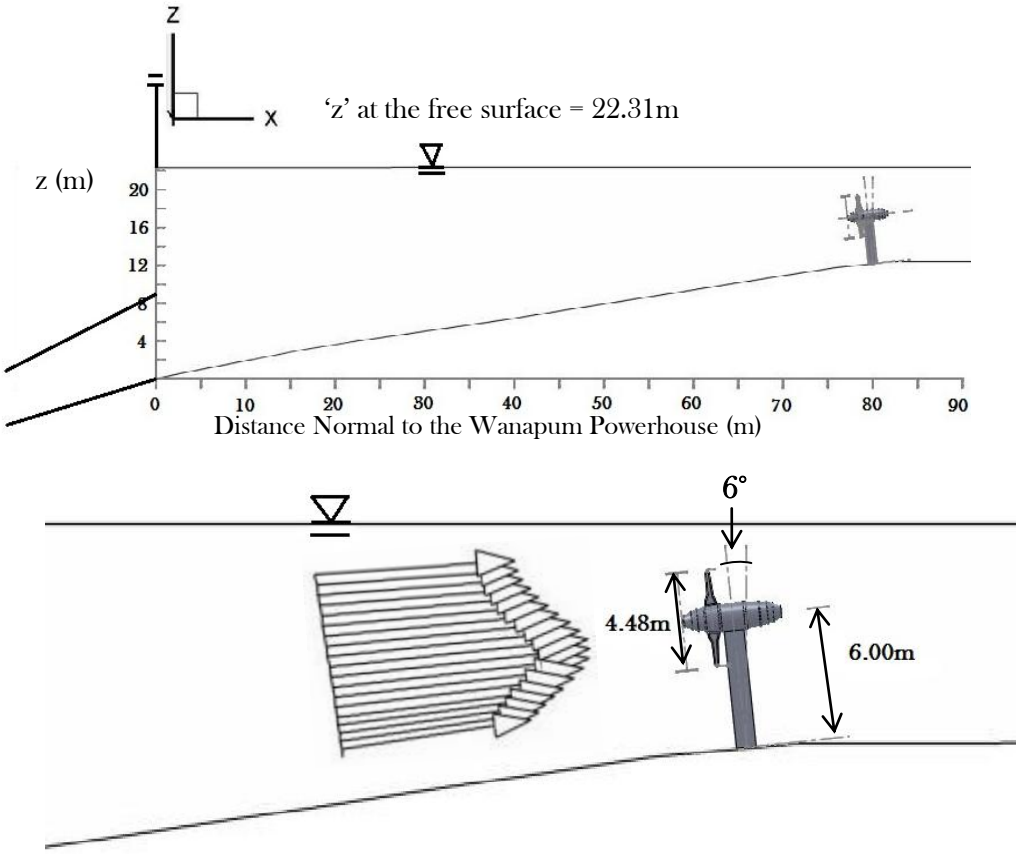

Figure 4.5 Typical arrangement considered for bottom mounted deployments in the vicinity of the Wanapum powerhouse. The area occupied by the figure of the turbine is scaled to that of the Tocardo T150-A. The height of the river bed corresponds to that of the independent bathymetry data and the velocity vectors are those for the profile identified at x = 65.3m in figure 3.16a.

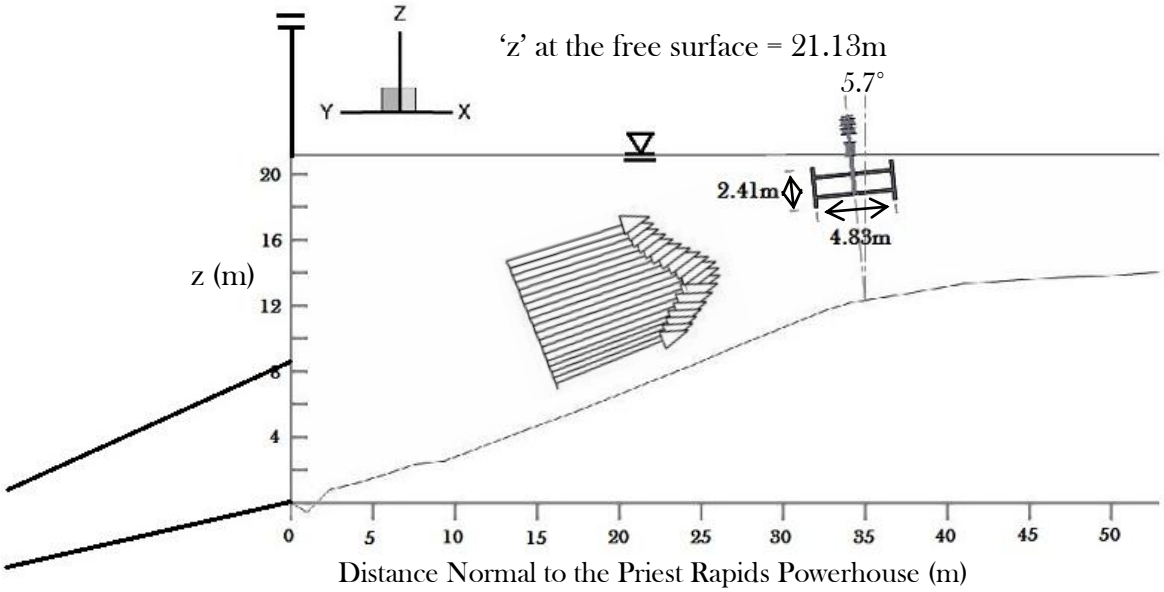

Figure 4.6 Illustration of a hydrokinetic device deployed on the free surface in the vicinity of the Priest Rapids powerhouse. The area covered by the turbine depiction is based on that of a low velocity 25kW EnCurrent model. The velocity vectors shown for visualization purposes are those for the profile identified at x = 65.3m in figure 3.16a.

Based on the velocity profile and the positive bed slope, it is noted that the ability to optimally align the rotor of the hydrokinetic turbine such that it intercepts the flow perpendicularly, will allow the device to harness energy from the full potential of the flow. In figure 4.6 it is seen how the limitation on allowable tilt for the EnCurrent series does not allow the turbines to be oriented with the slope of the river bed. Immediately downstream from the point bed gradient inflection (at a distance close to 35m normal to the powerhouse), the average slope decreases by almost half from the steep slope (higher than 20° in some parts). Since the change is so abrupt, the flow is expected to continue travelling in a more upwards trajectory through this point, before adapting to the free surface and regaining a path parallel with the river bed. A better alignment can exist with a tilt in the device closer to 20°.

V - Power and Energy Generation from a Pilot Scale Deployment

As deemed adequate under the conditions set forth for this study, the consideration of a device pilot scale deployment, using a single full-scale hydrokinetic turbine, is viewed as a sufficient means to weigh the feasibility of the hydrokinetic technology. With only one hydrokinetic turbine located in the deployment region, the small ratio between the rotor's cross-sectional area and the cross-sectional area of the river transect allows for blockage ratio influences on turbine performance and stream flow to be neglected [92,93]. That is, the turbine is assumed to perform as if placed in a stream of infinite area.

From the turbine manufacturers listed in section 1.3, all except Hydro Green Energy LLC continue to be in the forefront of the technology development for river application. However, only the EnCurrent and Tocardo Aqua models are currently available, while the appearance of the RivGen™ Power System and the SmarTurbine™ is not expected until sometime in the following two years. Information on the performance of the turbines considered varies, with power generation performance curves only available for the EnCurrent and Tocardo models. Some performance information for the ORPC and FFP devices has been deduced during conversations with representatives of the companies and from the documentation that is publically disclosed in the FERC licensing process. This is less desirable than having manufacturers' performance curves.

Consistent with the EnCurrent and Tocardo machines, the reported 'water-to-wire' efficiency was assumed to be constant inside the rated operational range and is calculated using equation 1.2,

$$P_{gen} = \frac{1}{2}\rho A_c u^3 \eta_e \qquad (1.2)$$

where the known rated power, velocity, and cross-sectional area of the rotor are used and a value of 1000kg/m^{3}is set for the density of water. The 'water-to-wire' efficiency takes into consideration the performance of the blades in converting the flow power into electrical power and the rectifier/inverter process necessary for the current coming from the permanent magnet generators.

Depending on the device, this approach can lead to uncertainty in the calculated power generation because of the dependence of the turbine efficiency on the tip-speed ratio. As an example: for the SmarTurbine™ being developed by FFP, the device is reported to generate 10kW in a flow velocity of 2.25m/s. Taking the diameter as 3m, the value for η_e is calculated to be 24.8%. At this velocity the rotor is reported as undergoing 38 rpm, which corresponds to a tip speed ratio of 2.65. On the other hand, in a velocity of 3m/s the generated power is reported to be 40kW at a rotation rate of 56 rpm. The values at this operating condition give a generation efficiency of 41.9% and a tip speed ratio of 2.93. Thus, from the information available for these two operating points, a dependence of efficiency on the tip speed ratio can be implied, as well as a possible loss in generator efficiency at a partial load. Without further information on the spread of the efficiency as a function of tip speed ratio, and how well the optimal tip speed ratio is maintained, the power generation only can be roughly estimated over a range of conditions.

Table 5.1 summarizes the rated performance parameters of the various turbines. For the estimates on power and energy generation, only the turbines for which performance curves are available are further considered. As an exception the low speed 125kW EnCurrent device is also considered. Since performance curves for the smaller units (5 and 10kW) show the same characteristics as the 25kWunit a scale up to the 125kW device is assumed. Table 5.2 list the parameters used for determining the power generation with the EnCurrent and Tocardo turbines.

Table 5.1 Performance Parameters of the Hydrokinetic Turbines

Turbine Model	Rated P_{gen} (kW)	A_c (m^2)	Rated Speed (m/s)	Rated η_e (%)
New Energy's EnCurrent 25kW/125kW (low speed)	25/125	11.64 / 58.32	2.4	31
New Energy's EnCurrent 25kW (high speed)	25	5.78	3	31
ORPC's RivGen™	30	13.19	3	17
FFP's SmarTurbine™	40	7.07	3	42
Tocardo's Aqua T50-A/T150-A	50/150	6.16 / 15.90	3.5	40

Table 5.2 Characteristics of the Hydrokinetic Turbines Used for Calculating Power Extraction

Turbine Model	η_e	A_c (m^2)	Cut-In Speed (m/s)	Rated Speed (m/s)	Cut-Out Speed (m/s)	Power Generation Between Rated and Cut-Out Speed (kW)
New Energy's EnCurrent 25kW/125kW (low speed)	31%	11.64 / 58.32	1.5	2.4	2.6	25/125
New Energy's EnCurrent 25kW (high speed)	31%	5.78	1.5	3	3.25	25
Tocardo's Aqua T50-A/T150-A	40%	6.16 / 15.90	0.7	3.5	4.8	9 + 10.2(speed-3.5) / 26.8 + 25(speed - 3.5)

5.1 Deployment Assumptions Used for Calculating the Power Generation

For the floating deployments, the turbines are assumed to sit below the free surface at different positions depending on their size, and when possible based on the specifications offered by the manufacturer. For the EnCurrent 25kW turbine, the tip of the rotor blades is placed 0.59m below the free surface and for the 125kW turbine at 1.35m. For the Wanapum downstream micro-site, the Tocardo T-50 is placed 0.75m below the free surface, and for the Tocardo T-150 the clearance is set at 1.50m. For the Priest Rapids downstream micro-site, the placement of the EnCurrent 25kW is kept at 0.59m below the free surface, but the clearance of the T-50 is reduced to 0.30m due to limiting depth. At the powerhouses, for all except the EnCurrent turbines, the turbines are assumed to be placed such that at a nominal river discharge, the hub is aligned with the peak jet velocity. For the Wanapum dam, this corresponds to a hub placement 5m below the free surface and for the Priest Rapids dam it corresponds to 4m. For the EnCurrent devices, the generator limits how far below the free surface the turbines sit. They are assumed to be tilted to the maximum possible to

best align them with the flow and not expose the blades on the downstream side. The 25kW low speed turbine is assumed to have a tilt of 5.7° and the 125kW a tilt of 10.3°.

The clearance for the bottom mounted scenarios is based on the free surface elevation at the 99% exceedance discharge. For the Wanapum downstream micro-site the highest point above the river bed is set at 8.6m, allowing for a 0.5m clearance with the free surface elevation of 9.1m predicted for this lower bounding discharge. This position offers 4m of bottom clearance for the largest turbine, the T-150, and more for the smaller device. For the downstream Priest Rapids site, it is inevitable that the rotors will be exposed during low discharge, so the clearance is based on the height above the bed. Deployments are assumed to be placed such that the tip of the blades is above 30% of the boundary layer at the 95% exceedance discharge, or 1.1m above the river bed. For the powerhouse vicinity, a minimum top clearance of 0.3m is set in relation to the 99% exceedance discharge. For the largest turbine, the bottom clearance near the Wanapum dam is close to 4.60m and near the Priest Rapids dam is 3.00m.

5.2 Downstream Sites

The optimal location for placement of a single device is chosen as the region within the site where a balance between highest specific discharge and depth is found. For the Wanapum downstream site, the region for the deployment is centered on the 50m mark from the right edge of the site and for the Priest Rapids site the region for deployment is centered on the 27.5m mark from the right edge of the site. As seen in section IV, this location coincides with the peak of the power density across the Wanapum site at the nominal discharge. The corresponding velocity profile at each river flow rate is constructed by using the average of the necessary parameters (u_*, z_o, Π, δ and h) taken over the profiles in a total lateral distance of 5m. Each one of these parameters is correlated to the total river discharge through empirical relations. Since only three values for the discharge are used, the correlation coefficient is equal to 1 for all of the fits. The correlations are assumed to be valid over the whole range of discharges used to calculate the probability of river discharge. Table 5.3

lists the relations as a function of the discharge used for each parameter at the two different sites. For the Wanapum downstream site the relation of the boundary layer and the depth is the same. The empirical equation for the boundary layer height in the Priest Rapids site is derived in terms of the percentage of the total depth occupied by the boundary layer. This value is then multiplied by the depth to calculate the height of the boundary layer.

Table 5.3 Empirical Correlations between Total River Discharge and Velocity Profile Parameters

Wanapum Site (All Q's are in kcms)	
u_* (m/s)	$0.0998 * Q^{.3894} - 0.1012$
Π	$3.3613 * Q^{-2.7255} - .4142$
δ (m)	$0.9871 * Q^{.6243} – 7.9222$
z_o (m)	$1.538e\text{-}06 * Q^2 + 5.5047e\text{-}07 * Q – 4.5848e\text{-}06$
Priest Rapids Site (All Q's are in kcms)	
u_* (m/s)	$0.0132 * Q^{.7651} - 0.0854$
Π	$-0.0003 * Q^{2.7984} - 0.2906$
h (m)	$3.13 * Q^{.4671} – 0.1660$
δ (m)	$(-0.0001*Q^{3.9068} + .8517) * h$
z_o (m)	$-5.0819e\text{-}08 * Q^2 + 2.7476e\text{-}06 * Q + 2.4077e\text{-}06$

Based on the characteristics of the site and of the devices being considered, either a floating or bottom mounted configuration (as viewed feasible in section IV) is used to determine the extractable power. Accordingly, the power density is calculated from the constructed velocity profile in the span of the water column where the device would intersect the flow and is averaged over the depth. This depth-averaged power density is assumed to act over the cross-sectional area of the rotor and the available power is determined based on the nominal efficiency of the device (see table 5.2). Finally, the probability distribution of the total river discharge is applied to the calculated extractable power in order to compute the average power generated in a year. Figure 5.1 shows the step by step process used to compute the average power generated in a year. Table 5.4

and table 5.5 list the results for the annual average power, energy generation, and capacity factor at each site, for the two different deployment configurations where possible.

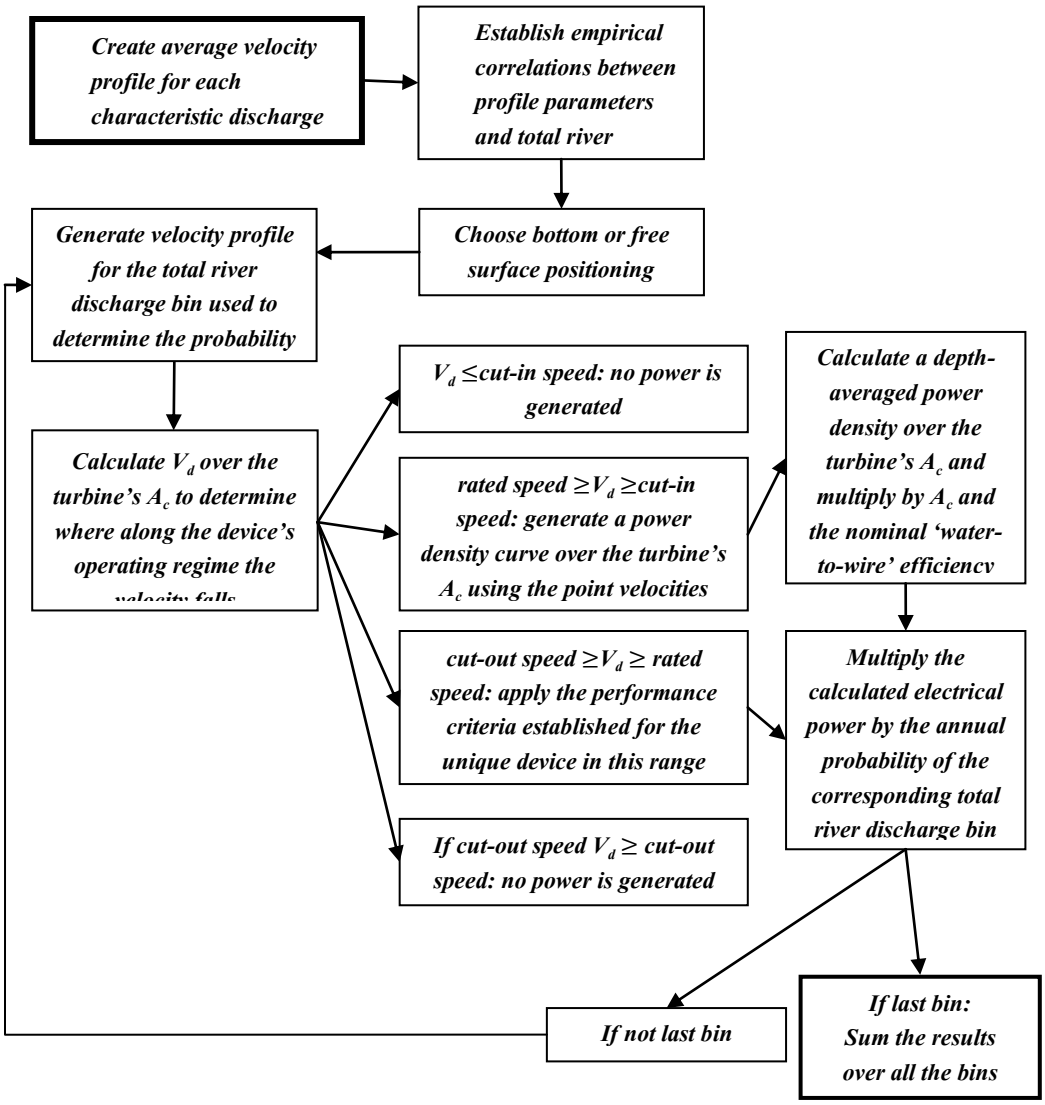

Figure 5.1 Depiction of the steps taken to compute the annual average power for the downstream sites. The process begins with the step found in the upper left hand corner and finishes with the step in the lower right hand corner.

Table 5.4 Results of Annual Average Power, Energy, and Capacity Factor at the Wanapum Site

Turbine	P_{gen} (kWa)	E (MWh/y)	Capacity Factor
New Energy's EnCurrent 25kW (low) 'floating'	8.0	69.7	0.32
New Energy's EnCurrent 125kW (low) 'floating'	33.9	297.0	0.27
Tocardo's T50-A 'floating'	7.7	67.3	0.15
Tocardo's T50-A 'bottom'	7.7	67.2	0.15
Tocardo's T150-A 'floating'	19.8	173.4	0.13
Tocardo's T150-A 'bottom'	19.6	172.1	0.13

Table 5.5 Results of Annual Average Power, Energy, and Capacity Factor at the Priest Rapids Site

Turbine	P_{gen} (kWa)	E (MWh/y)	Capacity Factor
New Energy's EnCurrent 25kW (high) 'floating'	5.1	44.8	0.20
Tocardo's T50-A 'floating'	30.7	269.2	0.61
Tocardo's T50-A 'bottom'	31.5	275.7	0.63

There is a big difference between the ranges in velocity expected at the two sites. The power density associated with the lower velocities present at the Wanapum site makes the low speed models offered by New Energy the superior option for this site. The larger EnCurrent turbine has a slight decrease in performance due to its position further below the free surface than the smaller turbine, intercepting slower velocities found closer to the river bed; this is also seen in the decrease in capacity factor for the Tocardo turbines. Nonetheless, the depth at the Wanapum site allows for sufficient clearance between the river bed and the blades to minimize the impact of the turbulence found in the lower ~35% of the water column. As observed in the results for the Tocardo units at

the Wanapum site, the change in the form deployment does severely impact the power generation expected.

Figure 5.2a shows the exceedance probability of the depth averaged streamwise velocity (V_d) calculated along the depth of the water column where the turbine intersects the flow for the low speed 25kW EnCurrent turbine at the Wanapum site. The cut-in, rated and cut-out speeds for the device are labeled. On an annual basis the device operates around 57% of the time. The higher cut-in speed of the EnCurrent turbine does not allow for operation of the device during 37.5% of the time. During about 5% of the time it is operating, the device operates at its rated power. Overall, given the range in power density expected at the Wanapum site, a positive economical prospect is difficult to foresee.

On the other hand, the data used to quantify the Priest Rapids site have velocities that are large, exceeding the optimal working range of the turbines. The velocity rating of 3 m/s of the EnCurrent high velocity model and the short working span in velocities above the rated value do not allow for much of a window (3 to 3.25 m/s) in which to expect this turbine to function. For this site, the T50-A turbine appears to be a good option, because its velocity range is fairly well matched to the river velocities. Figure 5.2b shows the exceedance probability of V_d for the T50-A turbine positioned in a bottom mount at the Priest Rapids site with the rated velocity and velocity at the minimum depth labeled. The device operates for over 95% of the time, with the depth limited operation during ~2% of the time. Although the turbine operates at non-optimal efficiencies for close to 35% of the time (when the river velocity exceeds the rated velocity of the turbine), the capacity factor is fairly high at 63%, implying the possibility of reasonable economics for the cost of electricity.

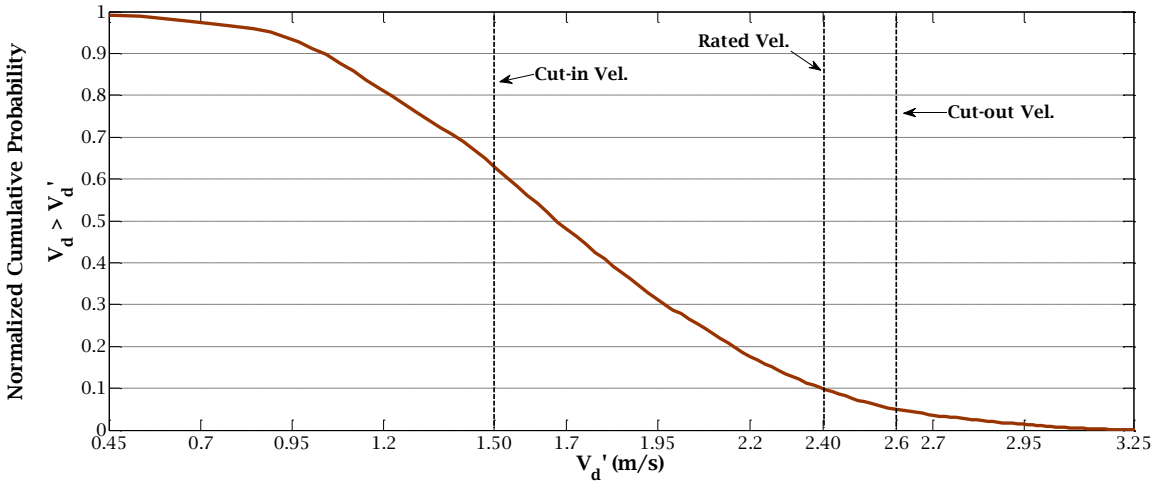

a)

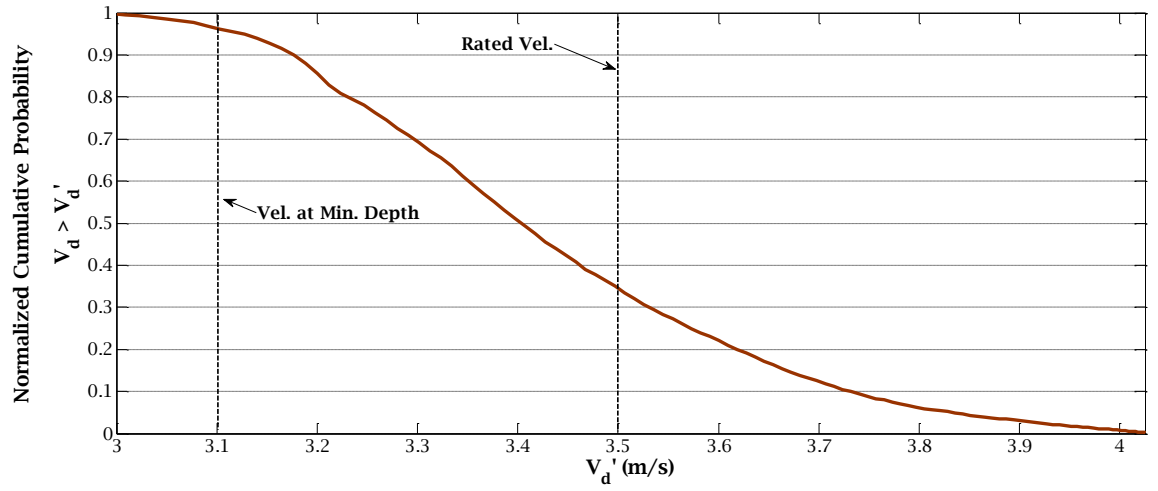

b)

Figure 5.2 Exceedance probability of the depth averaged streamwise velocity over the area of the turbines at the downstream micro-sites. Figure a) corresponds to the 25kW low speed EnCurrent turbine positioned in a floating deployment at the Wanapum site. Figure b) shows the results for the considered bottom deployment of the T50-A at the Priest Rapids downstream site.

5.3Powerhouse Vicinity

As a whole, the steps taken to determine the annual average power in the site near to the powerhouses are the same as presented in figure 5.1. The normalized velocity profiles presented in section 3.3 are used with empirical relations established between the total river discharge and the free-surface elevation in front of the powerhouse. The velocity decay for the profiles is applied to the average velocity at the draft tube outlet in order to determine the maximum velocity applicable to a normalized profile. The profile is used to compute the power density profile along the span of

the water column where the hydrokinetic turbine placement is envisioned. The frequency distribution of the area-averaged draft tube velocities for unit 6 and unit 4 at Wanapum and Priest Rapids, respectively, is used to calculate the available kinetic power. Where possible, the devices are aligned with the oncoming flow and if not, a correction for the component perpendicular to the rotor is included. Table 5.6 lists the free-surface correlations and tables 5.7 and 5.8 list the results for the annual average power, electricity generated, and capacity factor for each configuration. The velocity profile at the point of gradient inflection has an u_{max} equal to 1.09 times the maximum draft tube outlet velocity. This is considered a best case scenario.

A relatively large uncertainty exists in the power generation estimated for the powerhouse vicinity. As aforementioned, the behavior of the draft tube jets needs additional study and the shapes of the velocity profiles being used are those that most closely resemble published results and are only empirically matched. There is additional uncertainty associated with the velocities found in the draft tubes of the Priest Rapids powerhouse, which could be larger if in fact the outlet area is less than assumed.

Table 5.6 Empirical Relations between Free-Surface in Front of the Powerhouses And Total River Discharge

Wanapum Powerhouse Vicinity (All Q's are in kcms)	
Free-Surface Above Datum (m)	$0.3935 * Q^{.9816} + 148.8159$
Priest Rapids Powerhouse Vicinity (All Q's are in kcms)	
Free-Surface Above Datum (m)	$0.4466 * Q^{1.3091} + 122.5380$

Table 5.7 Results of Annual Average Power, Energy, and Capacity Factor in the Wanapum Powerhouse Vicinity with the 'Best Scenario' Velocity Profile

Turbine	P_{gen} (kWa)	E (MWh/y)	Capacity Factor
New Energy's EnCurrent 25kW (low) 'floating'	19.6	172.1	0.79
New Energy's EnCurrent 125kW (low) 'floating'	75.3	659.2	0.60
Tocardo's T50-A 'floating'	15.4	134.8	0.31
Tocardo's T50-A 'bottom'	10.2	89.6	0.20
Tocardo's T150-A 'floating'	37.4	327.7	0.25
Tocardo's T150-A 'bottom'	31.1	272.7	0.21

Table 5.8 Results of Annual Average Power, Energy, and Capacity Factor in the Priest Rapids Powerhouse Vicinity with the 'Best Scenario' Velocity Profile

Turbine	P_{gen} (kWa)	E (MWh/y)	Capacity Factor
New Energy's EnCurrent 25kW (low) 'floating'	9.9	86.9	0.40
New Energy's EnCurrent 125kW (low) 'floating'	53.1	465.0	0.425
Tocardo's T50-A 'floating'	13.1	114.7	0.26
Tocardo's T50-A 'bottom'	10.5	92.0	0.21
Tocardo's T150-A 'floating'	32.0	280.0	0.21
Tocardo's T150-A 'bottom'	31.0	271.9	0.21

As evident in the velocity profiles, the region of highest power density lies around the middle of the water column, with decay in velocity occurring in both up and down from the maximum point.

Being able to maintain a turbine centered on this peak by deploying from the free-surface clearly offers the highest capacity factor. For most of the floating deployments at both powerhouses the smaller devices outperform the larger ones. The larger devices (EnCurrent 125kW and T150-A) intersect a larger section of the flow, and therefore encounter regions of reduced velocity and power density. In the case of the EnCurrent turbines near the Priest Rapids powerhouse, both devices perform similarly, with the larger device having an increase of 2.5% in the capacity factor.

Under the assumptions used to perform the calculations, the vicinity of the Wanapum powerhouse offers a more optimal location for deployment of hydrokinetic devices than the downstream site. In figure 5.3 the exceedance probability of the mean velocities (V) calculated at the draft tube outlets of unit 6 of the Wanapum powerhouse and unit 4 of the Priest Rapids powerhouse are shown. It is observed that the velocity found at unit 6 of Wanapum exceeds the velocity calculated at unit 4 of the Priest Rapids powerhouse during 90% of the time. The difference in the expected velocities results in the difference between the two sites in the performance of the Tocardo turbines for free surface deployment. The range of velocities expected in the powerhouse vicinity means a low velocity turbine is going to work best, which is seen by comparing the capacity factors of the New Energy (rated at 2.4m/s) and the Tocardo (rated at 3.5m/s) devices.

Between the two powerhouses, the bed gradient is significantly steeper in the vicinity of the Priest Rapids powerhouse. The steep gradient coupled with the limitation that the gear box introduces for the positioning of the EnCurrent turbines, causes a decrease in performance of the devices. As stated in section 5.1, the angle up to which the turbines can be tilted in order to obtain an optimal alignment between the rotor blades and the oncoming flow is restricted. Therefore, the turbines could not be optimally aligned with the flow at the steeper bed gradient near the Priest Rapids powerhouse. The effect of obtaining better placement through a larger tilt angle is seen in the increase in capacity factor for the 125kW EnCurrent (10.3° instead of 5.7°).

If the outlet of the draft tubes in the Priest Rapids powerhouse is indeed smaller than considered, the flow speed can be expected to range much closer to the rated velocity of the Tocardo units. These turbines do not present a hindrance in their positioning for best alignment with the flow and could be expected to perform better than indicated in tables 5.7 and 5.8.

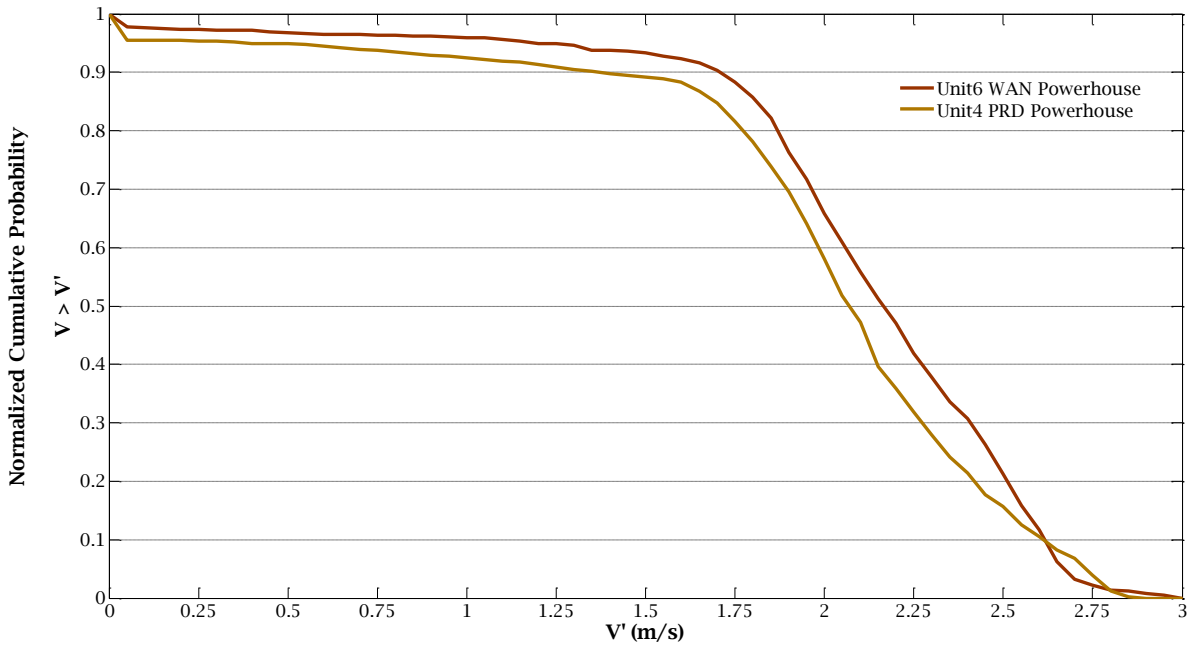

Figure 5.3 Exceedance probability of mean draft tube outlet velocity for unit 6 and unit 4 at the Wanapum and Priest Rapids powerhouses, respectively.

VI - Cost Estimate

At such an early stage of technology development, the costs associated with the deployment and long term functionality of a hydrokinetic turbine or power farm are uncertain. Section I lists the more prominent manufacturers of river in-stream turbines and as noted, only two can currently provide a tested, functioning device.

Table 6.1 lists the kinetic turbines currently available from New Energy with the corresponding prices. The pricing corresponds to the retail value found at ABS Alaskan Inc., a reseller for New Energy Corp. Inc. The price for the 25kW device is an approximation given by Jim Norman, president of ABS Alaskan Inc. [94]. This report estimates the nominal price at $5300 per rated kW.

Table 6.1 Pricing of Available Hydrokinetic Turbines

Manufacturer	Turbine	Rating	Price (per rated kW)
New Energy Corp. Inc.	**EnCurrent**	5kW	$5,600
		5kW (low speed)	$5,950
		10kW	$5,200
		25kW	~$5,400*

The prices listed above include the power electronics, i.e. the inverter and rectifier, necessary to provide an end product ready to be tied into a grid. Additional costs are going to be accrued in the mounting and anchoring system, electrical cable extending from the turbine to the connection point into the grid, a transformer in the case a voltage step-up is required, the civil work for final assembly of the components, labor costs, and licensing and permitting fees.

At this point in time a detailed breakdown of the cost for the remaining components would be speculative without a finalized design and coordinated deployment procedure. Using as an example the deployment of the 25kW EnCurrent turbine near the community of Eagle, AK, a price range for a floating aluminum structure without an anchor is quoted between $40,000 and $60,000, by Jim Norman [94]. ABS Alaskan, Inc. manufactured the pontoon being utilized at the Eagle site for the

turbine deployment. Based on this price, the cost for the system and the float falls between $7,000-$7,800/rated kW. According to a New Energy project pricing and payback brochure [95], the additional installation cost for the turbine system and float is $20,000 fixed, plus $1,000 per installed kW. This fixed amount is assumed to be for the mounting arms and plates that attach the turbine to a floatation device. Using this estimate brings the installed price of the Eagle deployment to a range of $8,800 to $9,600 per rated kW.

For this case in Eagle, AK, it is emphasized that the floating pontoon was built with the intention of acting dually as a work station and a buoyant support for the turbine system, hence having a larger weight capacity and more expense. This includes design for the severity of the environment expected at this site and the necessity for a very robust system able to withstand debris such as tree trunks that can scale in size to the depth of the river. Updates on the experience of this deployment have shown that overcoming the problem associated with debris is the key element holding back success of the installation and this is going to continue adding to the cost associated with the project [96].

A conservative estimate for the complete hook-up of a stand-alone deployment is set at the equivalent of the price of the turbine. Using the range of prices known and based on this installation budget, a complete pilot project falls in a price range between $6,000 and $11,900 per rated kW installed, with the price varying inversely to size, and an average cost of $10,050 per rated kW.

The higher overall investment for a single hydrokinetic pilot project will have costs that accumulate from site testing and infrastructure and deployment coordination. The experience gained in the fine tuning of a single device is intended to establish a more efficient use of time, machinery and resource and turn those costs into a shared expense among multiple units.

Foreseen operational and maintenance (O&M) costs are associated with damage incurred by the turbine, mounting structure, the electrical cables and supply system, and replacement of lubricating or sealing fluids. In general, the turbines do not have many serviceable parts and should not require much labor to maintain. Scenarios prone to a higher frequency of maintenance and more susceptible to damage are expected to occur for deployments in river reaches where the appearance of large vegetation or ice debris and significant sediment transport are typical. Comparing among the handful of deployments that have been recorded, the positioning of turbines in the tailrace of Columbia River dams should significantly lessen the burden of O&M due to damage caused by debris and sediment. In the study done by EPRI [9] on sites in Alaska, O&M costs ranged between 2.45-7.08% depending on the size and location of the deployment. Considering all of the options studied, an average O&M of 4.77% is obtained. In comparison, O&M costs for large and small conventional hydro is reported by the International Energy Agency (IEA) [97] to fall between 1.5-2.5% of the capital investment.

In addition to the benefit that the dam offers in containing any debris found in the flow, the PUD is seen as having an advantage in accessibility to the necessary electrical infrastructure and as having experience in the permitting and licensing procedures. It is difficult to assess by how much the various attributes of a tailrace deployment will influence the project cost, but it points towards a favoring of the lower side of the range. Because of the variability and scarcity of the projects being launched, a fairly broad spectrum in cost is expected. The sensitivity to site characteristics is illustrated by the quoted price of the floating barge. Based on a price listing provided to the Alaska Power and Telephone Company by U-Fab Boats in 2010, an approximate price per kg of weight capacity for aluminum pontoons is $3/kg [96]. Using this value with the price range of $40,000-$60,000 for a working barge, and the reported weight of the 25kW low speed EnCurrent turbine of 2665kg, the barge would be rated between five and seven and half times the weight of the rotor and

generator. If a reduction of these weight requirements by a factor of two was possible, it would bring the cost of the project down by 10-12.5% based on the New Energy installation estimates.

At $6,000-$11,900 per rated kW installed, a pilot scale hydrokinetic project fits close within the upper range of $7,500 and $10,000 per installed kW, given by the IEA [97], for small (1-10 MW) and micro ($\leq$1 MW) conventional hydro installations, respectively. If deployment for a kinetic turbine can be achieved near the lower end of the cost scale at a site that offers a capacity factor above that of the small hydro plants, typically 45-50%, it would place the technology within a competitive range for the cost of energy for small hydro developments. An analysis for determining this cost of energy requires details for project financing that are inherent to the way Grant County PUD conducts business and falls beyond the scope of this assessment.

VII - Concluding Remarks and Recommendations

The tailrace of the Wanapum and Priest Rapids dams have been analyzed in order to determine the hydrokinetic resource available for a feasible introduction of an energy converting hydrokinetic turbine. Data obtained directly from Grant County PUD, IIHR and DART have been used for the study. Four different hydrokinetic turbines that are available or are supposed to become available in the near future are considered as the viable technology to introduce in the tailrace waters. The devices cover a range of turbine designs and include a horizontal axis turbine with two blades, a shrouded horizontal axis turbine with seven blades and a diffuser on the downstream end, a vertical axis turbine with four blades, and a cross-flow horizontal axis turbine with four blades.

In each tailrace, two sites are chosen for the study, with the powerhouse vicinity of each dam being one of those. Thus, in all, four sites are treated. At approximately 1400m downstream from the left embankment of the Wanapum dam, the region near to a constriction that occurs in the river is chosen because it is observed to help overcome large spatial variations in the flow patterns that can occur during times of spill, either for fish passage or by the main spillway. Computational fluid dynamic (CFD) simulations requested from IIHR show that close to 550m downstream from the Priest Rapids powerhouse, as the width of the river decreases, the river reach has a region that develops high velocities that fall within the rated velocities of most turbines being manufactured, presenting a site with high kinetic power density.

For these downstream sites, average power extraction and energy generation has been calculated using the probability distribution of river discharge along with empirical correlations between the various parameters necessary to construct a representative velocity profile for a given discharge. The parameters for a low, median, and high discharge have been calculated by fitting data extracted from the IHR CFD simulations and averaged over the specific region within the micro-site where a pilot scale deployment is viewed as being best positioned. The performance and placement of each

turbine is examined according to information available from the manufacturers and based on the characteristics of the sites.

At the site downstream from the Wanapum dam, because of its relatively low velocities, the EnCurrent turbines that are designed to generate high torque at low speeds are favored. These turbines have a generator and gear box intended to remain above the water line and have been mounted on a floating structure for determining their performance. For the 25kW EnCurrent turbine, positioning of the rotor blades in the water below the floating platform is based on guidelines available from the manufacturer; for the 125kW turbine, positioning is based on extrapolation of the guidelines. The capacity factor for the 25kW turbine is calculated to be 32% and for the 125kW it is slightly lower at 27%. The difference between the two is due to the larger size of the rotor intercepting slower velocities deeper in the water column.

The Priest Rapids site offers the potential for placement in a region with high kinetic power density. However, the velocities at this point exceed the rated velocities of the turbines over 50% of the time. The limited range in which the EnCurrent turbines can function above the rated speed only allow the device to reach a capacity factor of 20%. On the other hand, the Tocardo T-50 turbine still performs at velocities close to 40% higher than its rated power velocity, though its extraction efficiency is hindered. Considering a bottom mounting, a capacity factor of 63% is calculated for the Tocardo T-50.

In the vicinity of the powerhouse, a generalized velocity profile has been constructed based on CFD simulations pertaining to the Wanapum tailrace that depict vertical velocity distributions similar to what has been reported in the literature for wall-bounded jets. This region offers a relatively high degree of uncertainty that arises from the complexity of the flow expected to come from within the draft tubes. Area-averaged velocities have been computed for the outlet of each draft tube based on the area of the Wanapum powerhouse draft tubes. The discharge through each

Kaplan turbine is assumed to be directly proportional to the power being generated and is calculated using the total discharge going through the powerhouse and the proportion of electricity being generated by each unit. As reported in the literature, the jets coming from the draft tube experience decay in the maximum velocity magnitude as a function of the distance from the outlet. However, the positive slope of the river bed and the expansion of the jet up to the free surface, might lead to an increase in velocity just downstream of the powerhouses. This increase is observed to occur to some extent in all of the CFD simulations and could be occurring because of conservation of mass. If the jet expands up to the free surface before the change in bed gradient is reached, the decrease in cross-sectional area of the flow due to the rising river bed reaccelerates the jet along a brief distance before it continues to decay and mix with the surrounding jets.

The slower velocities expected in the vicinity of the powerhouse favor the low speed turbines manufactured by New Energy. Using the velocities calculated for the outlet of unit 6 of the Wanapum powerhouse and applying a velocity factor of 1.09, the capacity factor of the 25kW EnCurrent turbine is calculated to be 79%, and a value of 60% is computed for the 125kW turbine. For the Priest Rapids powerhouse, velocities for unit 4 are used, providing a capacity factor of the 25kW turbine of 40% and of 42.5% for the 125kW turbine. In general the velocities calculated at the outlet of unit 4 of the Priest Rapids powerhouse are lower than those calculated for unit 6 at the Wanapum dam and the positioning of the turbine did not allow for optimal capture of the oncoming flow because of the steeper positive bed slope found in front of the Priest Rapids powerhouse. The rest of the devices performed comparatively, with an average capacity factor of 25%.

Keeping in mind the early stages of the technology and the limited experience that exist in bringing together a functioning deployment, costs associated with setting up a pilot scale project fall within a range. Based on the limited information available, the total cost for setting up a stand-alone unit is expected to range from $6,000 to $11,900 per rated kW installed. A detailed breakdown of the cost and of the financing for a project was not considered in this study.

The way things stand currently with the technology, it is recommended that the stretch of river downstream from Priest Rapids running from about 500m to 800m receive further attention, since this area appears to have an abundant source of kinetic energy. Based on the bathymetry, a slower flow can be expected to occur as the river bed evens out. The larger cross-sectional area that results from the wider section of depth should cause lower velocities than those observed at the chosen cross-section and should improve on the performance of the turbines by improved matching of river velocity with rated turbine velocity.

For the powerhouse vicinity, the Priest Rapids powerhouse is recommended for further study, since the cross-sectional area of the draft tubes may be smaller than that assumed in this study. As pointed out in section II, the combined cross-sectional area of the three bays for a Wanapum draft tube is about 170.5m^2 with an expansion ratio for the rectangular diffuser of 1.65. In the case of the Priest Rapids draft tubes, if a similar expansion ratio exist then the combined area would be 116.2m^2. This reduction in area of close to 30% would result in a significant increase in the average velocity of the flow leaving the draft tubes. For both dams, it is recommended that the general vicinity to the powerhouses be investigated more carefully in order to gain a better understanding on the decay of the jets, the interaction between the jets, and the turbulence levels expected.

As technology improves and manufacturers start to offer a wider selection of turbines optimized to function in different ranges of velocity and depth, the vicinity of the Wanapum powerhouse could be a reliable source of kinetic power, offering velocities close to the 2m/s range in front of certain units. Further downstream, it appears that the stretch of the thalweg beginning about 500m from the left embankment could have better velocities than those observed at the studied site. However, the behavior of smolt going through the fish bypass and being directed into this part of the river by the fast jet emanating from the structure has to be considered. If additional consideration of this stretch is taken, it would require an analysis of the resulting velocity profiles since the presence of the surface jet is expected to cause a variation in the distribution of velocities in the water column

when the bypass is operational. Additionally, the effects of having all three hydraulic structures operating simultaneously needs to be better understood, as well as the sensitivity of the average power generated by a commercially sized array of turbines on the different conditions.

References

[**1**] Department of Ecology, State of Washington. *Washington Rivers*, 1999. [Online] Available from: http://www.ecy.wa.gov/services/gis/data/image.asp?name=rivers [Accessed 15 October 2010]

[**2**] Anderson, J.J. *Decadal climate cycle and declining Columbia River salmon,* 1997. [Online] Available from: http://www.cbr.washington.edu/papers/jim/victoria.html [Accessed 19 September 2010]

[**3**] Wang, L., Infante, D., Lyons, J., Stewart, J. and Cooper, A. Effects of dams in river networks on fish assemblages in non-impoundment sections of rivers in Michigan and Wisconsin, USA, *River. Res. Applic.,* 2010. [Online] Available from: http://www.interscience.wiley.com [Accessed 19 September 2010] doi:10.1002/rra.1356.

[**4**] Haas, T.C., Blum, M.J. and Heins, D.C. Morphological responses of a stream fish to water impoundment, *Biology Letters,* 2010. [Online] Available from: http://rsbl.royalsocietypublishing.org [Accessed 19 September 2010] doi:10.1098/rsbl.2010.0401.

[**5**] *Assessment of waterpower potential and development needs*. EPRI, Palo Alto, CA: 2007. 1014762.

[**6**] Musial, W. *Status of wave and tidal power technologies for the United States*. NREL Technical Report *NREL/TP-500-43240*, August 2008.

[**7**] Bedard, R., Previsic, M., Hagerman, G., Polagye, B., Musial, W., Klure, J. et al. North American ocean energy status-March 2007. In *Proc. EWTEC 2007*, Porto, Portugal, 11-14th September 2007. [Online] Available from: http://oceanenergy.epri.com/attachments/ocean/reports/7th_EWTEC_Paper_FINAL_071707.pdf [Accessed 14 January 2010]

[**8**] Bedard, R.J., Previsic, M. and Polagye, B.L. *Marine energy: how much development potential is there?* 2009. [Online] Available from: http://www.renewableenergyworld.com/rea/news/article/2009/04/marine-energy-how-much-development-potential-is-yhere [Accessed 15 February 2011]

[9] The National Academies. *Current Projects; Project Title: Marine and Hydrokinetic Energy Technology Assessment,* 2010. [Online] Available from: http://www8.nationalacademies.org/cp/projectview.aspx?key=49272 [Accessed 5 June 2011]

[**10**] Previsic, M., Bedard, R. and Polagye, B. *System level design, performance, cost and economic assessment – Alaska river in-stream power plants*. EPRI Report *EPRI-RP 006 Alaska,* October 2008.

[**11**] Sturm, T.W. *Open Channel Hydraulics, 2nd ed*. Boston: McGraw-Hill, Inc., 2009.

[**12**] Sinha, S.K., Sotiropoulos, F. and Odgaard, A.J. Three-dimensional numerical model for flow through natural rivers, *J. Hydraulic Eng.,* 1998, **124**(1), pp. 13-24.

[**13**] Kundu, P.K. and Cohen, I.M. *Fluid Mechanics, 4th ed.* Cleveland: Academic Press, 2007.

[**14**] Linsley, R.K., Franzini, J.B., Freyberg, D.L. and Tchobanoglous, G. *Water-Resources Engineering, 4th ed.* USA: McGraw-Hill, 1992.

[**15**] Twidell, J. and Weir, T. *Renewable Energy Resources, 2nd ed.* London; New York, 2006.

[**16**] Vosbeek, P. (Founding Partner, Real New Energy, LLC). *RE: Tocardo Turbines.* Personal email communication with Arango, M., June 2011.

[**17**] Tocardo International BV. *Tocardo T50-A product brochure*, 2010. [Online] Available from: http://www.tocardo.com/cms/files/PDF-downloads/tocardo-t50-a-product-brochure-v1-1d-compact.pdf [Accessed 14 November 2010]

[**18**] Worthington, M. (Director of Project Development, ORPC Alaska, LLC). *RE: RivGen™ conceptual design.* Personal email and telephone communication with Arango, M., August 2010.

[**19**] Ocean Renewable Power Company. *ORPC Projects*, 2011 [Online] Available from: http://www.oceanrenewablepower.com/home.htm [Accessed 25 May 2010]

[**20**] New Energy Corporation. *Product datasheets*, 2009. [Online] Available from: http://www.newenergycorp.ca/Resources/DocumentLibrary/ProductDatasheets/tabid/87/Default.aspx [Accessed 10 March 2010]

[**21**] Hydro Green Energy. *Product specification sheet*, [no date]. [Online] Available from: http://hgenergy.com/Product%20Spec%20Sheet.pdf [Accessed 14 January 2010]

[**22**] Hydro Green Energy. *Hydro Green Energy Hastings, MN Photographs*, [no date]. [Online] Available from: http://www.hgenergy.com/hastingsinstallation.html [Accessed 14 January 2010]

[**23**] Free Flow Power Corporation. *Technology*, 2010. [Online] Available from: http://www.free-flow-power.com/Technology.html [Accessed 14 April 2010]

[**24**] Free Flow Power Corporation. *2nd Quarterly report under P-12829, et al.* FERC Submittal *20100802-5099*, 2 August 2010. [Online] Available from: http://elibrary.ferc.gov [Accessed 14 September 2010]

[**25**] Lovelace, E. (Executive Vice President of Engineering, FFP). *RE: SmarTurbine™.* Personal telephone communication with Arango, M., October 2010.

[**26**] Tocardo International BV. *Tocardo T150-A product brochure*, 2010. [Online] Available from: http://www.tocardo.com/cms/files/PDF-downloads/tocardo-t150-a-product-brochure-v1-0a-compact.pdf [Accessed 14 November 2010]

[**27**] Tocardo International BV. *Home page*, 2010. [Online] Available from: http://www.tocardo.com/ [Accessed 14 November 2010]

[**28**] Anderson, R.M., Unwin, S.D. and Van Cleve, F.B. *Identification and prioritization of analysis cases for marine and hydrokinetic energy risk screening: Environmental effects of marine and hydrokinetic energy – Fiscal year 2010*. PNNL Report *PNNL-19535*, June 2010.

[**29**] Department of Energy. *Hydropower Awards – 9/15/09*, 2009. [Online] Available from: http://www.energy.gov/recovery/8011.htm [Accessed 18 April 2011]

[**30**] *Quarterly technical progress report no. 2*: *Assessment of the environmental effects of hydrokinetic turbines on fish – Desktop and laboratory flume studies*. EPRI Technical Progress Report, 21 July 2010. (Limited distribution: obtained through personal communication between Worthington, M. and Arango, M., August 2010)

[**31**] *An estimation of survival and injury of fish passed through the Hydro Green energy hydrokinetic system, and a characterization of fish entrainment potential at the Mississippi Lock and Dam No. 2 hydroelectric project (P-4306) Hastings, Minnesota*. Normandeau Associates Final Report *Normandeau Associates Project No. 21288.000*, December 2009. [Online] Available from: http://www.hgenergy.com/Hastings%20Agencies%20Review%20Draft%2012-21-09.pdf [Accessed 8 January 2010]

[**32**] Thielmann, J. *Power Extraction from Irrigation Laterals and Canals in the Columbia Basin Project.* MSc Thesis, WA: University of Washington, 2009.

[**33**] Lalande, E. and Leijon, M. In-stream energy converters in a river – Effects on upstream hydropower station, *Renewable Energy*, 2011, 36(1), pp. 399-404.

[**34**] Toniolo, H., Duvoy, P., Vanlesberg, S. and Johnson, J.B. Modeling and field measurements in support of the hydrokinetic resource assessment for the Tanana river at Nenana, Alaska, *Proc. Inst. Mech. Eng, Part A: J. Power and Energy,* 2010, 224 *,* pp. 1127-1139.

[**35**] Worthington, M. *Fourth 6-month progress report of ORPC Alaska, LLC for Nenana project under P-13233*. FERC Submittal *20101001-5013*, 1 October 2010. [Online] Available from: http://elibrary.ferc.gov [Accessed 14 October 2010]

[**36**] New Energy Corporation. *White Papers*, 2009. [Online] Available from: http://www.newenergycorp.ca/Resources/DocumentLibrary/WhitePapers/tabid/84/Default.aspx [Accessed 10 March 2010]

[**37**] *Summary of activities, 7/1/1999-6/30/2000*. Iowa Institute of Hydraulic Research, [no date]. [Online] Available from: http://www.iihr.uiowa.edu/search/ [Accessed 18 April 2011]

[**38**] IIHR-Hydroscience and Engineering. *Fish Passage*, 2011. [Online] http://www.iihr.uiowa.edu/research/fish-passage/ [Accessed 18 April 2011]

[**39**] Public Utility District No.2 of Grant Country, WA. *Priest Rapids Project – FERC P-2114: Downstream passage alternatives action plan*. FERC Submittal, May 2009. [Online] Available from: http://www.gcpud.org/prcc/pdfs/PRPAction%20Plan_LA%20401.pdf [Accessed 21 February 2010]

[**40**] Sinha, S.K., Weber, L.J. and Odgaard, A.J. *Hydraulic model studies for fish diversion at Wanapum/Priest Rapids development, Part IX: Identification of a fish bypass outfall location for Wanapum Dam tailrace*. IIHR Limited Distribution Report No. 252, November 1996.

[**41**] Weber, L.J. and Politano, M. *Subject: Flow pattern in the tailraces of the Priest Rapids and Wanapum Dams*. IIHR Letter Report, 19 February 2010.

[**42**] Politano, M., Carrica, P. and Weber, L. A multiphase model for the hydrodynamics and total dissolved gas in tailraces, *Int. J. of Multiphase Flow,* 2009, **35**(11), pp. 1036-1050.

[**43**] Griffith, A.R., Rutherford, J.H., Alavi, A., Moore, D.D. and Groeneveld, J. Stability review of the Wanapum spillway using CFD analysis, *Canadian Dam Association Bulletin*, 2007, **18**(4), pp. 16-26.

[**44**] Noteboom, R. (Manager of Transmission Services, GCPUD) and Knitter, K. (Manager of Resource Planning GCPUD). *FW: Powerhouse and spillway operations* and *FW: Unit Specific Powerhouse data for PRP 07-09*. Personal emails sent to Arango, M., 19 April 2010 and 10 May 2010.

[**45**] FERC *Order Issuing New License Project No. 2114-116 _Priest Rapids Hydroelectric Project*, 17 April 2008. [Online] Available from: http://www.gcpud.org/pudDocuments/naturalResourcesDocs/h1.pdf [Accessed 4 January 2010]

[**46**] Public Utility District No.2 of Grant Country, WA. *Digital Media: Photos*, 2010. [Online] Available from: http://www.gcpud.org/yourPud/newsRoom/digitalMedia.html [Accessed 30 March 2011]

[**47**] Columbia River DART (Data Access in Real Time). *River Environment Graphics and Text*, 2011. [Online] Available from: http://www.cbr.washington.edu/dart/river.html [Accessed February 2010]

[**48**] Xu, J., Maxey, M.R. and Karniadakis, G.E. Numerical simulation of turbulent drag reduction using micro-bubbles, *J. Fluid Mech.*, 2002, **468**, pp. 271-281.

[**49**] *Fishery Operations Plan-Priest Rapids Hydroelectric Project (P-2114).* Public Utility District No. 2 of Grant Country, WA, February 2010. [Online] Available from: http://www.gcpud.org/prcc/supportingdocs/LA-404%20PRP%20Fishery%20Operations%20Plan.pdf [Accessed 4 January 2010]

[**50**] Knitter, K. (Manager of Resource Planning GCPUD), Jeske, D. (Project Manager and Hydroelectric Engineer GCPUD) and Strickler,B. (Project Engineer GCPUD). *RE: Question for Keith/WAN_PR dam*. Personal email to: Arango, M., 12 November 2010.

[**51**] Dauble, D.D., Deng, Z.D., Richmond, M.C., Moursund, R.A., Carlson, T.J., Rakowski, C.L. and Duncan, J.P. *Biological assessment of the advanced turbine design at Wanapum Dam, 2005.* PNNL Report *PNNL-16682*, August 2007.

[**52**] Holden, A.P. and James, C.S. Boundary shear distribution on flood plains, *J. Hydraul. Res.,* 1989, **27**(1), pp. 75-89.

[**53**] Knight, D.W. and Hamed, M.E. Boundary shear in symmetrical compound channels, *J. Hydraul. Eng.,* 1984, **110**(10), pp. 1412-1430.

[**54**] Knight, D.W. and Demetriou J.D. Flood plain and main channel flow interaction, *J. Hydraul. Eng.*, 1983, **109**(8), pp. 1073-1092.

[**55**] Jing, H., Li., C., Guo, Y. and Xu., W. Numerical simulation of turbulent flows in trapezoidal meandering compound open channels, *Int. J. Numer. Meth. Fluids*, 2011, **65**(9), pp. 1071-1083.

[**56**] Guo, J., Julien, P.Y. and Meroney, R.N. Modified log-wake law for zero-pressure-gradient turbulent boundary layers, *J. Hydraul. Res.,* 2005, **43**(4), pp. 421-430.

[**57**] Guo, J. and Julien, P.Y. Application of the modified log-wake law in open-channels, *J. Appl. Fluid Mech.,* 2008, **1**(2), pp. 17-23.

[**58**] Castillo, L. *Similarity Analysis of Turbulent Boundary Layers*. PhD Thesis, NY: State University of New York (Buffalo), 1997.

[**59**] Schlichting, H. *Boundary Layer Theory, 7^{th} ed.* New York: McGraw-Hill, 1979.

[**60**] Onitsuka, K., Akiyama, J. and Matsuoka, S. Prediction of velocity profiles and Reynolds stress distribution in turbulent open-channel flow with adverse pressure gradient, *J. Hydraul. Res.,* 2009, **47**(1), pp. 58-65.

[**61**] Yang, S., Xu, W. and Yu, G. Velocity distribution in a gradually accelerating free surface flow, *Adv. Water Resour.*, 2006, **29**(12), pp.1969-1980.

[**62**] Castro-Orgaz, O. Velocity profile and flow resistance models for developing chute flow, *J. Hydraul. Eng.*, 2010, **136**(7), pp. 447-452.

[**63**] Mikhailov, V.V. Universal velocity defect law for the turbulent boundary layer, *Fluid Dynam.*, 2005, **40**(2), pp. 245-255.

[**64**] Smits, A.J., McKeon, B.J. and Marusic, I. High-Reynolds number wall turbulence, *Annu. Rev. Fluid Mech.*, 2011, **43**, pp. 353-375.

[**65**] Nezu, I. and Nakagawa, H. Turbulence measurements in unsteady free-surface flows, *Flow Meas. Intrum.,* 1995, **6**(1), pp. 49-59.

[**66**] Khatua, K.K., Patra, K.C. and Jha, R. Apparent shear stress in a compound channel. Presented in the *Hydro-09 Nat. Conf. of Hydraul., Water Resour., Coast. and Environ. Eng.,* CWPRS, PUNE, India, December 2009. [Online] Available from: http://dspace.nitrkl.ac.in:8080/dspace/bitstream/2080/1095/1/APPARENT+SHEAR+STRESS+IN+A+COMPOUND+CHANNEL.pdf [Accessed 20 July 2010]

[**67**] Zarrati, A.R., Jin, Y.C. and Karimpour, S. Semianalytical model for shear stress distribution in simple and compound open channels, *J. Hydraul. Eng.*, 2008, **134**(2), pp. 205-215.

[**68**] Rhodes, D.G. Estimation of shear-layer widths in a compound channel flow. In *Proc. 28th IAHR Congress*, Graz, Austria, 22-27 August, 1999. [Online] Available from: http://www.iahr.org/membersonly/grazproceedings99/pdf/E020.pdf [Accessed 21 July 2010]

[**69**] Tominaga, A. and Nezu, I. Turbulent structure in compound open-channel flows, *J. Hydraul. Eng.,* 1991, **117**(1), pp. 21-41.

[**70**] Cervantes, M.J., Andersson, U. and Lövgren, H.M. Turbine-99 unsteady simulations-Validation, *IOP Conf. Series: Earth and Environment Science*, 2010, **12**(1), doi: 10.1088/1755-1315/12/1/012014.

[**71**] Lai, Y.G., Weber, L.J. and Patel, V.C. Nonhydrostatic three-dimensional method for hydraulic flow simulation; II: Validation and application, *J. Hydraul. Eng.,* 2003, **129**(3), pp. 206-214.

[**72**] Duquesne, P., Iliescu, M., Fraser, R., Deschênes, C. and Ciocan, G.D. Monitoring of velocity and pressure fields within an axial turbine, *IOP Conf. Series: Earth and Environment Science*, 2010, **12**(1), doi: 10.1088/1755-1315/12/1/012042.

[**73**] Deschênes, C., Ciocan, G.D., Henau, V. D., Flemming, F., Huang, J., Koller, M. et al. General overview of the AxialT project: a partnership for low head turbine developments, *IOP Conf. Series: Earth and Environment Science*, 2010, **12**(1), doi: 10.1088/1755-1315/12/1/012043.

[**74**] Henau, V.D., Payette, F.A., Sabourin, M., Deschênes, C., Gagnon, J.M. and Gouin, P. Computational study of a low head draft tube and validation with experimental data, *IOP Conf. Series: Earth and Environment Science*, 2010, **12**(1), doi: 10.1088/1755-1315/12/1/012084.

[**75**] Gouin, P., Deschênes, C., Iliescu, M. and Ciocan, G.D. Experimental investigation of draft tube flow in an axial turbine by Laser Doppler Velocimetry. Presented in the *3rd IAHR Int. Meeting of the Workgroup on Cavitation and Dynam. Problems in Hydraul. Machinery and Syst.*, Brno, Czech Republic, 14-16th October 2009. [Online] Available from: http://lamh.gmc.ulaval.ca/fileadmin/docs/Publications_Recentes/PHILIPPE_GOUIN_final_paper.pdf [Accessed 4 August 2010]

[**76**] Gagnon, J.M., Iliescu, M., Ciocan, G.D. and Deschênes, C. Experimental investigation of runner outlet flow in axial turbine with LDV and stereoscopic PIV. Presented in the *24th IAHR*

Symp.on Hydraulic Machinery and Systems, Foz do Iguassu, Brazil, 27th-31st October 2008. [Online] Available from: http://lamh.gmc.ulaval.ca/fileadmin/docs/Publications_Recentes/IAHR_2008_49.pdf [Accessed 4 August 2010]

[**77**] Gagnon, J.M. and Deschênes, C. Numerical simulation with flow feature extraction of a propeller turbine unsteady rotor-stator interaction. Presented in the *13th Int. Conf. Computational Methods Experimental Measure.*, Prague, Czech Republic, 2007. [Online] Available from: http://lamh.gmc.ulaval.ca/fileadmin/docs/Publications_Recentes/Numerical_Simulation_with_Flow_Feature_Extraction_of_a_Propeller_Turbine.pdf [Accessed 4 August 2010]

[**78**] Sudo, K., Sumida, M. and Hibara, H. Experimental investigation on turbulent flow in a circular-sectioned 90-degree bend, *Experiments in Fluids*, 1998, 25(1), pp. 42-49.

[**79**] Paik, J., Sotiropoulos, F. and Sale, J. Numerical simulation of swirling flow in complex hydroturbine draft tube using unsteady statistical turbulence models, *J. Hydraul. Eng.*, 2005, **131**(6), pp. 441-456.

[**80**] Spedding, P.L., Benard, E. and McNally, G.M. Fluid flow through 90 degree bends, *Dev. Chem. Eng. Mineral Process*, 2004, **12**(1-2), pp. 107-128.

[**81**] Tandiono, Winoto, S.H. and Shah, D.A. Visualizing shear stress in Görtler vortex flow, *J. Visualization*, 2009, **12**(3), pp. 195-202.

[**82**] Saric, W.S. Görtler vortices, *Annu. Rev. Fluid Mech.*, 1994, **26**, pp. 379-409.

[**83**] Hall, P. Görtler vortices in growing boundary layers: The leading edge receptivity problem, linear growth and the nonlinear breakdown stage, *Mathematika*, 1990, **37**(2), pp. 151-189.

[**84**] Zhang, R., Mao, F. and Wu, J. Characteristics and control of the draft-tube flow in part-load Francis turbine, *J. Fluids Eng.,* 2009, **131**(2), doi:10.1115/1.3002318.

[**85**] Cook, C.B., Dibrani, B., Serkowski, J.A., Richmond, M.C., Titzler, P.S. and Dennis, G.W. *Acoustic Doppler Current Profile measurements in the tailrace of John Day Dam.* PNNL Report *PNNL-15627*, January 2006.

[**86**] Barenblatt, G.I., Chorin, A.J. and Prostokishin, V.M. The turbulent wall jet: A triple-layered structure and incomplete similarity, *Proc. Natl. Acad. Sci. U.S.A*, 2005, **102**(25) pp. 8850-8853.

[**87**] Afzal, N. Analysis of power law and log law velocity profiles in the overlap region of a turbulent wall jet, *Proc. R. Soc. A,* 2005, **461**(2058), pp. 1889-1910.

[**88**] Dey, S. and Sarkar, A. Response of velocity and turbulence in submerged wall jets to abrupt changes from smooth to rough beds and its application to scour downstream of an apron, *J. Fluid Mech.,* 2006, **556**, pp. 387-419.

[**89**] Ead, S.A. and Rajaratnam, N. Plane turbulent wall jets on rough boundaries with limited tailwater, *J. Eng. Mech.,* 2004, **130**(10), pp. 1245-1250.

[**90**] Ead, S.A. and Rajaratnam, N. Plane turbulent wall jets in shallow tailwater, *J. Eng. Mech.,* 2002, **128**(2), pp.143-155.

[**91**] Tangermann, R. and Gretler, W. The computation of a two-dimensional turbulent wall jet in an external stream, *J. Fluids Eng.,* 2001, **123**(1), pp.154-160. [**92**] Whelan, J.I., Graham, J.M.R. and Peiró, J. A free-surface and blockage correction for tidal turbines, *J. Fluid Mech.*, 2009, **624**, pp. 281-291.

[**93**] Garrett, C. and Cummins, P. The efficiency of a turbine in a tidal channel, *J. Fluid Mech.,* 2007, **588**, pp. 243-251.

[**94**] Norman, J. (President of ABS Alaskan Inc.). *RE: EnCurrent hydrokinetic turbines.* Personal telephone communication with Arango, M., August 2010.

[**95**] New Energy Corporation Inc. Transition to a device supplier. Presented in the *Ocean Renewable Energy Group (OREG) 2008 Fall Symposium: Building the business of ocean energy*, Whistler, Canada, 19-20th November 2008. [Online] Available from: http://www.oreg.ca/docs/2008_Fall_Symposium/Bear.pdf [Accessed 23 February 2011]

[**96**] Alaska Power & Telephone Company. *RE: Proposal to AEA Renewable Energy Fund, Round IV: "Yukon River debris mitigation study".* Grant Application submitted to the Alaska Energy Authority, 15 September 2010. [Online] Available from: ftp://ftp.aidea.org/RENEWABLE%20ENERGY%20FUND/Round%204%20September%202010/638_APTC_Yukon%20River%20Debris%20Mitigation%20Project/YRDS_Grant_Application.pdf [Accessed 6 February 2011]

[**97**] Lako, P. *Hydropower*. IEA ETSAP Technology Brief *E12,* May 2010. [Online] Available from: http://www.etsap.org/E-techDS/PDF/E07-hydropower-GS-gct.pdf [Accessed 24 February 2011]

[**98**] Guo, J. and Julien, P. Turbulent velocity profiles in sediment-laden flow, *J. Hydraul. Res.*, 2001, **39**(1), pp. 11-23.

[**99**] Wang, X., Wang, Z., Yu, M. and Li, D. Velocity profile of sediment suspensions and comparison of log-law and wake-law, *J. Hydraul. Res.*, 2001, **39**(2), pp. 211-217.

[**100**] Qingyang, S. Velocity distribution and wake-law in gradually decelerating flows, *J. Hydraul. Res.*, 2009, **47**(2), pp. 177-184.

[**101**] Song, T. and Chiew, Y.M. Turbulence measurements in nonuniform open-channel flow using Acoustic Doppler Velocimeter (ADV), *J. Eng. Mech.*, 2001, **127**(3), pp. 219-232.

[**102**] Tachie, M.F., Bergstrom, D.J. and Balachandar, R. Rough wall turbulent boundary layers in shallow open channel flow, *J. Fluids Eng.,* 2000, **122**(3), pp. 533-541.

[**103**] Brzek, B., Torres-Nieves, S., Lebrón, J., Cal, R., Meneveau, C. and Castillo, L. Effects of free-stream turbulence on rough surface turbulent boundary layers, *J. Fluid Mech.,* 2009, **635**, pp. 207-243.

[**104**] Long, C.E., Wilberg, P.L. and Nowell, A.R.M. Evaluation of von Karman's constant from integral flow parameters, *J. Hydraul. Eng.*, 1993, **119**(10), pp. 1182-1190.

Appendix A: Probability Distributions

Table A.1 Annual Probability Distribution of Total River Discharge for the Wanapum Tailrace Based on the Years 1994-2009

River Discharge' Edge Bin (kcms)	Count	Probability
.57	0	0
.85	10	.00188
1.13	79	.01484
1.42	174	.03268
1.70	401	.07532
1.98	511	.09598
2.26	481	.09035
2.55	568	.10669
2.83	551	.10349
3.11	465	.08734
3.40	408	.07663
3.68	319	.05992
3.96	304	.05710
4.25	248	.04658
4.53	203	.03813
4.81	139	.02611
5.10	122	.02291
5.38	84	.01578
5.66	60	.01127
5.95	38	.00714
6.23	34	.00639
6.51	32	.00601
6.80	26	.00488
7.08	26	.00488
7.36	16	.00300
7.65	12	.00225
7.93	8	.00150
8.21	5	.00094
8.50	0	0

Table A.2 Annual Probability Distribution of Total River Discharge for the Priest Rapids Tailrace Based on the Years 1994-2009

River Discharge' Edge Bin (kcms)	Count	Probability
.57	1	.00019
.85	9	.00169
1.13	93	.01749
1.42	166	.03123
1.70	366	.06885
1.98	527	.09913
2.26	478	.08992
2.55	537	.10102
2.83	522	.09819
3.11	451	.08484
3.40	387	.07280
3.68	331	.06226
3.96	277	.05211
4.25	259	.04872
4.53	209	.03931
4.81	173	.03254
5.10	133	.02502
5.38	93	.01749
5.66	72	.01354
5.95	51	.00959
6.23	47	.00884
6.51	44	.00828
6.80	27	.00508
7.08	26	.00490
7.36	16	.00301
7.65	11	.00207
7.93	7	.00132
8.21	3	.00056
8.50	0	0

Table A.3 Count of Velocities Calculated at the Draft Tube Outlet of the Wanapum Powerhouse Units for the Years 2007-2009 (pp.127-128)

Velocity Edge Bin (m/s)	Unit1 Count	Unit2 Count	Unit3 Count	Unit4 Count	Unit5 Count	Unit6 Count	Unit7 Count	Unit8 Count	Unit9 Count	Unit10 Count
0	27	25	5	75	98	17	24	41	19	59
0.05	3	0	0	4	11	1	1	0	3	1
0.10	2	1	1	6	11	1	7	1	0	1
0.15	6	1	2	5	7	2	6	2	0	2
0.20	8	1	2	6	21	0	6	0	1	0
0.25	11	2	1	4	15	1	4	1	4	1
0.30	11	1	0	5	24	0	2	0	1	2
0.35	6	3	3	11	15	0	7	1	2	1
0.40	6	0	1	9	15	2	3	2	2	2
0.45	7	4	2	15	27	1	5	3	1	1
0.50	11	3	4	14	24	1	6	5	2	4
0.55	7	4	1	13	17	1	8	3	4	1
0.60	10	3	0	20	16	0	6	1	1	3
0.65	13	1	5	9	19	0	9	0	3	0
0.70	12	2	5	15	21	1	6	3	6	6
0.75	19	1	3	12	15	0	8	5	3	2
0.80	15	0	4	13	19	1	9	1	3	2
0.85	11	3	9	14	13	1	13	5	4	1
0.90	11	0	8	19	21	1	12	5	19	3
0.95	13	2	11	11	16	1	12	6	10	7
1	20	2	7	17	8	0	16	5	4	1
1.05	15	1	10	23	14	2	9	4	9	4
1.10	16	1	11	12	19	2	14	5	10	3
1.15	17	2	10	15	16	4	16	15	7	4
1.20	24	2	8	16	15	0	17	10	10	4
1.25	20	0	10	17	19	2	20	16	13	11
1.30	16	2	13	24	17	6	17	6	5	12
1.35	15	0	14	22	10	1	27	17	14	5
1.40	23	3	11	18	18	1	22	15	7	7
1.45	32	4	14	19	15	2	27	13	14	12
1.50	22	5	20	26	14	4	23	21	15	13
1.55	29	5	19	17	18	4	25	23	12	12
1.60	22	13	31	22	14	5	23	29	9	26
1.65	28	9	26	19	12	10	23	27	14	18
1.70	28	20	22	17	14	16	24	24	21	16
1.7	21	23	33	16	24	20	25	25	24	26
1.80	25	32	27	16	14	28	33	31	32	19
1.85	18	63	31	21	14	45	29	36	16	33
1.90	27	46	23	20	14	36	29	42	19	26
1.95	27	64	24	22	6	46	34	38	22	31
2	17	72	29	18	21	38	40	46	25	37
2.05	26	62	26	20	21	40	28	46	20	37
2.10	23	56	29	20	11	36	20	42	25	38

2.15	25	66	29	22	6	32	25	41	22	33
2.20	29	58	21	21	24	40	23	46	23	33
2.25	24	52	36	32	19	31	30	47	30	33
2.30	24	44	34	29	21	34	27	32	24	26
2.35	34	42	37	27	31	22	44	46	18	38
2.40	30	38	34	32	24	34	41	40	29	21
2.45	32	51	37	38	30	40	45	47	20	30
2.50	39	54	41	43	36	42	41	46	29	32
2.55	45	43	42	42	41	32	39	47	30	17
2.60	43	45	48	42	44	43	45	42	38	7
2.65	17	21	20	17	17	23	19	14	18	6
2.70	11	12	10	9	9	8	5	7	12	6
2.75	4	8	5	7	4	6	6	7	6	1
2.80	6	5	7	4	5	2	3	2	3	0
2.85	7	6	8	5	7	3	3	4	6	2
2.90	5	5	1	7	3	2	4	4	7	2
2.95	1	2	0	2	2	4	1	2	2	3
3	0	0	0	0	0	0	0	1	0	0

Table A.4 Count of Velocities Calculated at the Draft Tube Outlet of the Priest Rapids Powerhouse Units for the Years 2007-2009 (pp.129-130)

Velocity Edge Bin (m/s)	Unit1 Count	Unit2 Count	Unit3 Count	Unit4 Count	Unit5 Count	Unit6 Count	Unit7 Count	Unit8 Count	Unit9 Count	Unit10 Count
0	42	33	40	49	35	12	124	170	231	232
0.05	2	1	2	1	1	0	5	10	12	11
0.10	2	1	2	0	2	0	2	8	8	12
0.15	1	1	2	0	4	0	7	6	9	19
0.20	0	1	0	1	1	0	7	16	22	15
0.25	1	2	3	0	3	1	9	12	14	21
0.30	4	2	1	1	4	1	5	14	17	19
0.35	5	1	5	3	6	0	18	24	27	11
0.40	2	4	6	0	8	1	11	34	25	23
0.45	3	2	2	0	8	1	15	19	24	10
0.50	8	4	4	2	2	0	13	15	22	21
0.55	5	4	5	3	2	1	10	18	22	22
0.60	6	4	3	3	9	3	18	22	19	10
0.65	8	8	1	4	6	1	14	15	12	10
0.70	3	4	9	1	11	2	15	20	16	19
0.75	5	2	4	3	8	2	16	18	20	18
0.80	3	2	6	3	5	1	16	15	20	9
0.85	9	8	8	3	10	3	14	13	13	10
0.90	5	4	3	3	8	2	12	26	15	17
0.95	5	3	6	3	9	0	12	15	15	11
1	3	5	0	2	9	0	12	21	20	7
1.05	7	7	10	3	14	1	20	8	13	11
1.10	4	8	10	2	11	1	13	15	13	11
1.15	4	6	8	5	11	4	15	12	11	10
1.20	11	9	8	5	9	4	4	18	9	16
1.25	10	7	11	5	17	5	11	15	17	15
1.30	10	6	10	3	11	7	13	12	13	11
1.35	4	11	16	4	18	2	11	17	10	15
1.40	20	29	26	3	29	23	20	15	11	14
1.45	17	19	19	3	24	11	18	14	10	10
1.50	19	12	28	3	17	14	12	15	16	12
1.55	17	16	15	7	23	19	18	9	12	10
1.60	16	30	31	18	31	28	16	18	6	13
1.65	29	40	38	22	29	47	15	12	7	17
1.70	30	41	37	34	27	37	25	20	13	17
1.7	38	52	46	37	38	47	24	14	14	18
1.80	44	56	56	47	44	66	31	15	14	16
1.85	52	62	57	48	37	69	35	10	13	21
1.90	52	58	50	60	46	64	25	27	17	8
1.95	63	56	47	65	64	85	43	27	17	25

2	66	56	50	70	40	72	29	18	17	24
2.05	45	46	39	50	44	48	31	14	12	14
2.10	55	45	45	83	39	53	41	25	17	22
2.15	41	45	40	41	36	48	29	21	24	22
2.20	40	35	38	43	36	42	20	9	10	10
2.25	44	32	36	43	38	42	30	25	23	19
2.30	38	27	28	43	20	28	24	16	15	18
2.35	22	21	16	30	23	18	15	13	9	12
2.40	26	25	26	40	27	32	21	19	23	21
2.45	23	17	15	22	20	19	17	15	10	19
2.50	20	33	29	34	22	22	13	12	16	16
2.55	22	23	22	23	25	25	25	24	20	24
2.60	21	22	27	25	21	25	22	23	21	28
2.65	25	25	27	16	29	28	34	29	27	24
2.70	23	7	9	31	12	17	9	15	19	15
2.75	6	5	4	30	3	3	2	4	4	5
2.80	3	4	3	10	4	5	5	4	3	3
2.85	4	4	6	3	6	4	4	5	5	3
2.90	3	3	1	0	0	0	1	1	2	0
2.95	0	0	0	0	0	0	0	0	0	0
3	0	0	0	0	0	0	0	0	0	0

Table A.5 Probability Distribution of River Flow during Spring and Summer Fish Spill Season 2007-2009

River Discharge' Centered Bin (kcms)	Count	Probability	Probability of Flow Being Greater than River Discharge'
8	0	0	0
7.6	5	.0147	.0147
7.2	7	.0206	.0354
6.8	7	.0206	.0560
6.4	12	.0354	.0914
6	5	.0147	.1062
5.6	16	.0472	.1534
5.2	33	.0973	.2507
4.8	40	.1180	.3687
4.4	48	.1416	.5103
4	40	.1180	.6283
3.6	35	.1032	.7316
3.2	27	.0796	.8112
2.8	33	.0973	.9086
2.4	21	.0619	.9705
2	5	.0147	.9853
1.6	5	.0147	1

Table A.6 Probability Distribution of Spillway Flow during Spring and Summer Fish Spill Season and of River Discharge when the Spillway is not in Operation 2007-2009

Spillway Discharge Bins (kcms)	Count	Probability	Cumulative Probability	River Discharge Bins when Spillway Discharge is zero and Fish Bypass is On (kcms)	Count	Exceedance Probability
0	187	0.5516	0.5516	5	0	0
.15	31	0.0914	0.6431	4.82	0	0
.3	16	0.0472	0.6903	4.64	3	0.0160
.45	7	0.0206	0.7109	4.46	9	0.0642
.6	14	0.0413	0.7522	4.28	16	0.1497
.75	11	0.0324	0.78466	4.10	20	0.2567
.9	13	0.038	0.8230	3.92	16	0.3422
1.05	10	0.029	0.8525	3.74	17	0.4332
1.2	12	0.035	0.8879	3.56	14	0.5080
1.35	2	0.0059	0.8938	3.38	9	0.5561
1.5	2	0.0059	0.8997	3.20	12	0.6203
1.65	3	0.0088	0.9085	3.02	12	0.6845
1.8	2	0.0059	0.9144	2.84	16	0.7701
1.95	2	0.0059	0.9203	2.66	16	0.8556
2.1	5	0.0147	0.9351	2.48	12	0.9198
2.25	6	0.0177	0.9528	2.30	5	0.9465
2.4	3	0.0088	0.9616	2.12	1	0.9519
2.55	3	0.0088	0.9705	1.94	4	0.9733
2.7	1	0.0029	0.9734	1.76	0	0.9733
2.85	2	0.0059	0.9793	1.58	4	0.9947
3	7	0.0206	1	1.4	1	1

Table A.7 Probability Distribution of Spillway Flow
When the Fish Passage is Not in Operation 2007-2009

Spillway Discharge Bins (kcms)	Count	Probability	Cumulative Probability	River Discharge Bins when Fish Bypass Discharge is zero and Spillway is On (kcms)	Count	Exceedance Probability
0	54	0.7105	0.7105	6.1	4	0.0526
0.4	10	0.1316	0.8421	5.6	3	0.0921
0.8	1	0.0132	0.8553	5.1	5	0.1579
1.2	4	0.0526	0.9079	4.6	6	0.2368
1.6	0	0	0.9079	4.1	17	0.4605
2	3	0.0395	0.9474	3.6	21	0.7368
2.4	1	0.0132	0.9605	3.1	9	0.8553
2.8	1	0.0132	0.9737	2.6	10	0.9868
3.2	0	0	0.9737	2.1	0	0.9868
3.6	2	0.0263	1	1.6	1	1

Appendix B: Distribution of the Velocity Profile Parameters for the Downstream Sites

In section 3.2, the velocity profiles extracted along the sites identified downstream from the dams were shown to fit to the modified version of the Cole's Law of the Wake reported by Guo and Julien [58]. Four different parameters (u_*, Π, δ, z_o) have to be fitted in order to satisfy the equation, which was presented as,

$$u = \frac{u_*}{\kappa}\left[ln\frac{z}{z_o} - \frac{1}{3}\left(\frac{z-z_o}{\delta-z_o}\right)^3\right] + \frac{2\Pi u_*}{\kappa} sin^2\frac{\pi(z-z_o)}{2(\delta-z_o)} \qquad \text{(B.1).}$$

As reported by Guo and Julien [96], when the water in the flow is considered to be 'clear' or free of sediment, the universal von Kármán constant (κ) was found by Guo to be equal to 0.406. Although it is noted as a constant, κ has been found to depend on sediment suspension and concentration, which leads to a density stratification in the water column and a decrease in the value of κ [98,99].Sturm [11] presents the constant with a value ranging between 0.40 and 0.41. In the application of the modified equation B.1, Guo and Julien use a value for κ of 0.41, as is similarly done by Castro-Orgaz [62], Nezu and Nakagawa [65], and Tominaga and Nezu [69], in their studies on turbulent velocity profiles.

Onitsuka, Akiyama, and Matsuoka [60], Nezu and Nakagawa [65], Qingyang [100] and Song and Chiew [101], discuss the dependence of Π on the streamwise pressure gradient parameter. As presented by Onitsuka et al. and Song and Chiew, the pressure gradient parameter for steady 2D nonuniform flow is defined as,

$$\beta = \frac{h}{\rho u_*^2}\left(-\rho g sin\theta + \frac{\partial P}{\partial s}\right) \qquad \text{(B.2)}$$

where h(m) is the depth of the flow, ρ(kg/m^3) is the density of the liquid, u_*(m/s) is the shear velocity as defined in equation 3.3, θ(rad) is the angle of the river bed, and $\partial P/\partial s$(N/m^3) is the pressure gradient with respect to the streamwise direction denoted by 's'.

If the pressure gradient is assumed hydrostatic, as it is commonly considered for natural rivers, then the streamwise pressure gradient is equal to,

$$\frac{\partial P}{\partial s} = \rho g cos\theta \frac{\partial h}{\partial s} \qquad \text{(B.3)}$$

where $\partial h/\partial s$(m/m) is the change in depth in the streamwise direction.

Qingyang [100] reports on empirical correlations established between Π and β by Nezu, Kadota, and Nakagawa, as well as Song and Graf, and a relation established by Qingyang. Song and Chiew [101] present an empirical relation established in their study and compare it to that established by Song and Graf and that determined by Kironoto and Graf. It is clear from looking at the various results that a general agreement on an exact relation that can be used to determine Π is not currently established among researchers.

Reported values for Π were found to range from -0.81 to 2.13 for various pressure gradients, with agreement that an increase in the wake parameter occurrs for increasing adverse pressure gradients. As summarized by Tachie, Bergtrom, and Balachandar [102]: For a zero pressure gradient, Π was initially reported by Cole to equal 0.55 at large *Re* numbers but later reported to asymptotically reach a value of 0.62; in research performed by Nezu and Rodi it was reported that at a sufficiently large *Re* number (> 2 x 10^5), Π becomes independent of the *Re* number and has a value of approximately 0.2 for a zero pressure gradient, whereas Xinyu et al. reported a value closer to 0.3. More recently Guo, Julien, and Meroney [56] have reported a value of Π independent of the *Re* number in a zero-pressure-gradient as being 0.76.

The wake parameter has also been reported to depend on flow history, the aspect ratio of the cross-sectional area of the channel, the roughness of the bed, and turbulence levels in the outer part of the boundary layer and the free stream [65,101-103]. In a study performed by Brzek, Torres-Nieves, Lebrón, et al. [103] on the effects of free stream turbulence on rough surface turbulent boundary

layers, a reported value of -0.10 for Π was attributed to the presence of free stream turbulence intensities of 6.2%, constituting a decrease in Π from 0.70 for zero free stream turbulence.

Without having sufficient data to determine the pressure gradient in the streamwise direction in this study it is difficult to attempt to use any of the established correlations for Π. As stated in section 3.2 the parameter is hence obtained through a least-square curve fit to the extracted velocity profile data, but is considered to still offer some insight into the pressure gradient.

Per equation 3.3, the shear stress on the wetted boundary (τ_0) is directly related to the shear velocity (u_*). As defined by Kundu [13] for fully developed 2D wall bounded turbulent velocity profiles,

$$\tau_0 = \mu \frac{du}{dz} \qquad \text{(B.4)}$$

where μ (kg/(ms)) is the dynamic viscosity of water and du/dz (1/s) is the gradient of the streamwise velocity (u) with respect to the height above the wall (z) at the point on the river bed where the no-slip condition is satisfied. However, all of the data used was found far above from where the viscous interaction occurs and therefore the influence of the turbulent fluctuations over the vertical velocity distribution are imbedded within the velocity gradient used to fit u_* and a value for τ_0 deduced from the fitted value of u_* would be inclusive of the shear stress on the bed resulting from a balance between the pressure gradient and weight contribution, plus the added effects of the Reynolds' stresses.

The value z_o found across both sites was stated to fall between 10^{-7} and 10^{-5}. These values were found to increase as the discharge increased and were not similarly distributed across each site. Recalling that the viscous sublayer is found for $z^+ < 5$ and considering that the velocity distribution in this sublayer has been found to vary linearly [11,13], the appearance of z_o in the term $\frac{u_*}{\kappa} ln \frac{z}{z_o}$ in equation B.1 shows that if z^+ is smaller than 5 when the value of z_o is used, then z_o is related to the thickness of the viscous layer [11,104]. For the high discharge cases, where the value of both

the shear velocity and z_o were the highest, the median value across the sites is z^+= 4.94 for the Wanapum site and z^+= 1.91 for the Priest Rapids site. Therefore the value and distribution of z_o is taken to represent a height of the viscous sublayer. Since the influence of the viscosity does not significantly affect the distribution of the velocities for z^+> 5, the distribution of this value across the sites is not further discussed.

B.1 Wanapum Site

In section 3.2.1 the shear velocity distribution was shown for the case of a median discharge (3.00kcms) where only the powerhouse was operating. This scenario is considered as a 'neutral' case where the distribution of the shear is determined by the natural shape of the river. Figures B.1 and B.2 show the shear velocity distribution plotted alongside the bed elevation for the fish bypass and regular spill operating, respectively. Figure B.1 is for a low river discharge (1.70kcms) and figure B.2 is for a high discharge (5.79kcms). It is noted, that as in figure 2.12c, the river bed bathymetry assumed by IIHR in the CFD simulations for low discharge (figure B.1) is different than assumed for the medium (figure 3.3) and high discharges (figure B.2).

In a flume experiment performed by Holden and James [52] in a compound channel consisting of a trapezoid and two shallow rectangular banks, the interaction between the main channel and the shallow bank showed an increase in the bed shear in the main channel relative to the bed shear in the shallow plain as the discharge decreased. As the discharge increased the difference in bed shear was reduced with an eventual transfer of the peak bed shear to the shallow plain. This is similarly observed in the results of Knight and Demetriou [54] and Tominaga and Nezu [69].

If the results for powerhouse-only (figure B.3) is used as a baseline for the shear velocity, during a decrease in river discharge a similar plateau for the shear velocity across the deeper region of the river would be expected, with a relative decrease in shear velocity occurring between the shear velocity closer to the right bank and that flowing along the main section. On the other hand, during an increase in river flow the region where the shear velocity is observed to increase closest to the

shallow plain along the right bank would be expected to broaden and also maintain a relatively larger value than the shear along the main channel. This relation between the river stage and the shear distribution is not apparent from the results at the low and high discharge, but as noted, they instead point to the dominance of the operational configuration over the shear stress distribution. As seen in the plots, the shear velocity distribution resembles that of the specific discharge shown in figure 2.12b, and point to the transfer of momentum occurring across the site that can be attributed to the two different operational configurations.

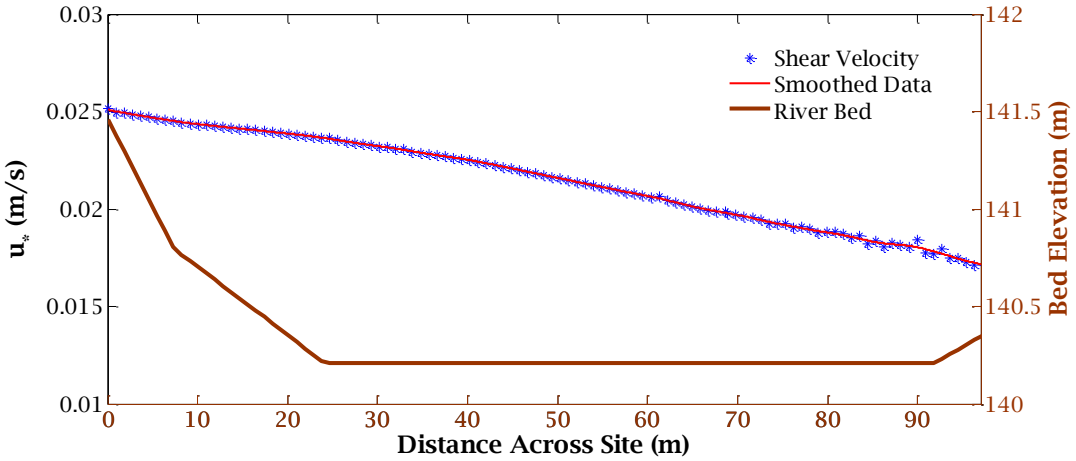

Figure B.1 Distribution of shear velocity across the Wanapum site for a river discharge of 1.70kcms, with .566kcms discharged through the fish bypass (~95% total river discharge exceedance). The smoothed data line is intended for visualization.

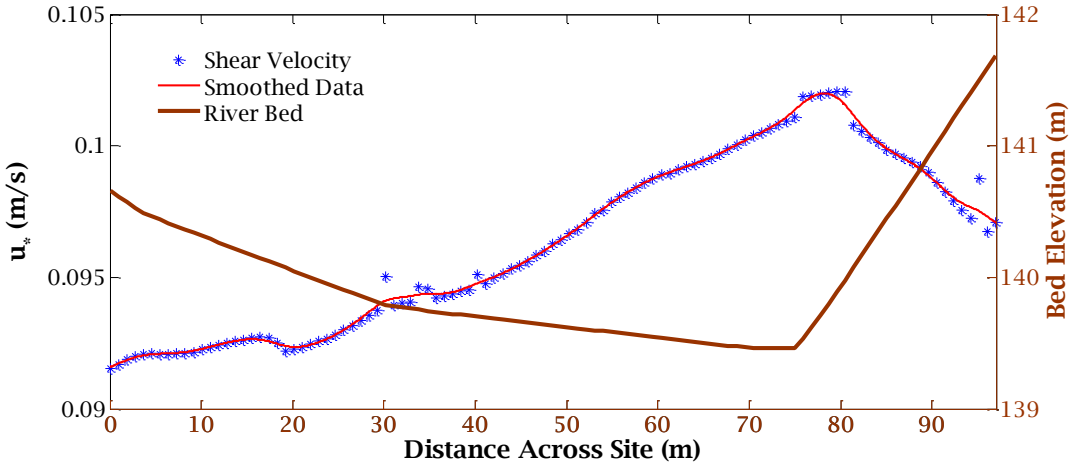

Figure B.2 Distribution of shear velocity across the Wanapum site for a river discharge of 5.79kcms, with 2.11kcms discharged through the spillway (~5% total river discharge exceedance). The smoothed data line is intended for visualization.

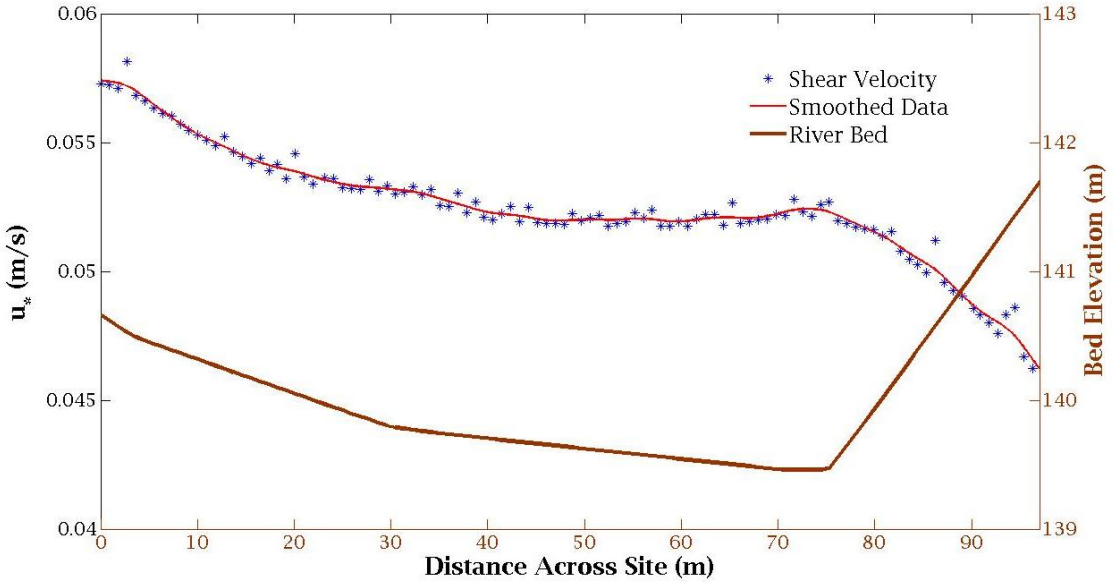

Figure B.3 Distribution of shear velocity across the Wanapum site for the 'neutral' river discharge of 3.00kcms (~50% total river discharge exceedance). The smoothed data line is intended for visualization.

The distribution of the wake strength parameter across the site is seen in figure B.4 for the three levels of discharge. Negative values are obtained for Π for all of the profiles except for the case when the fish bypass is operating (low discharge). For the median and high discharges, the parameter has a relatively constant value across the site, whereas for the low discharge the value of Π is steadily rising towards the left bank.

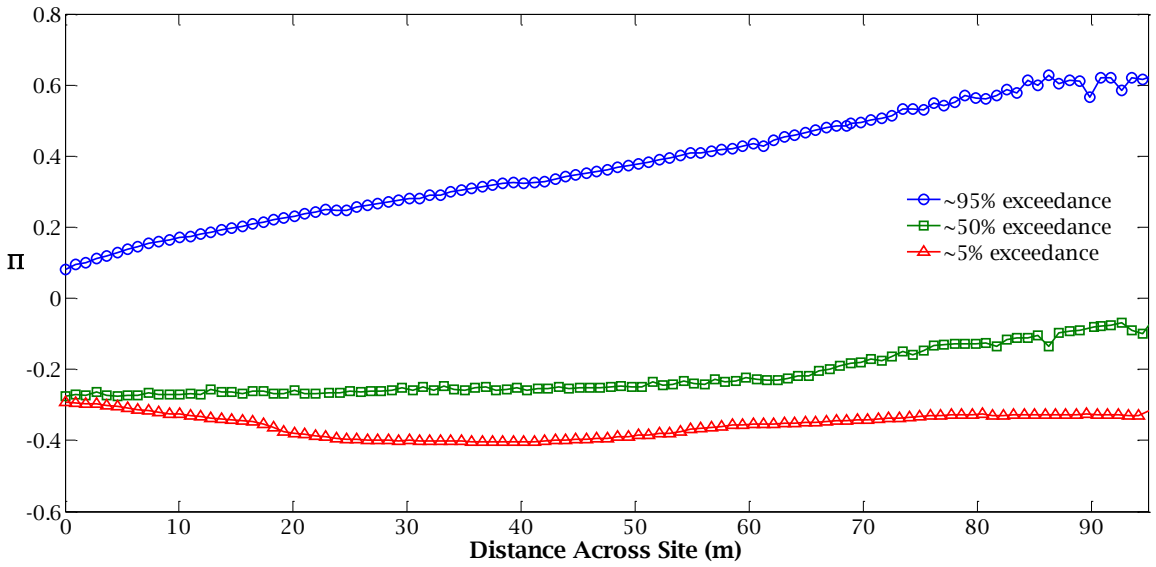

Figure B.4 Distribution of the wake strength parameter across the downstream Wanapum site.

Recalling that a large recirculation region is occurring upstream from the constriction when the fish bypass is operating, a mechanism has to be in place that maintains the equilibrium between the fluid entrained by the bypass jet and the fluid entering the recirculation region. The change to positive values of Π when the bypass is operating can indicate that this equilibrium is obtained through an adverse pressure gradient that feeds the necessary fluid back into the recirculation zone occurring in front of the spillway and slows down the rest of the flow that passes through the constriction until a point where a preferential pressure gradient is reestablished. The rise in Π in the direction of the left bank suggests that the adverse gradient originates along the left bank. This can also explain why for the low discharge case (1.70kcms) the bulk of the flow is observed to move towards the right bank as seen in the specific discharge distribution in figure 2.12b, reduces the velocities along the left bank as seen in figure 2.12a, and causes the velocity vectors to shift towards the right bank relative to the other two simulations as seen in figure 2.14. More data is necessary to further study the distribution of Π and the possible existence of this pressure gradient that can be developing when the bypass is operating. The behavior at higher river discharges, and the result of having spillway flow occurring simultaneously, is another matter that requires further attention as it is expected to have an influence as well.

The negative values of Π seem to indicate that either a zero or slightly favorable pressure gradient exists during the median discharge, which can be considered as a ‘neutral’ operational condition, and also demonstrates the presence of free stream turbulence, which is expected. As the river discharge is increased during the spillway operation, the value of Π is seen to decrease. Although the distributions are not exactly similar, the decrease in the wake parameter is not accompanied by a significant change in the shape of the distribution across the site. This decrease in Π is understood as an enhancement of mixing throughout the water column resulting from the spillway flow, rather than a significant change in free-surface slope that would alter the pressure gradient.

B.2 Priest Rapids Site

The difference in bathymetry observed between the Priest Rapids and Wanapum site can be noted to be a key role in leading to a completely dissimilar distribution of parameters across the sites. In the case of Priest Rapids, there is not a distinct main channel but rather multiple smaller deep grooves. In section 3.2.2, it was noted how the shear velocity has variations that closely resemble the jagged bathymetry, particularly as the discharge increases to the median and high discharge cases. The shear velocity distribution and maximum velocity distribution the across the Priest Rapids site are shown again in figure B.5.

By comparing between the distributions, the relative increase in the shear velocity observed along the left bank that is occurring between the 30m and 40m mark that was noted in section 3.2.2 for the median (3.91kcms) and high (5.72kcms) discharge, is seen to occur right of the peak velocities observed to occur for the median and high discharge between the 40m mark and the left side of the region studied for siting. In the case of the low discharge (1.82kcms), there is a very similar decaying distribution observed for both the shear and maximum streamwise velocity occurring from the about the 27m mark all the way to the left side of the site.

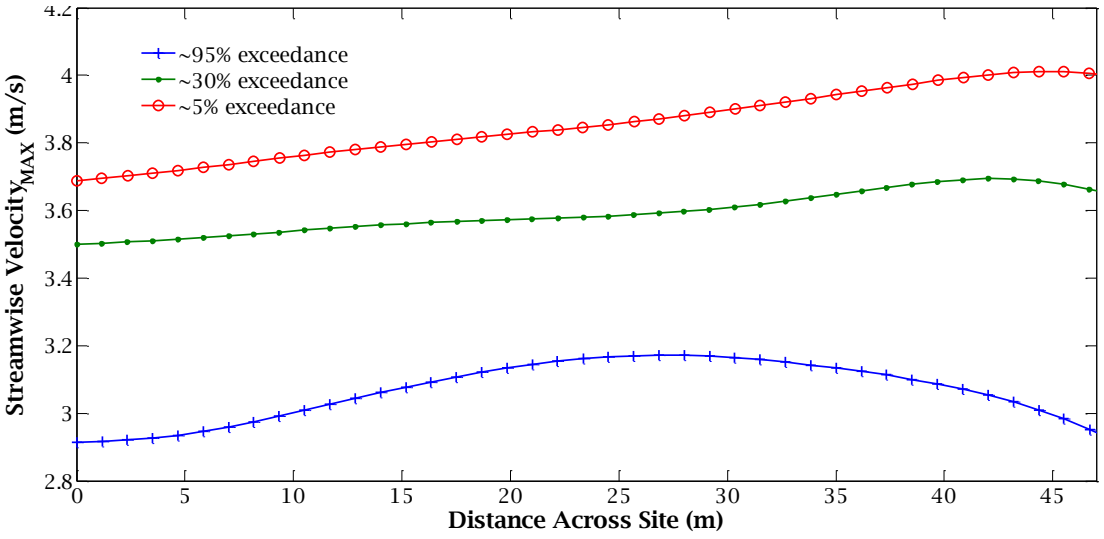

a)

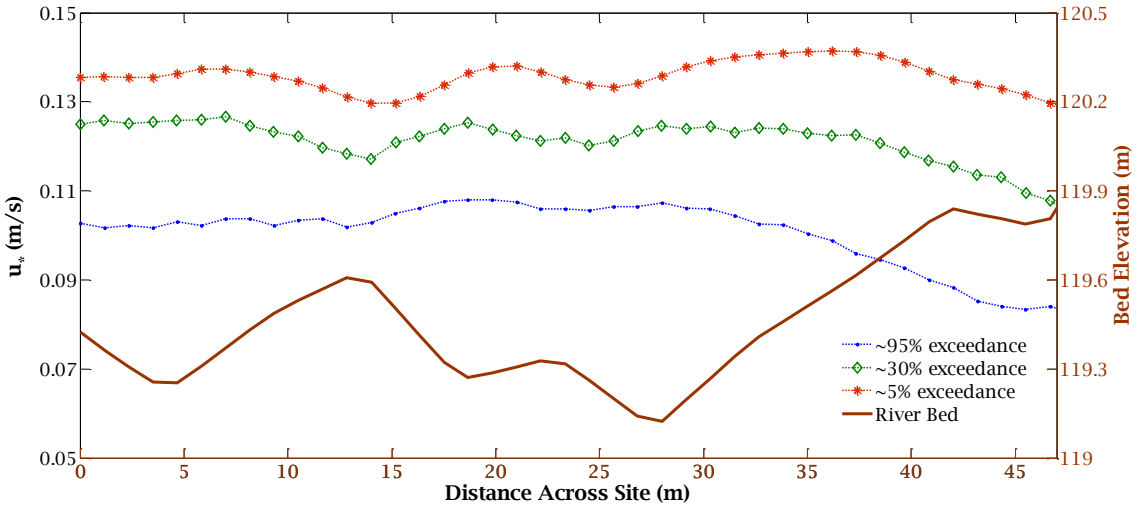

b)

Figure B.5 Distribution across the Priest Rapids site of a) the maximum streamwise velocity and b) the shear velocity for all three discharge cases.

This shows that a region of momentum transfer might be growing around the 35m mark as the discharge increases. It is pointed out that in the median and high discharge case, the additional flow is primarily discharged through the rest of the units in the powerhouse, which will cause more flow to come along the left bank. As seen in the bathymetry of the tailrace, the site is located near to where the river width is constricted as the left bank shifts towards the right bank. From the top-view of the bathymetry, the shape of the left bank resembles that of a convex surface. The relative leveling out of the shear velocity between the 30m and 40m, can be pointing to a transfer of momentum occurring from the faster flow found in the shallow area that is moving away from the left bank due the effects of the convex surface. This in turn, can be helping to increase the momentum of the slower flow in the deeper sections in the right side of the site and lead to a more uniform lateral distribution of the velocity further downstream across this series of grooves found along this side of the river.

As discussed in section 3.2.2, for this cross-section of interest the fitted value for δ is generally not found at the free surface. The results show an increase in the depth below the free surface where the velocities can be considered constant as the discharge increases and also demonstrate the pronounced effects of the bathymetry which are noticed in the waviness of the distribution. The

increase in the region of approximately constant velocities can be attributed to the enhanced mixing through the water column that result from the increase in the strength of the turbulent outburst and the higher sensitivity to this mixing due to the generally shallower depths. The distribution of δ/h is shown in figure B.6a.

The wake strength parameter across the site is plotted in figure B.6b. All of the results returned negative values for this parameter. Similarly to the Wanapum site, this is taken to indicate the expected presence of turbulence in the outer region of the boundary layer and in the free stream and the presence of either a zero or slightly favorable pressure gradient acting on the flow. The distribution of Π across the region of interest shows a higher level of fluctuation than that observed in the Wanapum site. Comparing with the variation in δ/h a very good agreement is observed to exist between the two distributions. The waviness and the behavior of Π across the site as the discharge changes are attributed to the location of δ.

A behavior is observed in the transition from low to median discharge where the difference between the maximum and minimum points is reduced in a more pronounced manner. Between the median and high discharge the distributions of both the relative location of δ and the value of Π is shifted down while maintaining a very similar distribution and similar proportions among the lateral variation of the parameters. The variability exhibited by the parameters is attributed primarily to the strong influence of the non-uniformity of the river bed along this stretch of the river and the effects of increasing stage in reducing the distinct difference between maximum and minimum values observed for the low discharge.

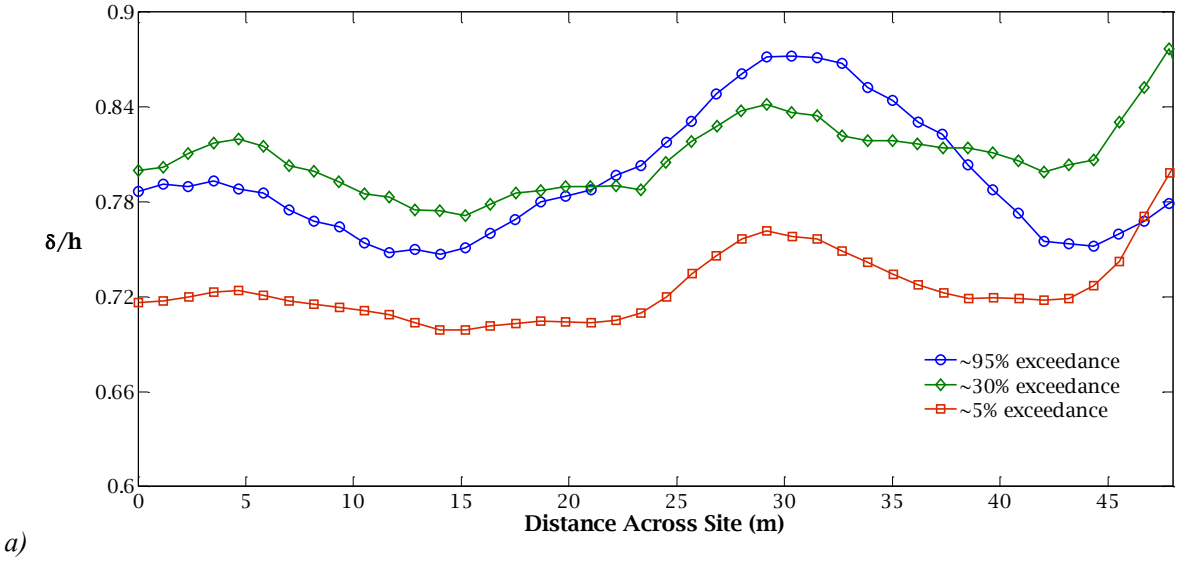

a)

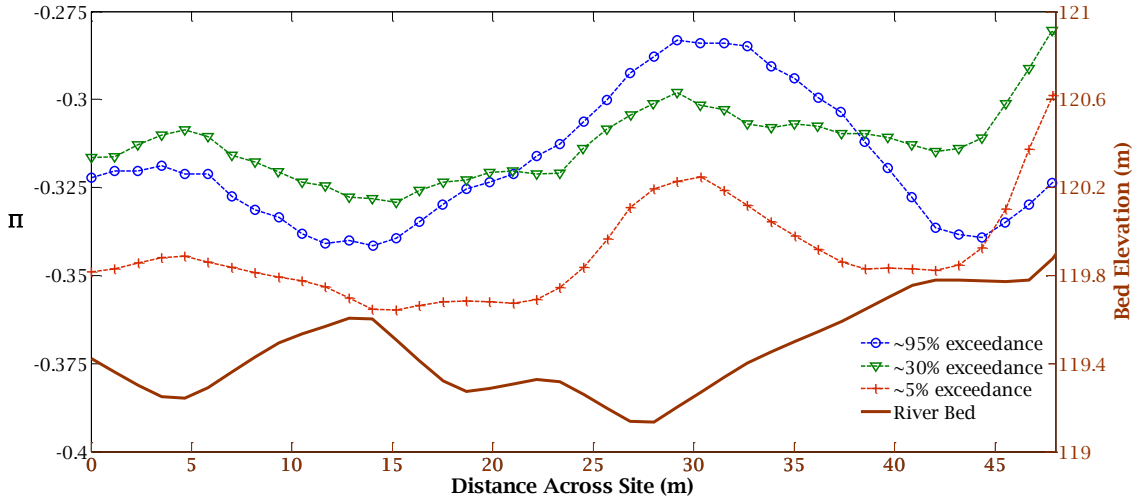

b)

Figure B.6 Distribution across the Priest Rapids site of a) the relative location of the fitted boundary layer height and b) Cole's wake strength parameter, for all three flow rates used to describe the site.

Appendix C: Results for Additional Data Planes in the Vicinity of the Powerhouses

In the analysis of the data planes running perpendicular to the face of the powerhouse, certain differences are observed in the manner in which the flow propagates from the draft tube outlet. As discussed in section 3.3.2, the wall bounded jets emanating from the draft tubes are expected to behave similarly to a jet coming out from underneath a sluice gate. The behavior is characterized by the development of a boundary layer along the river bed, an expansion of the jet up to the free surface occurring immediately downstream from a recirculation region that forms above the jet, and a transition to an open channel velocity profile as the velocity deficit in the upper section of the free jet profile is reduced through turbulent dissipation associated with the growing boundary layer, moving the point of maximum streamwise velocity to the vicinity of the free surface.

In section 3.3.2 a data plane corresponding to one of the two simulation results that depict this wall bounded jet behavior is shown. As mentioned, the CFD results for the Priest Rapids powerhouse vicinity and two data planes associated with the Wanapum powerhouse did not demonstrate the expected velocity distribution. In figure C.1 one of these data planes oriented perpendicularly to the Wanapum powerhouse is shown and in figure C.2 one of the planes running normal to the Priest Rapids powerhouse can be seen. As mentioned in section 3.3.2, this set of simulation results exemplified by figures C.1 and C.2 show a point of maximum velocity that remains at or near the river bed until its eventual dissipation. For the Wanapum case (figure C.1), after the recirculation region that ends around the 50m mark the shape of the velocity distribution outlined by the vectors show the increase in velocity occurring as the bed is approached and a jet peak that does not expand up towards the free surface. In figure C.2, the persistence of the peak velocity in the lower 20% of the water column is also observed after the recirculation region ending approximately 20m downstream from the Priest Rapids powerhouse. The vectors associated with the recirculation are not as clearly depicted in the images but it is still noticeable.

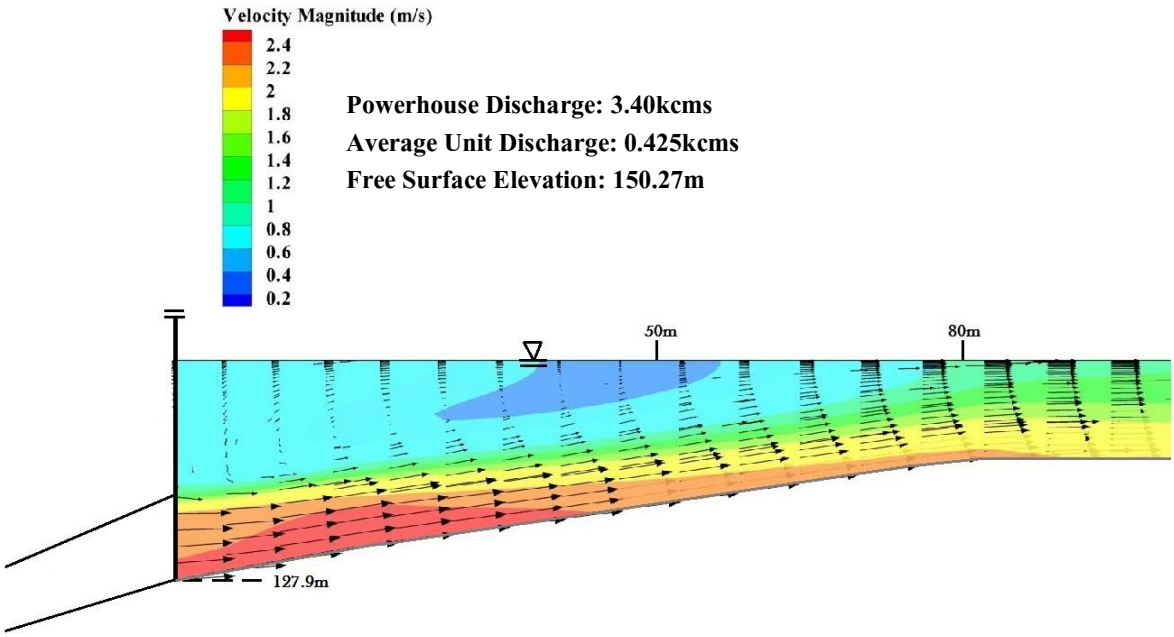

Figure C.1 Data plane perpendicular to the Wanapum powerhouse crossing through the middle bay of unit 6. Vectors originate at the nodes of the mesh of the data plane. The distance is normal to the powerhouse.

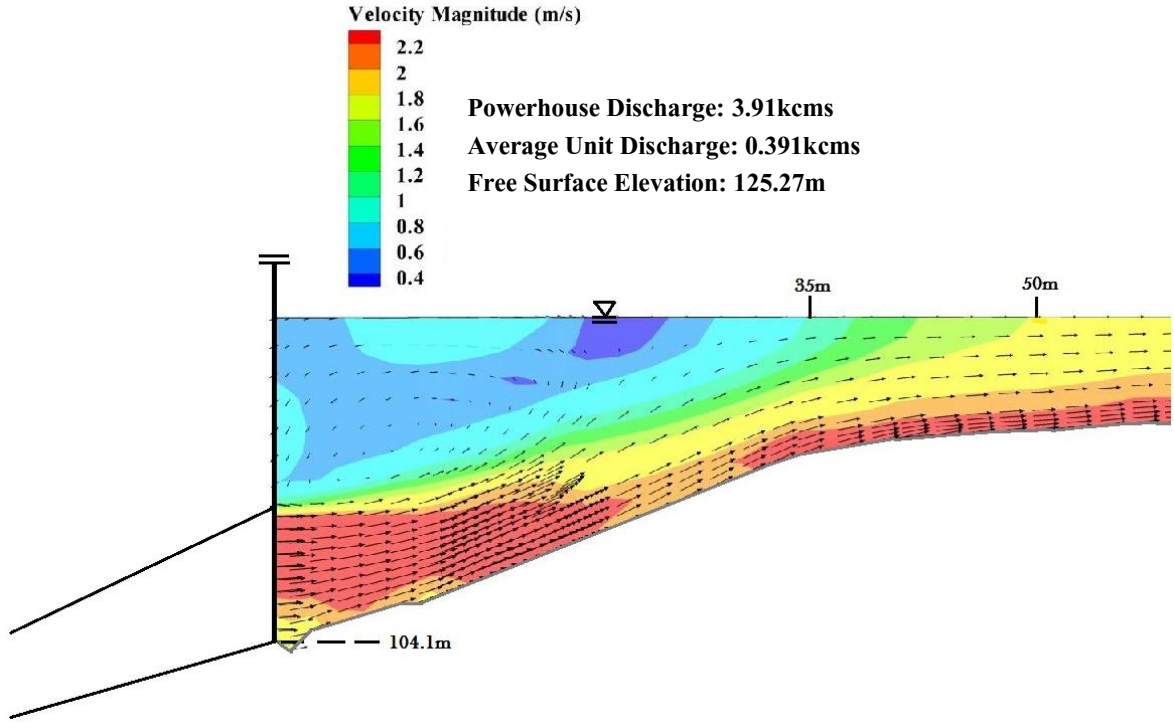

Figure C.2 Data plane perpendicular to the Priest Rapids powerhouse crossing through the middle bay of unit 4. Vectors originate at the nodes of the mesh of the data plane. The distance is normal to the powerhouse.

As with the data planes in the downstream site of the Wanapum tailrace, the bathymetry used in all of the Wanapum simulations is not seen to be the same. The river bed for the planes showing a draft tube jet progressing as that shown in figure C.1 matched the independent bathymetry exactly, whereas the data planes exemplified by figure 3.11 in section 3.3.2 correspond to a different bathymetry data that has a slightly steeper positive bed slope (~11° vs. ~9°) and an initial point of slope transition occurring almost 20m closer to the powerhouse.

Although the vertical distribution of the velocities was not similar in all of the cases, some attributes of the spatial behavior of the jet's peak velocity are shared between all of the results. Figure C.3 shows the behavior of the maximum velocity (u_{max}) for velocity distributions extracted along lines perpendicular to the river bed. The maximum velocity is normalized by the u_{max} found at the upstream edge of the data planes. In these results a comparable region is found near the draft tube outlet where the velocity increases up to a maximum value; this occurs near the 20m mark for the Wanapum case and close to 15m in front of the Priest Rapids powerhouse. This point of maximum velocity is seen to coincide with the area where the recirculating flow is aligned with the general direction of the jet flow. From this peak the value begins to decay as was observed in figure 3.13, and similarly, the presence of a second region is observed to exist where the decay process is hindered and an increase in velocity magnitude occurs once more. For most of the simulations (all except the case of an average unit discharge of 0.460kcms shown in figure 3.13) this second region spans along the section of the river bed where the initial positive slope starts to transition over to a gradual negative river bed slope. This section is found around the 80m mark in figure C.3a and the 35m mark in figure C.3b. The results shown in figure C.3b for the Priest Rapids case show a more pronounced fluctuation in the peak velocity behavior with a third point of velocity increase occurring 7m downstream from the second peak. The higher variation can be partly associated with the steeper gradient. It is reiterated that the powerhouse vicinity and the

behavior of the draft tube jets is a topic for which a minimal amount of research was found and requires further attention.

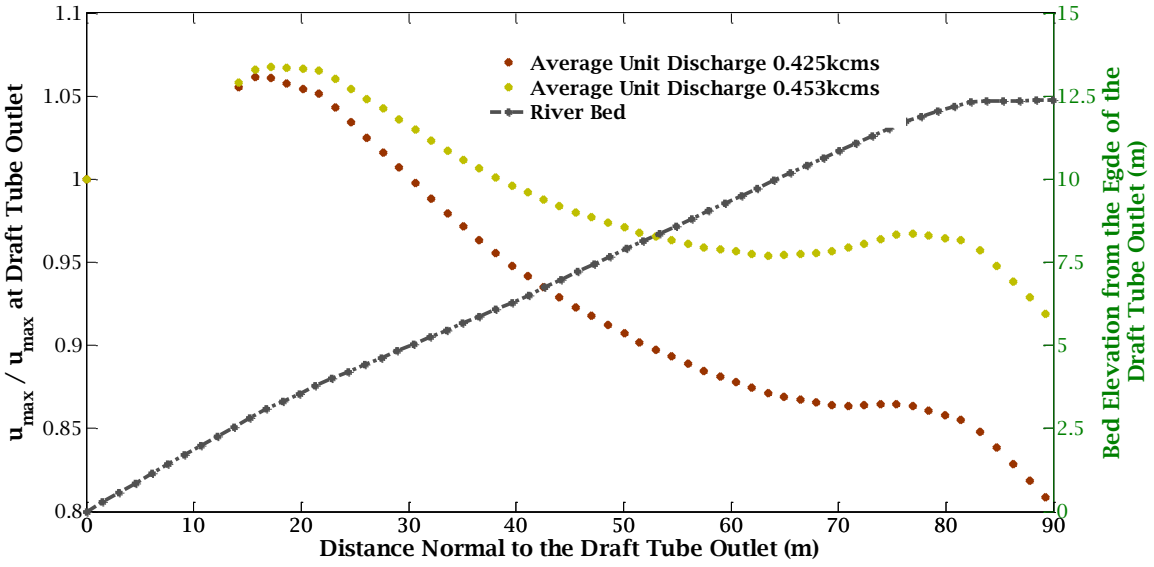

a)

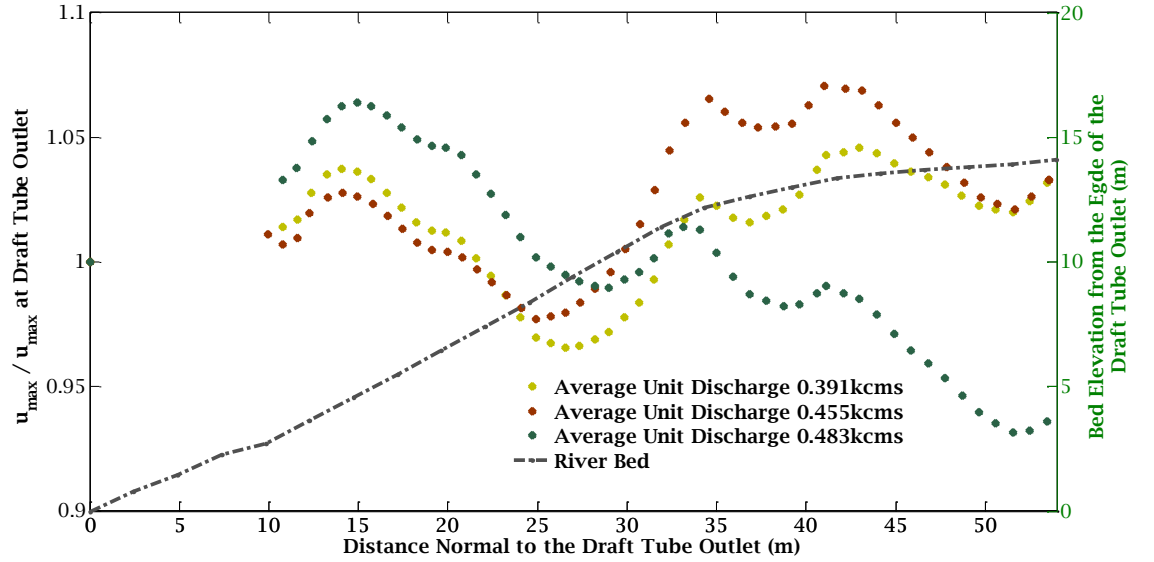

b)

Figure C.3 Behavior of the normalized maximum velocity as a function of distance from the draft tube outlet. The results in a) correspond to simulations of the Wanapum tailrace with an average unit discharge of 0.425kcms and 0.453kcms, and b) is for simulations of the Priest Rapids tailrace with an average unit discharge of 0.391kcms, 0.455kcms, and 0.483kcms.